Ollscoil na hÉireann, Corcaigh

National University of Ireland, Cork

Optimized Grating Coupler Designs for Integrated Photonics

Thesis presented by

Luca Zagaglia, PhD candidate

https://orcid.org/0000-0002-4402-3031

for the degree of

Doctor of Philosophy

University College Cork

Tyndall/SEFS

Head of School/Department: Fatima Gunning

Supervisor(s): Peter O'Brien, Francesco Floris

2021

Contents

"This is to certify that the work I am submitting is my own and has not been submitted for another degree, either at University College Cork or elsewhere. All external references and sources are clearly acknowledged and identified within the contents. I have read and understood the regulations of University College Cork concerning plagiarism and intellectual property."

Luca Zagaglia

Abstract

A wide range of expertise is enclosed in the expression: “Photonics Packaging” with the common aim of interfacing a Photonic Integrated Circuit (PIC), either optically, electrically, thermally, and mechanically, with the surrounding environment. Thus, a multi-physics approach is essential to tackle the many challenges that Photonics Packaging poses. In this context, the design process is a crucial and vital step to overcome the majority of the issues that can potentially arise during the packaging assembly procedure. As a consequence, a single person cannot manage all the aspects behind the design process, but a multidisciplinary team needs to work together engineering and optimizing the different types of connections.

The current thesis work is oriented on the optical packaging branch with particular focus on the design of the optical connections needed to deliver, in an efficiently and controlled manner, the light signal from a specific external light source or waveguide into the PIC.

This work aims to show the importance of the design process in photonics packaging, and how it can be carefully exploited and tailored to optimize coupling schemes to obtain high efficient and packaging compatible optical connectors, which can constitute the building-blocks of future photonic devises.

In this context, my research deals with the optimization of complex grating couplers for SOI platforms to couple light from a specific coupling scheme and it is divided in 4 sections.

First, Chapter 2 presents in details the customized design routine, developed during my PhD, based on a Particle Swarm Optimization, an iterative algorithm, implemented using a commercial Finite Different Time Domain (FDTD) software.

Then, in Chapter 3, the routine is exploited and tested to optimize the structural features of non-uniform grating coupler designs, characterized by a non-constant pitch. The aim is boosting their Coupling-Efficiency (CE) under a horizontal fibre coupling scheme, which is of particular interest in photonics packaging. The optimal designs were then fabricated in Cornerstone, the Silicon photonics foundry of the University of Southampton, and eventually packaged and tested at Tyndall National Institute.

High CE values, up to 83% at 1550nm, are demonstrated and the results are shown to be in excellent agreement with the computational predictions. Due to the high efficiency, these designs were requested by the foundry as part of their official Process Design Kit, which is now on offer.

In Chapter 4, the first experimental and FDTD comparative analysis of the multiwavelength response, in terms of bandwidth and asymmetry of the CE curve, is conducted and reported for such optimized non-uniform grating couplers. Here, the bandwidth is shown to be inversely proportional to the dimension of the impinging mode field diameter, which affects, together with the energy dispersion curve of each grating structure, its CE curve.

Grating coupling is not only a suitable packaging solution for fiber-to-PIC coupling, but also for direct laser-to-PIC coupling.

Chapter 5 shows how millimetre-scale FDTD simulations can be used to carefully design a Micro Optical Bench, made of a micro ball-lens and a micro prism. The μOptics are used to reshape the laser emission making it compatible with a single mode fiber emission, thus suitable for grating coupling. Here, a uniform grating coupler is used to couple the impinging electromagnetic field. A laser-to-PIC performance penalty of only 1dB, with respect to the fiber-to-PIC coupling scheme, is shown under perfect alignment conditions. The origin of the higher loss is carefully analysed suggesting that 0.6dB are due to back-reflection from the optics interfaces, and 0.4dB due to spherical aberrations. Moreover, a detailed analysis of the manufacturing and alignment tolerances is conducted demonstrating their compatibility with current standard packaging processes.

Chapter 1

Introduction

The understanding of the physical properties of materials, through the engineering of their geometrical structures, represents nowadays one of the fundamental aspects at the base of either the scientific and technological progress. Thus, the comprehension of their optical properties is the key-goal of the research field called Photonics, which has the final aim of gaining total control on light generation, propagation, and detection. This can be achieved through the engineering of the materials at dimensions comparable to the wavelength involved. In particular, thanks to the technological progress seen in the past decades behind the fabrication techniques, the features of photonics structure can be controlled down to the nanoscale.

In this context, the wide heritage earned by electronics related to the semiconductor fabrication technology of Electronic Integrated Circuit (EIC), together with the low-cost and the useful optical properties, made Silicon one of the most promising optical medium selected for the future light-based technology.

Currently, Silicon-on-Insulator (SOI) wafers are the targeted platforms employed for the creation of the multi-functional Photonic Integrated Circuits (PICs), the backbone of applied Photonics.

The scope of this first chapter is to give an overview on applied Silicon Photonics, and PICs, taking into account the technological advantages and potentialities, as well as on Photonics Packaging. Particular attention is focused on the design of the optical connections, in order to show the motivation behind this work.

1.1 Silicon Photonics

The modern requirements related to the volume and transmission velocity of data have drastically increased in the past decades making inefficient the metallic interconnection to fulfil such demand. Optical interconnection has been addressed as the potential solution to overcome such issue as the carriers of the information are now the photons. Due to their zero rest mass and no electric charge, photons enable to

overcome various issues, to name a few: reduce cross-talk, power consumption, heating problems. On the other hand, the major pros are high-speed, high-density, and high-transmission reliability.

Today, optical connections are already a reality having substituted the electrical interconnections exploited in telecom and data-com applications, either for long-distance communications through the employment of optical fibres, to the mid and short-rage scale. Here, the optical links are used to connect the servers and the different racks inside modern data centres. However, electrical interconnections still dominate the intra-chip communications limiting the speed of data flow and, here the current technology would benefit from the introduction of Photonics [1].

This constitutes the background that drove the stimulus for the development of Photonics, and especially Silicon Photonics.

The origin of Silicon Photonics can be dated back to the 1980's, when R. A. Soref *et al.* proposed Silicon as a new material for integrated optical-components [2]. This created a new era for the investigation and the development of the first Silicon-based photonics components at the end of the 1980's [3, 4] and across the 90s. During this decade, the research community developed the first passive components such as waveguides (WGs), focusing their attention on the reduction of the WG losses and their single mode operation [5, 6, 7]. Moreover, the first modulators based on a Mach-Zehnder interferometer and the prototype at the base of modern switches were proposed [8].

The motivations behind the use of Silicon as a credible material for modern applied Photonics are multiple: it is the second most abundant element on our planet, it shows a wide transparency window in the infrared between approximately 1100nm and 1700nm, large optical damage threshold, and excellent thermal conductivity, and a high refractive index, roughly 3.48 at 1550nm wavelength [9].

Above all, the most interesting aspect of Silicon is represented by the possibility of exploiting the well-established complementary metal-oxide semiconductor (CMOS) fabrication technology. The latter is currently used for the fabrication of metal-oxide-semiconductor field-effect transistor (MOSFET); thus, the compatibility with COMOS fabrication processes can potentially enable low-cost and large-scale manufacturing. These are essential aspects to target mass-production [10].

In this context, the well-established SOI platform, employed in microelectronics, appeared to be a quite interesting building block also for Photonics.

In fact, the SOI wafer is composed by a thin Silicon layer, with a typical thickness of 220nm, sandwiched between two SiO_2 layers, with a fixed thickness of the bottom layer of 2μm. The entire structure sits on an additional Silicon layer with thicknesses of the order of hundreds of microns. Figure 1 shows a cross section of a SOI wafer.

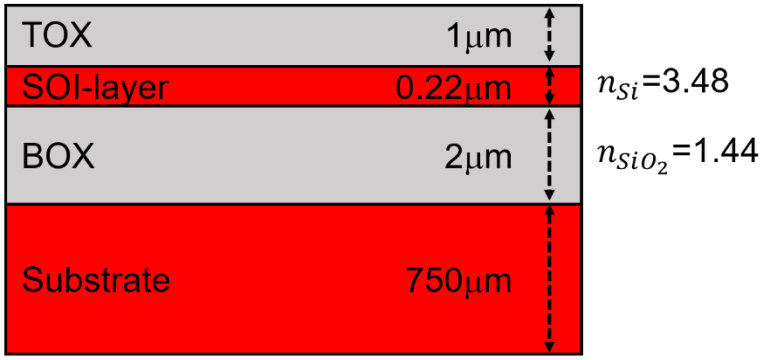

Figure 1: Typical cross-section of a Silicon-on-Insulator (SOI) wafer composed by: a 1μm-thick Top Oxide layer (TOX), a 0.22μm-thick SOI layer, a 2μm-thick Bottom Oxide layer (BOX), and a 750μm-thick Substrate. The red regions indicate the Si material with a refractive index of 3.48 at 1550nm, while the grey layers refer to the SiO_2 with a refractive index of 1.44 at 1550nm.

At the telecom and data-com wavelengths of 1310nm, center of the O-band, and 1550nm, proper of the C-band, the SOI platform is characterized by a high refractive index contrast between the Si and SiO_2 materials with values of $n_{si} = 3.48$ and $n_{SiO_2} = 1.44$ at 1550nm, [11, 12]. This high refractive index contrast allows for a tight light confinement inside single mode SOI-WGs, with mode dimensions down to 100nm. Typically, on a SOI wafer, the WG cross section is of the order of 220nm-hight times 450nm-wide.

These dimensions are compatible with the geometrical features of CMOS EIC devices [13] and allows for the harvesting of thousands of photonics structures on a single SOI wafer fulfilling the requirement for economic CMOS compatibility.

Therefore, the SOI platform constitutes the architecture at the base of modern Silicon Integrated Photonics and the bare-base for the fabrication of SOI-PICs.

1.2 Integrated Silicon Photonics and SOI-PICs

Integrated Photonics is the research field that aims for the efficient integration of specific photonics structures into a single PIC, able to exploit multiple operations: from telecom applications, automotive, Lidar, bio-sensing, as well as treatment and diagnose purposes [14, 15, 16]. The integrated Silicon Photonics is the branch of this

research field that focuses on the integration of some of the aforementioned functions onto a SOI-PIC. An image of a SOI-PIC is reported in Figure 2.

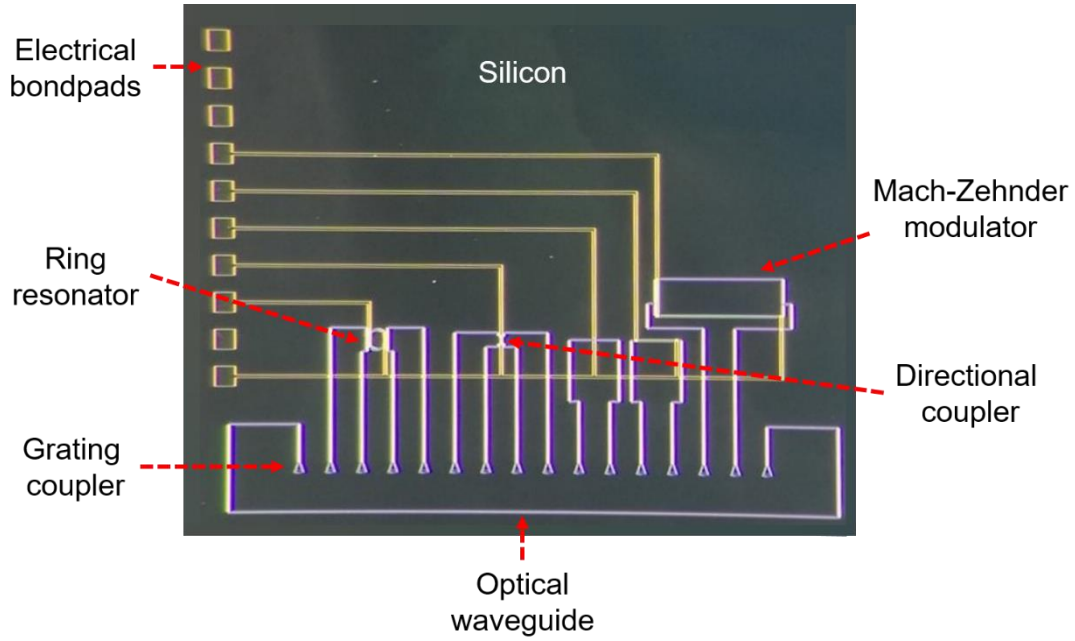

Figure 2: Picture of the PIXAPP Integrated Photonic Educational Kit (IPEK) circuit. The grating couplers fabricated on the IPEK were taken from the designs developed in this thesis.

The structures on a SOI-PIC can be divided into two main categories: passive and active components.

Here in the following, the main types of passive and active components are addressed.

Passive components are all those structures that do not generate heat, modulate or detect light. One of the key passive components are optical WGs, which enable through total internal reflection to confine light in tiny spatial region, guiding it along a specific spatial direction. WGs are the “photonics” high-ways to deliver the light signals throughout the PIC surface with losses of the order of a few dBs/cm [17], due to Rayleigh scattering consequence of the roughness of the side-walls.

Figure 3 shows the intensity profile of the transverse-electric (TE), panel (a), and transverse-magnetic (TM), panel (b), fundamental modes proper of a strip SOI-WG at the telecom wavelength of 1550nm.

For the sake of completeness, there is another category of optical WGs called Photonic Crystal WGs (PC-WG). Here, the confinement of light is achieved vertically through total internal reflection, and longitudinally through the so-called Photonic Band Gap confinement, consequence of a two dimensional periodic modulation of the

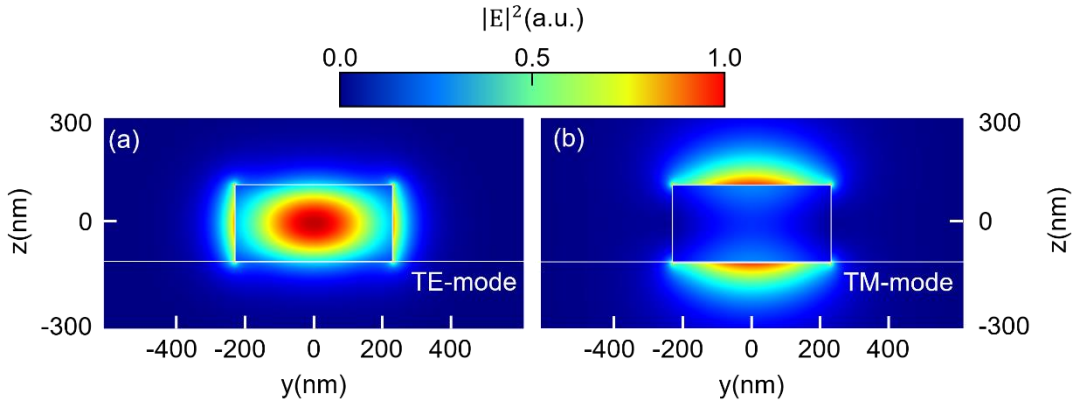

Figure 3: Intensity profile of the electric field for: (a) the TE fundamental mode, (b) the TM fundamental mode of a Silicon strip Waveguide (WG) with a height of 220nm and a width of 450nm, sandwiched inside a SiO_2 TOX and BOX layers. The modes are calculated at 1550nm.

dielectric function [18]. However, the fabrication of such structures are more complicated and suffer from higher losses due to the fabrication induced disorder [19].

Besides photonics WGs, there are several photonics structures that are currently employed to fulfil numerous applications, from telecom to sensing.

Optical filters are one of the major essential passive components that constitute modern PICs due to their ability to select the different wavelengths of a travelling pulse. A typical optical filter bases its operational behaviour on integrated diffraction-gratings or micro-cavities, exploiting micro-ring resonators [20].

The first one employed a periodic patter to separate different wavelengths, as done in echelle gratings; while a micro-ring is made of a closed loop waveguide. In this case, the cavity sustains only certain wavelengths able to satisfy the resonant condition imposed by the optical path length for an amount of time related to the cavity Q factor [21].

In this context, array-waveguide grating (AWG) represents a great example of the importance of optical filter in modern optical network, being a key component for enabling wavelength-division multiplexing (WDM) and demutiplexing. Essentially, AWGs allow to increase the bandwidth of modern optical interconnections thanks to their ability of joining several signals from different wavelength-carriers into a single transmission channel, i.e. multiplexing. Vice versa, they can be used to decompose the signal at the receiver, i.e. demultiplexing [22].

On the contrary, active components are all the structures that generate, manipulate actively and detect the light signal.

The possibility of having a light source integrated directly onto the SOI-PIC is another hot-topic research field.

Silicon, being an indirect band gap material, offers a low rate of radiative combination. Thus, the most intriguing solutions, currently, are Heterogeneous and Hybrid Integration [23]. The first approach enables to bond onto the SOI surface an un-patterned active material, which is used to fabricate the actual laser-source in a second fabrication step. On the contrary, Hybrid Integration allows to transfer directly a laser-diode onto the PIC surface. This is treated in more detail in Chapter 5.

Besides laser sources, optical modulators are essential key-integrated components due to their ability of modifying the characteristics, such as intensity, phase, and polarization of the light beam. Hence, they play an important role in optical fibre communication and optical metrology. In this field, electro-optical modulators are extensively used in Integrated Photonics as they exploit electro-optic effects to introduce a variation in either the real or imaginary part of the refractive index.

Important physical phenomena used to achieve this goal are Pockels, Kerr, and Franz-Keldysh effects, strong in III-V materials, but relative weak in Silicon [24], due to its centrosymmetric crystalline structure.

Instead, a variation in the refractive index can be induced exploiting thermal modulation, using the dependence of the refractive index from the temperature, and the plasma dispersion effect. The latter uses the dependence of the refractive index from the free carrier density [25]. These effects are currently exploited to create electro-optical modulators based on either ring-resonators or Mach-Zehnder interferometers [26].

Finally, Silicon due to its transparency windows in the O- and C-bands is an excellent material to fabricate low-loss passive components for telecom applications.

However, it is not suitable, in the same spectral interval, to fabricate large-bandwidth, high-efficient, and high-speed waveguide-integrated, rather than surface illuminated, photodetectors. This represent a current hot-topic in integrated Silicon photonics for telecom and datacom applications since the ability to detect and analyse the travelling light signal directly onto the SOI-PICs is a technological essential aspect.

Currently, the detection of light travelling inside the waveguide is achieved exploiting the physical characteristics of external materials, such as III-V compounds

or Germanium. These materials are used to create waveguide-photodiodes, either integrated or growth onto the SOI-PICs [27].

All the aforementioned photonic structures summarize briefly the vast world behind Silicon Integrated Photonics to give a general overview of the structural complexity proper of a SOI-PIC.

All these optical components are essential to perform the functions required by either a private or a public customer, resulting in quite high final cost. During the past decade, great effort has been put by foundries to decrease dramatically the cost of SOI-PICs for customers.

This goal was achieved through the introduction of Multiple-Project-Wafer (MPW) runs [28]. MPW offer the chance to share the mask and fabrication costs across different projects, *i.e.* customers, reducing significantly the economic effort of the single. Therefore, a private or a public customer can easily access to the foundry services simply navigating on-line and checking the MPW runs offered by the various foundries.

Indeed, some restrictions apply to the photonics structures due to the fabrication tolerances related to the fabrication processes available for the specific run. Thus, only a certain level of customization can be requested.

Usually, each foundry offers a list of available fabrication processes and structures, with their technical specs and efficiencies, summarized in the so-called Process Design Kit, *i.e.* PDKs. In particular, PDKs represent available commercial products.

Consequently, a single SOI-PIC can be populated through a "forest" of multiple structures to satisfy the requirements of the customer's applications.

In particular, in the past few years, organisations, such as Europractice [29], have been founded joining under a single entity multiple foundries as well as other partners. Thus, a wide range of expertise, from the fabrication till the packaging of the final SOI-PIC, are available from a single organisation.

This offers the chance to develop and fix standard design rules for Integrated Photonics, as previously done for electronics. In this context, Photonics Packaging represents the final steps of the fabrication chain to deliver the final PIC to the customer.

Through packaging processes, the PIC is interfaced with the external world allowing for the driving light signal to be in and out coupled from the circuit. In

particular, packaging processes are an essential and crucial step to allow Integrated Photonics to become a reality.

The next paragraph is focused entirely on this topic with particular attention on the optical connections, main argument of this thesis work, with a special focus on the importance of the optical design process to overcome current optical packaging issues.

1.3 Photonics Packaging

Photonics Packaging performs all the connections needed to make a PIC work. This step is quite challenging as typical photonic chips require simultaneously integration with electronics, high-speed connections, heat-dissipation through thermal vias, multi-channel fibre-to-PIC coupling. Figure 4 shows a sketch of a final packaged photonic device.

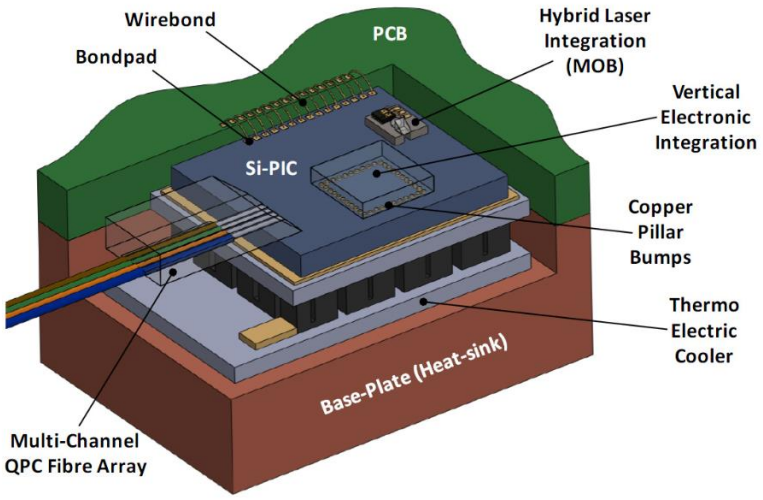

Figure 4: Layout of a packaged photonic device with all the different type of connections: electrical, thermal, optical, and mechanical. The image has been taken from [23].

Each single process, per se, is quite simple within a laboratory environment; however, dealing with all the connections at the same time is not an easy task even in a dedicated laboratory, and result way more challenging when targeting mass production.

For instance, when designing a packaged photonic device, the optical connections should be organized in order to: allow direct access to the PIC surface for in and out

coupling of the light signal, avoid the overlap with the electrical connections used to drive the PIC, and, at the same time, guarantee efficient thermal management. Moreover, the final packaged device must be mechanically stable.

All these aspects are summarized in Figure 5.

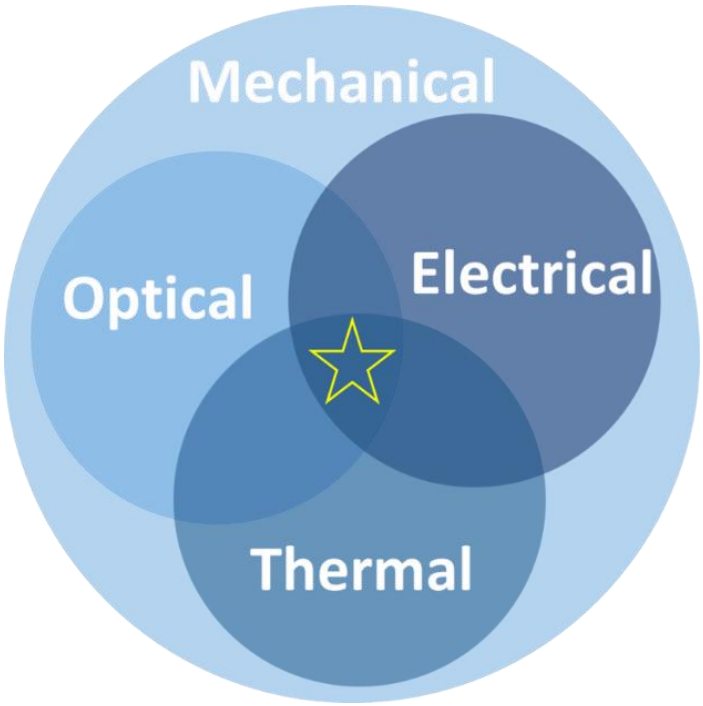

Figure 5: Sketch of the Photonics Packaging principle: optical, electrical and thermal connections should be designed in order to be efficient and to guarantee easy access to the PIC. All the three connections should also show mechanical stability.

In order to obtain a fully-functional device, Photonics Packaging should be the first step to be considered when designing a photonic device, as the design and fabrication of the PIC should fulfil and follow packaging design rules.

These rules are available through the Europractice organization [29], and are essential to avoid unnecessary level of customization of either the photonic, electrical, and thermal connections. This is one of the major problems in Integrated Photonics as customized layouts can dramatically increase the final cost of the device. In fact, electronics accounts for approximately 20% of the manufacturing cost, while it often approaches 80% for photonics [30].

1.3.1 Electronic Packaging

Electrical powering of the PICs components is achieved and controlled through an external EIC.

The ideal solution to reach mass production for the integration of either an EIC and PIC functionalities over a single chip is monolithic integration. This milestone has been achieved in 2015 by MIT [31] were a CMOS compatible monolithic integration was proven on a sub-100nm SOI wafer. However, this approach is far from being widely accessible, and for medium-volume production the vertical integration of an EIC over a PIC can be cheaper, as various CMOS nodes can be employed [23].

In particular, the footprint of a PIC is usually between 10-30 mm^2 due to the wide dimension of photonic structures such as AWGs, and the space needed to place the optical-connections. Thus, the possibility of allocating an external EIC, which typically displays lower area, is fundamental to fill the whole PIC area.

This is important to avoid wasting the empty space on the more expensive CMOS node, significantly reducing the final cost.

The vertical integration is achieved mainly exploiting two different types of bumps: solder ball or copper-pillar bumps, respectively called (SBBs) and (CPBs), with diameters of roughly 10μm for SBBs and 30μm for CPBs. These interconnections allow to obtain a 2.5D integration strategy and each bump acts as an electrical, mechanical, and thermal interface at the same time.

Vertical integration enables to obtain a performing electric interface exploitable also for high-speed electronics, reducing the parasitic induction effects [23]. These, on the contrary, affect the wire-bonding approach, which is based on long curved metal wires, with length of hundreds micrometres.

Moreover, the mechanical SBBs or CPBs connections enable the integration of various different technologies, such as micro-electro-mechanical systems, or MEMS.

Usually, the EIC is vertically integrated performing an active alignment of the SBBs or CPBs pattern with the specular one on the PIC surface through the so-called flip-chip technique. The latter is done using a beam-splitter camera, which enables to overlap the PIC and EIC surfaces in real-time.

Then, the two chips are brought into physical contact and thermo-compression as well as solder-reflow enable to fuse the two chips together. The flip-chip bonding process is quite delicate as it can lead to extra losses due to the chemical residue, which can potentially compromise the quality of the optical connections.

To avoid such issues, a so-called “no clean” flux is used during the solder-reflow bonding [23]. The quality of the final bonding is usually tested on site directly performing electrical resistance measurements. Moreover, X-ray microscopy can be applied to obtain an image of the soldered bumps. Figure 6 shows a vertical-integrated EIC onto the SOI-PIC via CPBs interconnections.

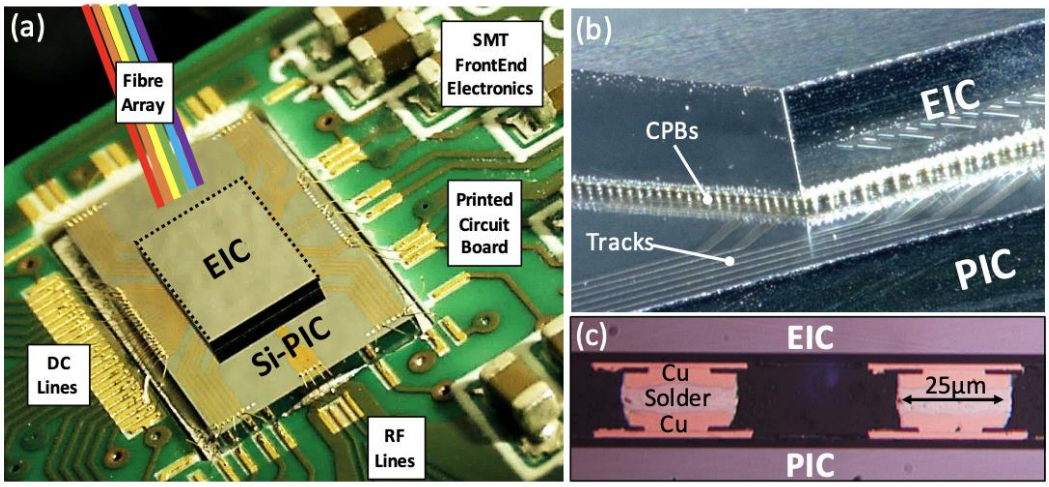

Figure 6: Vertical integration of an EIC over a SOI-PIC: (a) picture of a packaged photonic device, (b) EIC flip-chipped and soldered onto the PIC surface via copper-ball-bumps (CPBs), (c) microscope image of two CPBs with a typical diameter of 25µm. The images have been taken from [23].

1.3.2 Thermal Packaging

Photonics structures are quite sensitive to thermal variation that can dramatically compromise the functionality of the photonic device by changing the optical properties of the media involved.

As stated in the previous section, controlled thermal variation can be introduced on purpose to create electro-optical modulators.

However, the external environment does not show stable temperature conditions, which change significantly either across the Earth and throughout the year. In particular, a variation of 20° is sufficient to completely detune the functional behaviour of a PIC, resulting in a dramatic failure of performing any required action.

Moreover, even inside a temperature stable environment such as a laboratory, the thermal fluctuations due to the heat produced by the active components, such as optical amplifiers and laser, represent a serious issue for a SOI-PIC.

Typically, the stabilization in temperature is reached through a thermo-electric cooler (TEC), which is based on the Peltier effect, controlled externally and place in

close contact with the PIC surface. The TEC allows to dissipate the heat away from the PIC.

The usual thermal structure is developed vertically below the PIC and the integrated EIC. Here, part of the electric power delivered to the EIC is transformed into thermal power, due to the Joule-effect, and it is transferred trough the SBBs and CPBs connections to the PIC. The bottom surface of the PIC is connected to a heat-spreader plate, directly in contact with the cold side of the TEC. From there, the heat is conducted to a base-plate where it can be dissipated exploiting convection or conduction processes. Figure 7 shows the vertical structures used to dissipate the heat form the PIC surface gaining a thermal stabilization of the entire device.

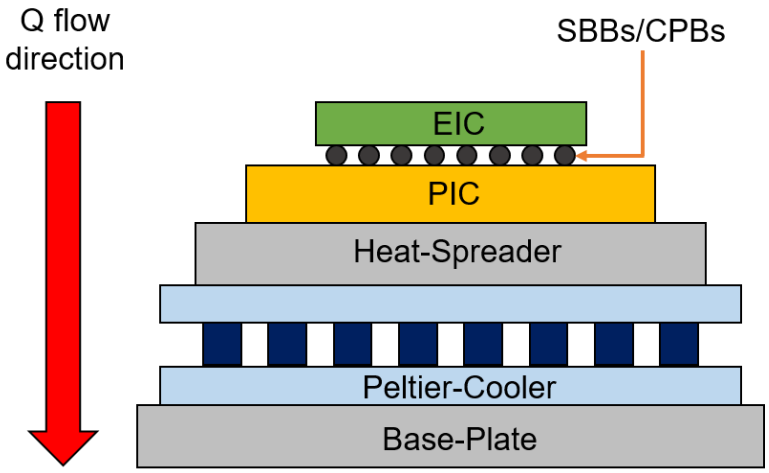

Figure 7: Vertical structure for thermal management. The heat (Q) is dissipated from the structure flowing from the EIC to the Base-Plate, passing through the PIC, the heat spreader, and the Peltier-cooler. Then, the heat is removed through convection and/or conduction processes. The image is taken from [23].

1.3.3 Optical Packaging

The optical packaging aims to the efficient and control in- and out-coupling of light from a PIC. Here, the main challenge faced is the Mode Field Diameter (MFD) mismatch between the modes of the WGs of the PIC and the one related to the optical interconnections used to inject and collect the light beam form the PIC.

For telecom and datacom applications, SMFs are used as optical interconnections, and the MFD associated to their mode, at 1550nm in the C-band, is 10.4μm.

However, the WG cross-section of a SOI PIC is 0.45μm wide and 0.22 μm height, see Figure 8. Thus, the poor overlap between the two modes result in high insertion losses and, consequently, low efficiency.

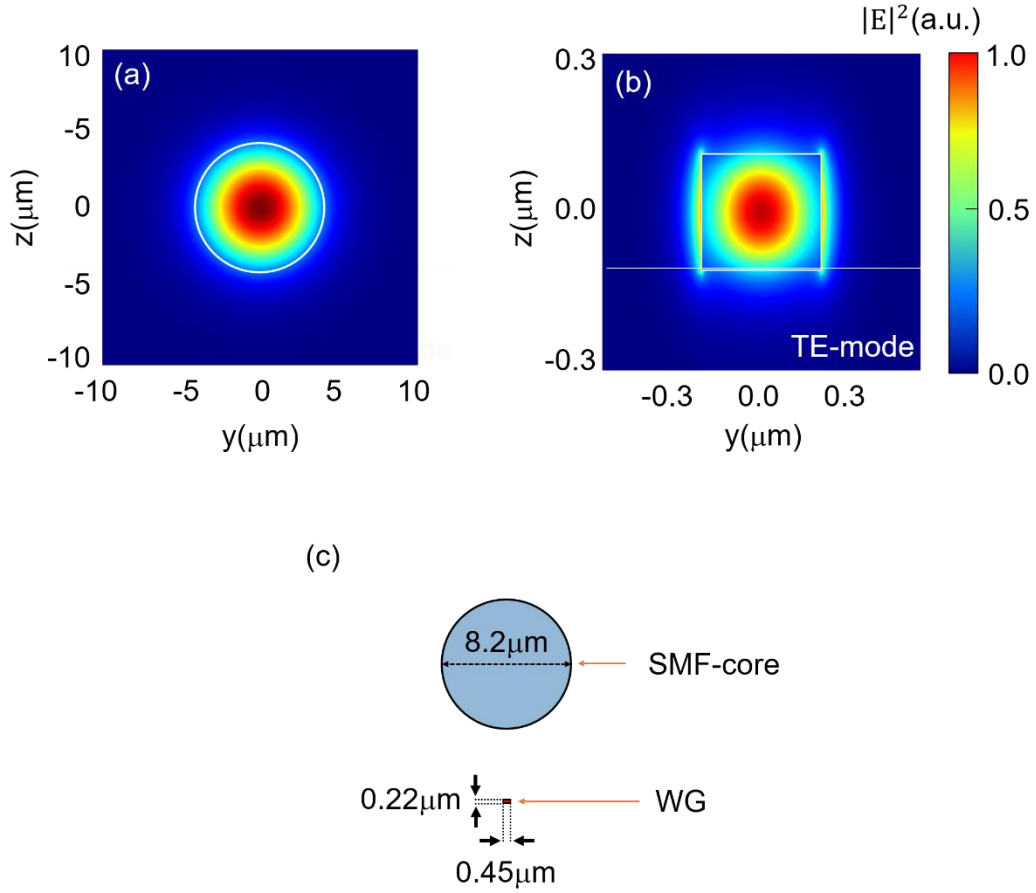

Figure 8: (a) Intensity profile of the fundamental SMF mode calculated at λ=1550nm. The white line points out the fibre core. (b) Intensity profile of the fundamental TE-mode of the SOI-WG with a 0.22μm height and 0.45μm width, calculated at λ=1550nm. (c) Comparison of the SMF core and the SOI-WG dimensions.

Indeed, the optical design is fundamental to optimize the photonic structure guaranteeing an efficient mode-matching, and reducing the overall fabrication cost of the final structures. In fact, the fabrication of a high-number of different designs characterized by diverse geometrical parameters with the scope of seeking for the best photonic structure is either time consuming and, above all, prohibitive in terms of final cost. Moreover, the optical design is fundamental to obtain optimized structures, which meet the constrains of the desired fabrication process leading to a buildable final device.

This is really vital, for instance, if someone is targeting MPW runs as well as standard optical photonics packaging procedures to maintain a low cost of the final photonic device, essential aspect for mass-production.

In order to overcome such issue, optical packaging exploits four different coupling strategies:

- Edge coupling

- Evanescent coupling
- Photonic-wire bonding
- Grating coupling

and, in particular, my thesis focuses on grating-coupling. These strategies allow to interpose additional photonics structure/structures to match the two different MFDs allowing for an efficient transfer of energy between the two modes.

Each coupling strategy has its own pros and cons, and the choice should be made taking into account the specific application.

Edge Coupling

Edge coupling is a well-established technique used in photonics packaging as it guarantees: (i) low-insertion losses, *i.e.* high-coupling efficiency, below 1dB, (ii) broad-bandwidth, hundreds of nm, and (iii) polarization independence.

A typical edge coupler is based on an inverse tapered SOI WG, where the width is changed adiabatically from 450/500nm down to tens of nanometres.

The tapering allows for the progressive reduction of the confinement of the WG mode, with the consequent reduction of its effective refractive index, increasing its effective cross-section.

Thus, the mode can be transferred with low insertion losses to a wider symmetric WG, called Spot Size Converter (SSC), with dimensions typically of the order 3μm x 3μm. This results in an expansion of the initial MFD.

The optical media of the SSC are usually Polymer, Si_3N_4, or SiON, with lower refractive index with respect to Si [32].

Figure 9 shows a sketch of an adiabatic SOI-WG coupled to a SSC.

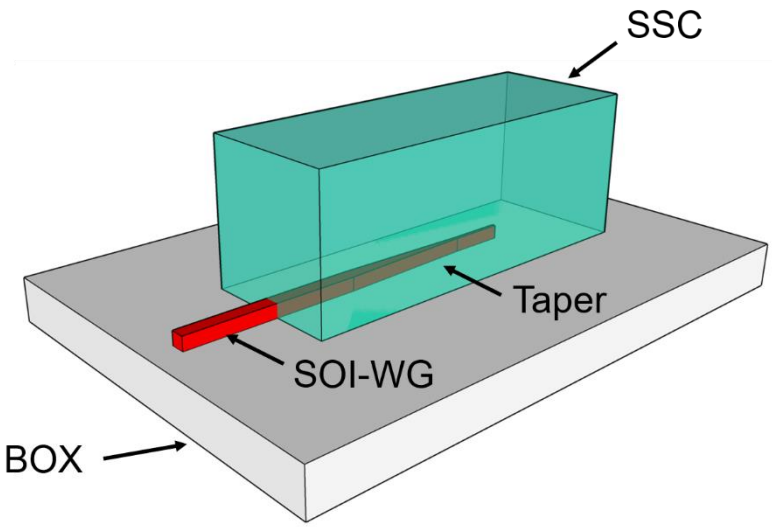

Figure 9: Edge coupler with Spot-Size-Converter (SSC) and an adiabatic tapered SOI-WG. The BOX layer has been also indicated for sake of completeness.

Thus, the expansion of the MFD allows to directly couple the SSC WG-mode into a lensed SMF, which has a tapered-tip in order to guarantee the required mode-matching condition between the incoming and receiving MFDs.

The quality of the coupling-process depends on various parameters: (i) the quality of the SSC facet, the higher the quality, the lower the back-reflection at the interface, (ii) the overlap integral between the incoming and receiving mode profiles, (iii) the quality of the mode conversion related to the adiabatic tapering process.

The adiabatic condition can be achieved if the spreading of the taper side walls is slower compared to the diffraction spreading of the WG fundamental mode [33]. From the mathematical prospective, the previous condition is described by the following Eq.

1

1

$$\theta < \frac{\lambda_0}{2Wn_{eff}}$$

where θ is the local angle, at a distance x, of the side walls, λ_0 is the wavelength in vacuum, *e.g.* 1550nm, W is the local full width of the taper at a distance x, and n_{eff} is the effective refractive index of the corresponding WG mode at x, as reported in Figure 10.

The simplest tapering is done through a linear variation of the sidewall width, i.e. the angle θ is unique. To reach an adiabatic conversion, the length should be of the

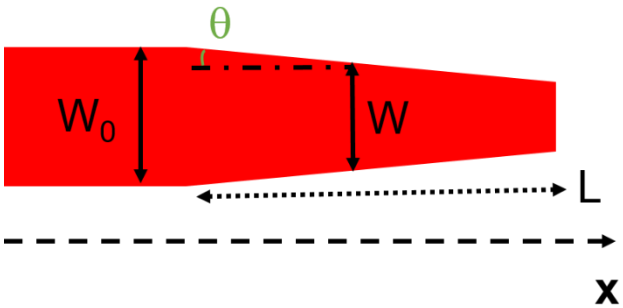

Figure 10: Inverse tapered WG: W_0 is the initial width of the WG, W is the local width at x, θ is the local angle, and L is the total length of the taper.

order of hundreds of microns to reduce almost to zero the insertion losses. However, this is not suitable for Integrated Photonics as the miniaturization of the structure dimension is an important aspect to guarantee small final photonic devices.

Nevertheless, with this type of configurations, efficiencies of the order of 90% have been demonstrated with an almost flat spectral response, i.e. bandwidth of 300nm [34]. Here, the authors exploited e-beam lithography to create the tapered WG as the dimension of the final tip is a fundamental parameter to enable a better transfer of energy from the SOI-WG and the SSC.

Furthermore, the use of lensed fibers for this coupling scheme can be avoided thanks to wider SSC. Up to now, there are few designs that enables to expand the SOI-WG mode in order to obtain a final MFD of 6 or even 10 μm, allowing to use directly standard SMFs, which are cheaper than the lensed counterpart [35]. Here, the SSCs are based on more complicated designs made of multi-layered WGs where two optical materials, such as SiO_2 and Si_3N_4, are interlaid with thickness values optimized depending on the desired MFD.

Besides the excellent performances of edge coupling, the major downsides of this coupling scheme are the high-cost related to the post-process fabrication steps needed to obtain high-quality flat facets. In particular, the cleavage of the SSC facet is not a trivial task.

In addition, edge-couplers can be quite bulky and such structures can be placed only at the edges of the PIC making impossible the in- and out-coupling of the light signal from any position on the PIC surface [36].

From the packaging prospective, edge couplers are quite sensitive to any in-plane misalignment between the SSC and the SMF. Usually, the 1dB alignment tolerances are less than half a micron making challenging the packaging procedures even inside

a dedicated laboratory. This results in time consuming active alignment processes [23].

However, recently, 3D printed polymer free-form μlenses were proposed as a possible solution to relax the alignment procedure [37], guaranteeing at the same time high-efficiencies. Figure 11 shows the edge coupling scheme assisted through free-form μlenses.

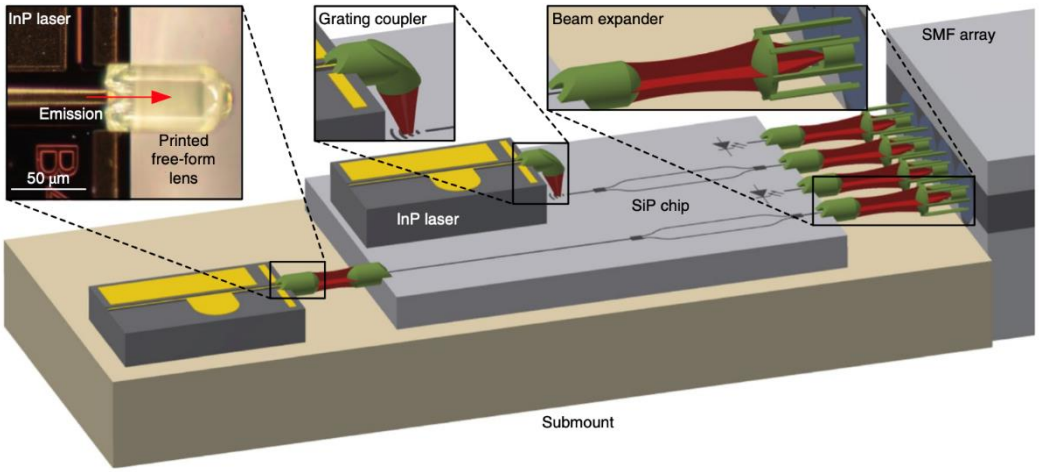

Figure 11: 3D printed free-form μlenses for in and out coupling of a light beam. The lenses are employed to collect and expand, and collimate the travelling beam relaxing the alignment tolerances. The figure is taken from [37].

Evanescent Coupling

The past decade has seen also the development of a new-coupling strategy called evanescent coupling. This strategy exploits the transfer of the energy between two separate WG using their evanescent field, *i.e.* the tail of the confined modes associated to the exponentially decaying unconfined electromagnetic field.

Evanescent -coupling has been well known and exploited as a coupling strategy between III-V optical amplifier and SOI-WGs with discrete efficiency [38].

The first high-efficient evanescent-coupler was demonstrated by IBM in 2015 [39]. As in edge-coupling, an inverse tapered WG is used to extract the mode form the SOI-PIC, which now is not transferred into a SSC, but into a second polymer WG on a new separate optical-chip in close proximity with the PIC surface. In this way, the refractive index and the MFD of the new optical-chip can be easily tailored in order to match the one of a SMF and enabling for an efficient two step fibre-to-PIC coupling. The efficiency of the coupling-process between the SOI WG and the polymer WG has been demonstrated to be higher than 80%.

In 2018, IBM published a new work related to evanescent coupling where the entire optical connectors were fabricated reporting a fiber-to-chip CE of 45% (3.5dB) at 1310nm, *i.e.* in the O-band. The SOI-PIC was integrated with the new optical chip exploiting the flip-chip bonding technology, as shown in Figure 12 [40].

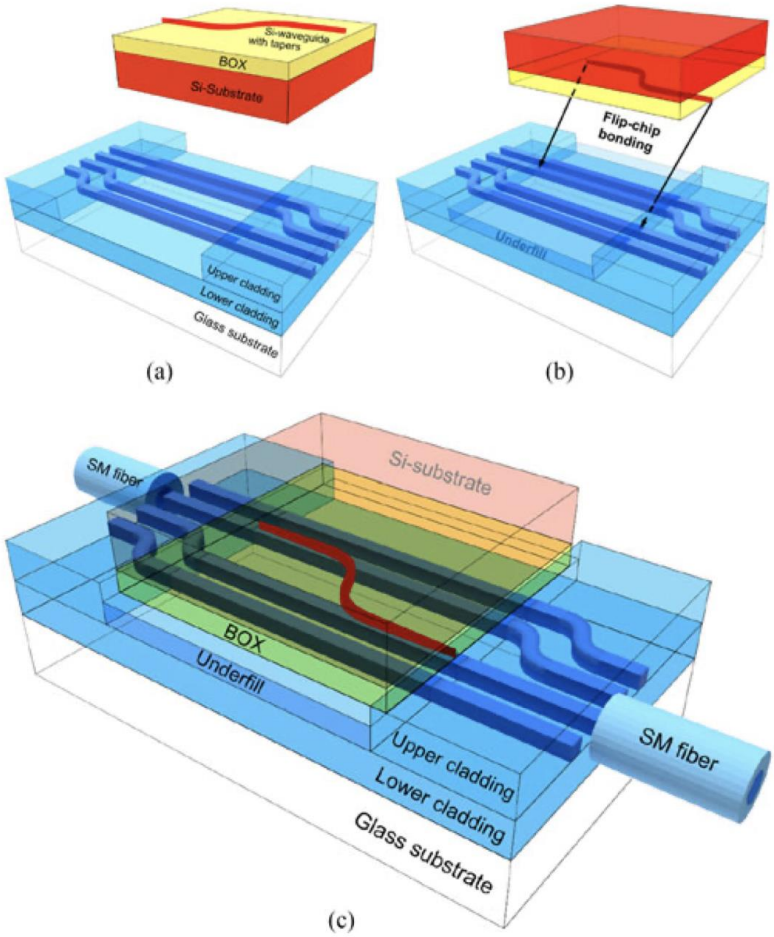

Figure 12: Evanescent optical connector: (a) the SOI-PIC with the tapered WG for adiabatic coupling, red WG, and the second optical-chip with the wider polymer WG, dark blue WGs (b) Flip-chip of the SOI-PIC onto the optical-chip, (c) image of the entire connector where the polymer WGs are edge-coupled to two separate SMFs. The figure has been take from [40].

The great advantages of this coupling strategy, aside from good CE, are the broadband optical spectra, with wide bandwidth, and low polarization sensitivity. Moreover, the alignment tolerances are more relaxed compared to edge coupling, of the order of ±2μm for 1dB alignment tolerances.

Finally, evanescent coupling offers the possibility to inject and extract the light signal from everywhere on the PIC surface, with the only constrains of the presence of an adiabatic tapered WG. Again, the major downside of this technique is represented by the need of long adiabatic taper, not suitable from a technological

prospective. In fact, IBM exploited millimetre-length linear adiabatic tapers to achieve an excellent adiabatic process.

Photonic-wire bonding

Photonic-wire bonding is inspired by electrical wire bond connections where a metal wire is used to connect two separate pins of a circuit allowing to circulate electric current. Here, the metal wire is substituted by a polymer WG, directly attached either to the light source and the receiver, in order to directly coupled the travelling light beam, see Figure 13.

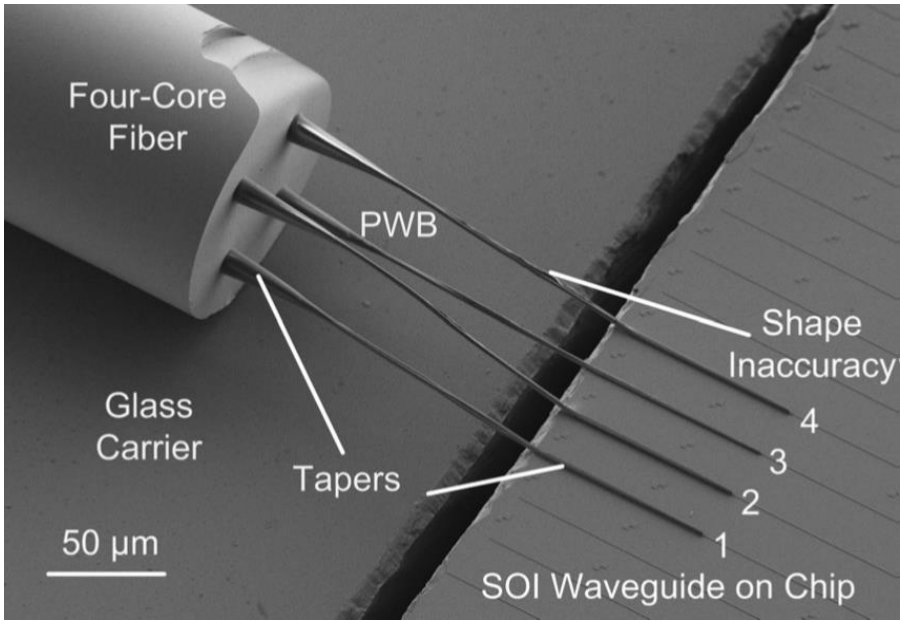

Figure 13: Photonic-wire bonding between a four-core fiber and SOI WGs. The image has been taken from [41].

This technology has been successfully demonstrated for coupling between SMF and inverse tapered SOI-WGs with high CE and flat spectral response [41].

The photonic wire bond is directly written into the optical material, i.e. polymer resist, exploiting a fs laser, allowing for precise control of its geometrical features.

This coupling strategy is quite interesting from a packaging prospective has no active alignment is needed, and display low material cost potentially targeting mass-production. Nevertheless, photonic wire bonds are a quite new technique and great effort is currently made by the research community to develop a fast writing process of such photonics structures.

Grating coupling

Grating coupling, with edge coupling, is the most exploited coupling strategy due to its several technological advantages, to name a few: (i) high CEs, (ii) relaxed alignment tolerances, (iii) the possibility of placing such structures anywhere on the PIC surface.

Here, a periodic structure is directly etched down into the SOI layer enabling the in- and out-coupling of the impinging light beam, see Figure 14.

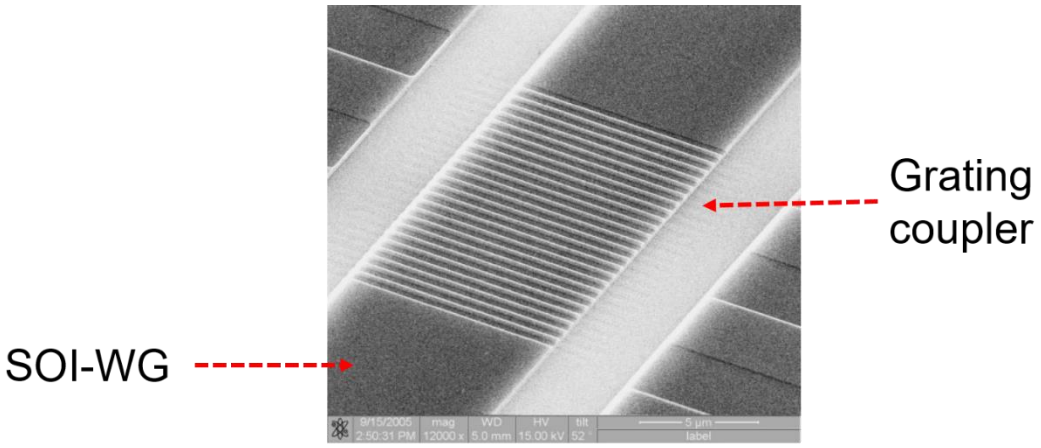

Figure 14: SEM image of a uniform grating coupler. The image has been taken and adapted from [42].

Grating coupling is one of the first proposed scheme for fiber-to-PIC coupling for telecom applications; nevertheless, the optimization of optical connections based on this strategy is currently considered an active and attractive research field.

In particular, grating coupling represents the core concept of this work. The thesis is focused on the design, optimization, packaging, and testing of a specific grating structure, called non-uniform grating coupler, for a horizontal fiber coupling scheme. Therefore, a detail introduction to grating-coupling, starting from the theory behind this coupling strategy, is presented in the following Chapter 2.

1.3.4 System requirements for Photonics Packaging

The typical system requirements of a photonics packaging laboratory need to fulfil a broad spectrum of operations across the three branches: electrical, thermal, and optical.

In this frameworks, optical connections need alignment tolerances down to half a micron and two separate machines, able to satisfy such requirements, are currently employed in the photonics packaging laboratory at Tyndall National Institute: (i) the

Nanosyntec NanoGlue machine, and (ii) a customize auto-aligner with motorized stages made by Newport.

The Nanoglue machine is a multi-task advanced workstation realized for the alignment of optoelectronic components such as laser diodes, VCSEL, waveguides, and lens arrays. Figure 15 panel (a) shows a picture of the machine where the different building-blocks are pointed out.

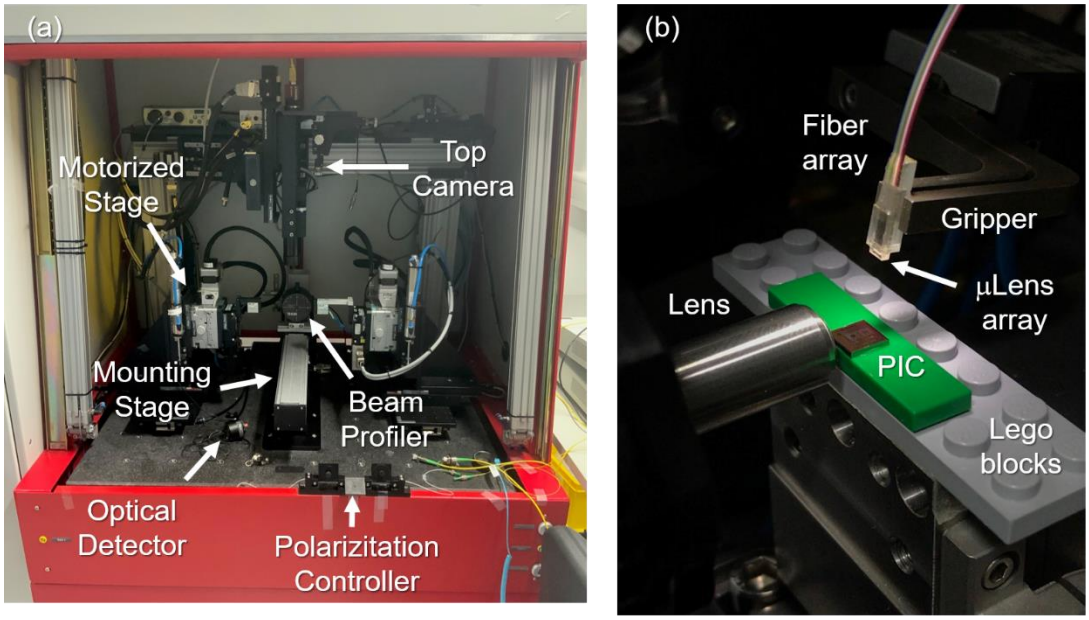

Figure 15: (a) Picture of the Nanosyntec Nanoglue machine. (b) Closed-up image of the mounting stage. Here, a fiber array, with a μLens array attached to its facet, is actively aligned to couple the light beam into a PIC. A lens is aligned in front of the PIC facet to collect the emission from one of the PIC WG.

Two motorized stages, controlled through an external computer, are used to perform the alignment process exploiting built-in algorithms to achieve a good active pre-alignment, reducing the time needed to complete such procedure. Moreover, a top camera is used for advanced machine vision.

The motorized stages have six degrees of freedom, three linear axes related to the three spatial directions, and three rotary axes for the corresponding angular rotations, which angles are called pitch, roll, and yaw. The nominal resolution for the linear axes is 20nm, and for the rotary axes 0.0005°. Specific gripping tools can be mounted on the motorized stages to pick-up the optical components, such as optical fibers or lens arrays.

Typically the PIC is loaded onto external trays on a loading station, which is then secured on the mounting stage, see Figure 15 panel (b). The machine is mounted on a stabilized optical table where different components like optical detectors and

polarization controllers can be allocated. Furthermore, the Nanoglue machine can be customized by adding external components, such as a slit optical beam profiler, enabling to go beyond the alignment process.

The Newport auto-aligner is an advanced packaging machine used for fiber-to-fiber, fiber-to-laser, or fiber-to-PIC alignment. In particular, it is the machine that I used to perform the measurements for my thesis work. Figure 16 panel (a) shows a picture of the auto-aligner.

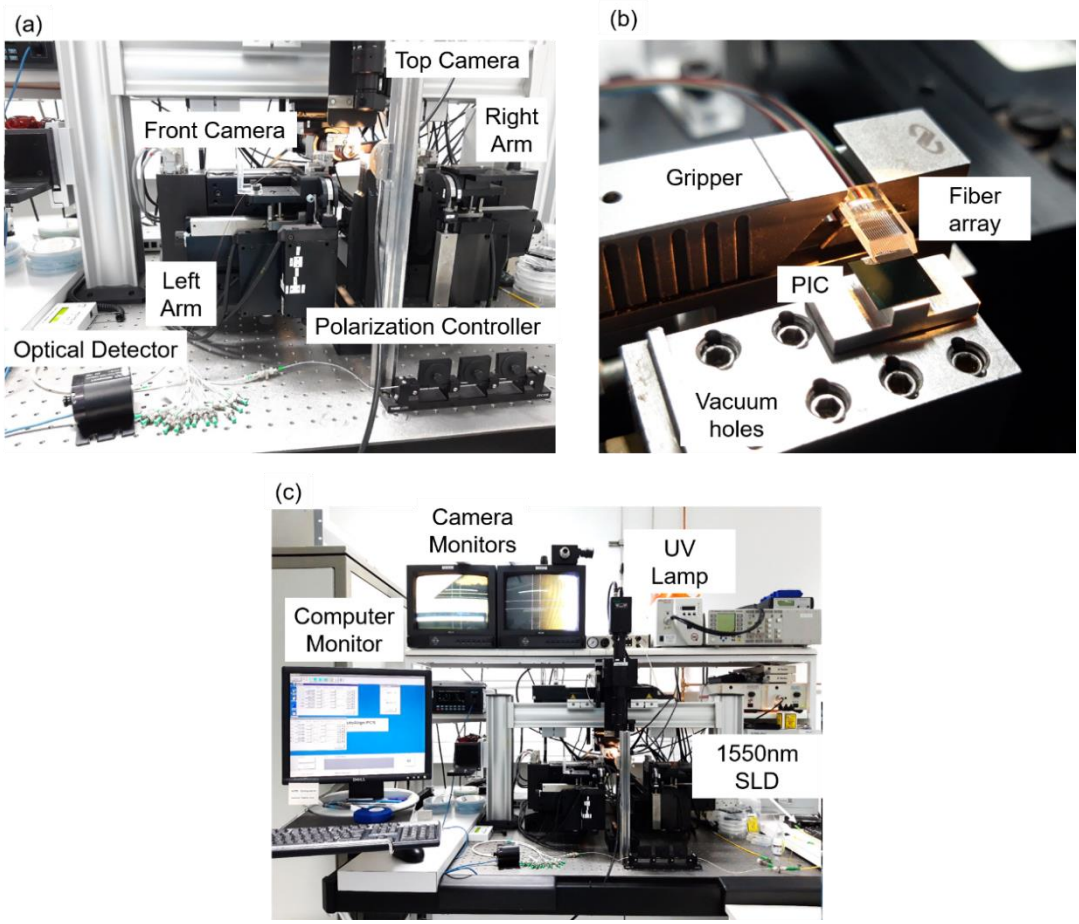

Figure 16: (a) Auto-aligner image, where the left- and right- arms are pointed out together with the top- and front-cameras. The optical detector and the polarization controller used during the campaign of measurements are also indicated. (b) Closed-up image of the central stage. A fiber array is directly mounted on the arm through the gripper to actively align it onto the PIC. The latter is kept in place by vacuum. (c) Broad overview of the auto-aligner machine with the Computer Monitor used to control the machine, the 1550nm superluminescence laser diode (SLD) light source, the camera monitors, and the UV lamp.

The machine is made of two motorized stages, called left and right arm, and two motorized cameras, called front and side camera. The arms are characterized by six degrees of freedom, as the Nanoglue machine, three linear axes and three rotary axes. The resolution of the linear axes is below half a micron, while the one related to the rotary axes is 0.01°. In particular, optical fibers are secured mechanically either

through customized tools to the arms or directly to the arm gripper, see Figure 16 panel (b).

By controlling separately the six degrees of freedom the alignment processes can be performed. Here, the photonic chip is mounted on a central stage, placed between the arms, and the position of the PIC is kept stable applying vacuum. The latter is created exploiting an external pump directly connected to the central stage.

The top and front cameras have three degrees of freedom, *i.e.* the three spatial directions, and ensure machine vision to see in real time, either from the top and the side, the alignment between the fiber and the PIC surface through the camera monitors, see Figure 16 panel (c).

This is vital as it allows to monitor the distances between the different objects avoiding damages due to uncontrolled physical contact, as well as to see the mutual positions of the objects. Either the arms and the cameras are controlled exploiting the auto-aligner software, see computer monitor in Figure 16 panel (c). This allows to exploit built-in algorithms to perform quickly the active pre-alignment. The entire machine is positioned above a stabilized optical table where addition optical components can be secured, such as optical detectors, or polarization controllers.

After the alignment process, optical fibers are mechanically attached to the PIC surface exploiting optical Epoxies, see Figure 17 panel (a),

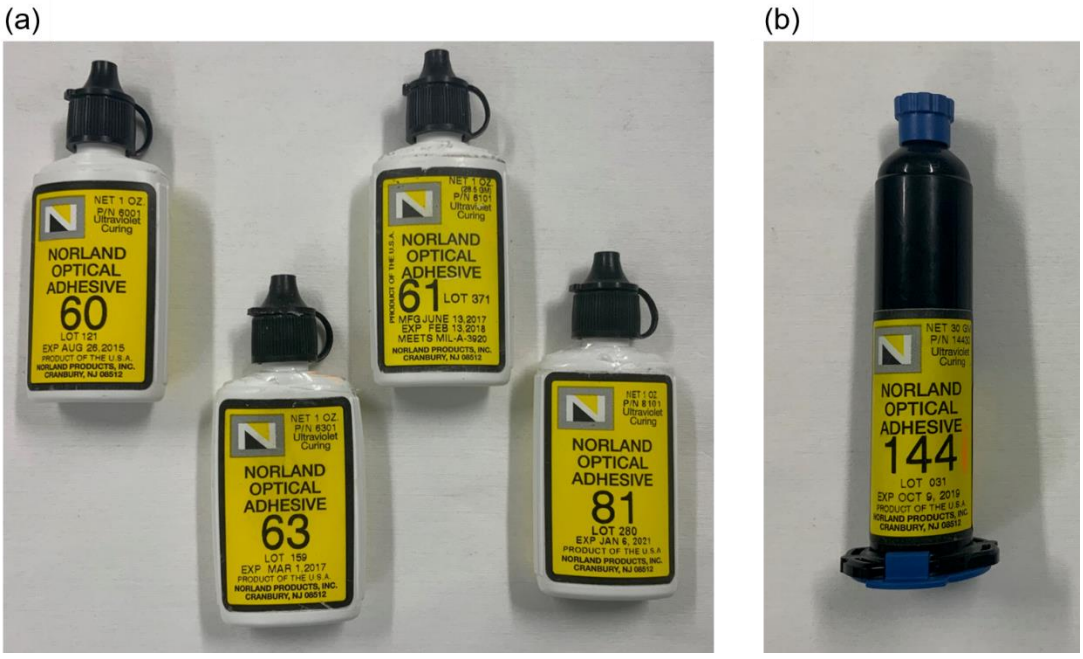

Figure 17: (a) Various Norland optical Epoxies with different mechanical and optical characteristics. (b) Norland NOA144 Epoxy.

which are liquid resins with specific mechanical, thermal, and optical properties.

The choice of the Epoxy is not straightforward and it is strictly linked to the materials involved in the packaging process. For example, the adhesion to a glass, metal, or plastic surfaces changes between the different Epoxy, important aspect to consider before performing the packaging processes.

In this context, the hardness of the Epoxy is another important feature to take into account to guarantee the mechanical robustness of the final packaged device.

The optical properties of such resins are vital as the Epoxy are used for index matching purposes. This guarantees to avoid back reflections at the different material interfaces. Thus, Epoxies come with a vast choice of refractive indexes from 1.7 down to 1.3 in order to match the refractive index of the majority of glasses, for instance BK7 or SiO_2.

In particular, a specific Epoxy with a refractive index of 1.44 can be used to fill the air gap between an optical fiber and the TOX surface of a SOI-PIC reducing the losses due to the index mismatch. As the Epoxies are typically applied manually, the viscosity of such resins must be considered during the packaging processes. The lower the viscosity, the easier the application and the spreading of the liquid between two surfaces.

Figure 17 panel (b) shows the Norland NOA144, which is the optical Epoxy used to perform the measurements reported in this thesis. NOA144 is indicated for bonding glass and shows wide transparency widow in the infrared with a refractive index of 1.44, suitable for fiber-to-PIC bonding. In particular, this Epoxy has a low viscosity resulting in being particularly liquid and easy to apply between a fiber array and a PIC surface.

Finally, these optical adhesives are cured exploiting UV light; thus a UV lamp is typically placed close to the packaging machine in order to fulfil easily this task, see in Figure 16.

During the UV curing, it is important to consider the shrinkage of the Epoxy, which can affect the quality of the alignment between the fiber array and the PIC. To overcome such problem, the alignment can be adjusted actively during the curing to guarantee the best coupling condition of the final device.

1.4 Conclusion

Chapter 1 represents an introduction to my thesis work. A broad summary of Silicon Photonics is provided with particular attention to Integrated Silicon Photonics. Here, a definition and a description of SOI-PICs is given together with a general overview of the main photonic passive and active structures typically integrated inside it.

Particular attention on the technological aspect has been highlighted through the description of the current services offered by organizations, such as Europractice starting from the fabrication of the SOI-PICs to the final photonics packaging services.

In this context, an extend introduction to this research field has been reported underling the technological importance of photonics packaging and the working principles behind it, summarized in Figure 5.

Then, an overview of the electrical, thermal, and optical packaging is provided with particular attention on this last one, as the main argument of this work.

In this context, a summary of the state of the art regarding the main coupling schemes currently used in photonics packaging is reported. Particular attention on their operational behaviour and technological advantages and disadvantages is addressed as well.

Moreover, a general overview of the system requirements of a photonics packaging laboratory for optical packaging processes is done. Here, the two main machines used in the packaging lab at Tyndall, the Nanoglue and the auto-aligner, are described with particular attention on the last one, which is the one used to perform the measurements reported in this wok.

Finally, a brief introduction to optical Epoxies and their importance in photonics packaging processes is provided.

Bibliography

[1] Günther Roelkens, et al., “III-V/silicon photonics for on-chip and inter-chip interconnects,” *Laser Photonics Review,* vol. 4, no. 6, p. 751–779, 2010.

[2] Richard A. Soref, and J. P. Lorenzo, “Single-crystal silicon: a new material for 1.3 and 1.6 μm integrated-optical components,” *Electronics Letters,* vol. 21, no. 21, p. 953 – 954, 1985.

[3] B. N. Kurdi, and D. G. Hall, “Optical waveguides in oxygen-implanted buried-oxide silicon-on-insulator structures,” *Optics Letters,* vol. 13, no. 2, pp. 175-177, 1988.

[4] Dennis G. Hall, “The role of silicon in integrated optics,” *Optics News,* vol. 14, no. 2, pp. 12-15, 1988.

[5] Joachim Schmidtchen, et al., “Low loss integrated-optical rib-waveguides in SOI,” in *1991 IEEE International SOI Conference Proceedings,* Vail Valley, CO, US, 1991.

[6] Andrew Rickman, et al., “Low-loss planar optical waveguides fabricated in SIMOX material,” *IEEE Photonics Technology Letters,* vol. 4, no. 6, pp. 633 - 635, 1992.

[7] Andrew Rickman, and Graham Reed, “Silicon-on-insulator optical rib waveguides: loss, mode characteristics, bends and y-junctions,” *IEE Proceedings - Optoelectronics,* vol. 141, no. 6, p. 391 – 393, 1994.

[8] G. Treyz, et al., “Silicon Mach–Zehnder waveguide interferometers based on the plasma dispersion effect,” *Applied Physics Letters,* vol. 59, no. 7, pp. 771-773, 1991.

[9] Zhou Fang and Ce Zhou Zhao, “Recent Progress in Silicon Photonics: A Review,” *International Scholarly Research Notices,* vol. 2012, pp. 1-27, 2012.

[10] Leonid Tsybeskov, “Silicon Photonics: CMOS Going Optical [Scanning the Issue],” *Proceedings of the IEEE,* vol. 97, no. 7, pp. 1161-1165, 2009.

[11] H. H. Li, “Refractive index of silicon and germanium and its wavelength and temperature derivatives,” *Journal of Physical and Chemical Reference Data,* vol. 9, no. 3, pp. 561-658, 1980.

[12] I. H. Malitson, “Interspecimen Comparison of the Refractive Index of Fused Silica,” *Journal of the Optical Society of America,* vol. 55, no. 10, pp. 1205-1209, 1965.

[13] Lorenzo Pavesi, “Will silicon be the photonic material of the third millenium?,” *Journal Of Physics: Condensed Matter,* vol. 15, no. 26, p. R1169–R1196, 2003.

[14] Amir H. Atabaki, et al., “Integrating photonics with silicon nanoelectronics for the next generation of systems on a chip,” *Nature,* vol. 556, p. 349–354, 2018.

[15] Enxiao Luan, et al., “Silicon Photonic Biosensors Using Label-Free Detection,” *Sensors,* vol. 18, no. 10, pp. 3519(1-42), 2018.

[16] John E. Bowers, et al., “Recent advances in silicon photonic integrated circuits,” in *SPIE OPTO,* San Francisco, CA, US, 2016.

[17] Callum Littlejohns, et al., “CORNERSTONE’s Silicon Photonics Rapid Prototyping Platforms: Current Status and Future Outlook,” *Applied Sciences,* vol. 10, no. 22, pp. 8201(1-34), 2020.

[18] John D. Joannopoulos, Photonic Crystals: Molding the Flow of Light (second edition), Princeton, New Jersey, US: Princeton University Press, 2008.

[19] Liam O’Faolain, et al., “Dependence of extrinsic loss on group velocity in photonic crystal waveguides,” *Optics Express,* vol. 15, no. 20, pp. 13129-13138, 2007.

[20] Dajian Liu, et al., “Silicon photonic filters,” *Microwave and Optical Technology Letters,* pp. 1-17, 2020.

[21] Jan Niehusmann, et al., “Ultrahigh-quality-factor silicon-on-insulator microring resonator,” *Optics Letters,* vol. 29, no. 24, pp. 2861-2863, 2004.

[22] Daoxin Dai, et al., “Monolithically integrated 64-channel silicon hybriddemultiplexer enabling simultaneous wavelength-and mode-division-multiplexing,” *Laser & Photonics Review,* vol. 9, no. 3, pp. 339-344, 2015.

[23] Lee Carroll, et al., “Photonic Packaging: Transforming Silicon Photonic Integrated Circuits into Photonic Devices,” *Applied Sciences,* vol. 6, no. 12, pp. 426(1-21), 2016.

[24] Richard A. Soref, and Brian R. Bennett, “Electrooptical Effects in Silicon,” *IEEE Journal of Quantum Electronics,* vol. 23, no. 1, pp. 123-129, 1987.

[25] Graham Reed, and C.E.Jason Png, “Silicon optical modulators” *Materials Today,* vol. 8, no. 1, pp. 40-50, 2005.

[26] Jeremy Witzens, “High-Speed Silicon Photonics Modulators,” *Proceedings of IEEE,* vol. 106, no. 12, pp. 2158-2182, 2018.

[27] Molly Piels, and John E. Bowers, “Photodetectors for silicon photonic integrated circuits,” in *Photodetectors,* Woodhead Publishing, 2016, pp. 3-20.

[28] Andy Eu-Jin Lim, et al., “Review of Silicon Photonics Foundry Efforts,” *IEEE Journal of Selected Topics in Quantum Electronics,* vol. 20, no. 4, pp. 405-416, 2014.

[29] Europractice, [Online]. Available: https://europractice-ic.com/packaging-integration/photonics-packaging/.

[30] Kevin Fogarty, and Ed Sperling, “Silicon Photonics Begins To Make Inroads,” Semiconductor Engineering , 2019. [Online]. Available: https://semiengineering.com/silicon-photonics-begins-to-make-inroads/.

[31] Miloš A. Popović, et al., “Monolithic silicon photonics in a sub-100nm SOI CMOS microprocessor foundry: progress from devices to systems,” in *SPIE OPTO,* San Francisco, CA, US, 2015.

[32] Riccardo Marchetti, et al., “Coupling strategies for silicon photonics integrated chips,” *Photonics Research,* vol. 7, no. 2, pp. 201-239, 2019.

[33] Yunfei Fu, et al., “Efficient adiabatic silicon-on-insulator waveguide taper,” *Photonics Research,* vol. 2, no. 3, pp. A41-A44, 2014.

[34] Sharee J. McNab, et al., “Ultra-low loss photonic integrated circuit with membrane-type photonic crystal waveguides,” *Optics Express,* vol. 11, no. 22, pp. 2927-2939, 2003.

[35] Martin Papes, et al., “Fiber-chip edge coupler with large mode size for silicon photonic wire waveguides,” *Optics Express,* vol. 24, no. 5, pp. 5026-5038, 2016.

[36] Xin Mu, et al., “Edge Couplers in Silicon Photonic Integrated Circuits: A Review,” *Applied Sciences,* vol. 10, no. 4, pp. 1538(1-29), 2020.

[37] Philipp-Immanuel Dietrich, et al., “In situ 3D nanoprinting of free-form coupling elements for hybrid photonic integration,” *Nature,* vol. 12, p. 241–247, 2018.

[38] Hsu-Hao Chang, et al., “1310nm silicon evanescent laser,” *Optics Express,* vol. 15, no. 18, pp. 11466-11471, 2007.

[39] Roger Dangel, et al., “Polymer waveguides for electro-optical integration in data centers and high-performance computers,” *Optics Express,* vol. 23, no. 4, pp. 4736-4750, 2015.

[40] Roger Dangel, et al., “Polymer Waveguides Enabling Scalable Low-Loss,” *IEEE Journal of Selected Topics in Quantum Electronics,* vol. 24, no. 4, pp. 8200211(1-11), 2018.

[41] Nicole Lindenmann, et al., “Connecting Silicon Photonic Circuits to Multicore Fibers by Photonic Wire Bonding,” *Journal of Lightwave Technology,* vol. 33, no. 4, pp. 755-760, 2015.

[42] Dirk Taillaert, et al., “Grating Couplers for Coupling between Optical Fibers and Nanophotonic Waveguides,” *Japanese Journal of Applied Physics,* vol. 45, no. 8A, pp. 6071-6077, 2006.

Chapter 2

Grating Coupling: Theory and Optimization Procedure

Diffraction gratings, optical components characterized by periodic grooves, are one of the most historical object used in Optics. Nowadays, they are fundamental components of our modern spectrometers and monochromators, but their invention can be brought back to the eighteenth century, when the first diffraction grating was created by David Rittenhouse using: "…a square of parallel hairs about half an inch each away" [1]. In this article, Rittenhouse described for the first time the operational behaviour of a diffraction grating in splitting a polychromatic incident beam into its different "colour" components pointing out: "…that the red rays are more bent out of their first direction, and the blue rays less; as if the hairs acted with more force on the red than on the blue rays, contrary to what happens by refraction, when light passes obliquely through the common surface of two different medium".

Today, this outcome comes with no surprise, as the well-known diffraction grating equation describes its dispersive behaviour linking the wavelength and the incident angle of the incoming light beam to the different angular positions at which each order of the grating, indicated as (m=0,±1,±2..), is diffracted deviating from the original travelling path. This is shown in Figure 16, for a monochromatic light beam at normal incidence with respect to the grating surface.

The diffraction from a grating is not only exploited by modern spectroscopy, but it is also attractive for current Integrated Photonics where diffraction gratings are currently used to couple light from an incident beam into a PIC, and in this framework they are addressed as grating couplers (GCs). These structures can be designed to direct the m=+1 order towards the PIC's waveguide suppressing the higher orders, which would represent a channel of loss. The fabrication of grating couplers is made

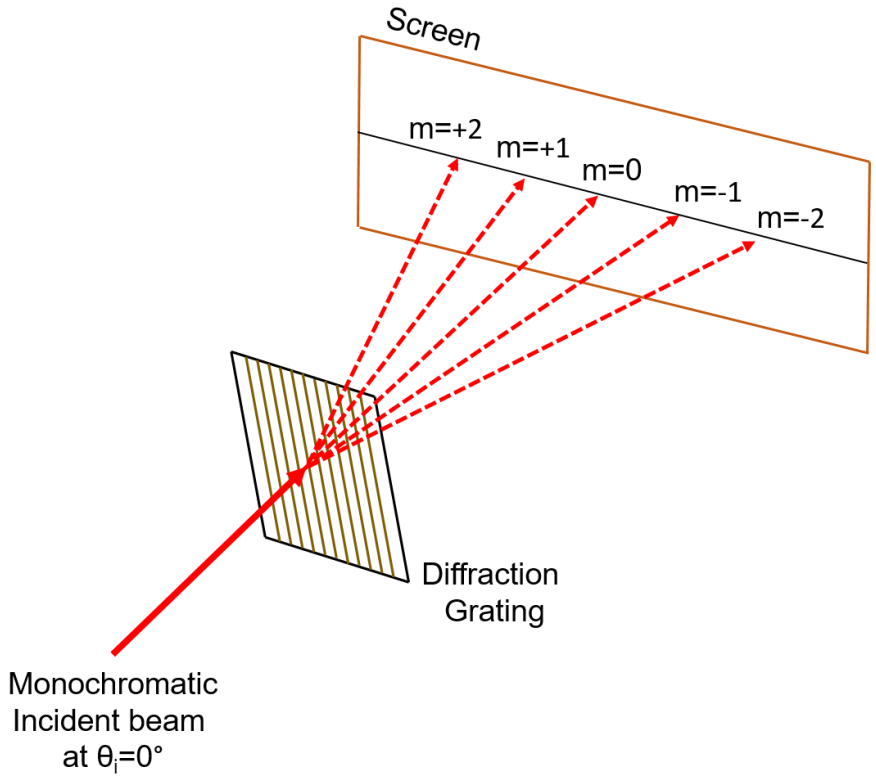

Figure 16: Operational behaviour of a diffraction grating: a monochromatic beam at normal incidence, i.e. $\theta_i = 0°$ is separated into its different diffraction orders, m=0,±1,±2… projected onto the screen.

possible thanks to the progress undertaken during the past decades by fabrication technologies, such as UV or deep UV-, and e-beam lithography, now capable of realizing small photonics structures with the required geometrical features, down to the nanometre scale [2, 3].

Historically, GCs were proposed as a coupling solution in Silicon photonics for telecom applications working in the C-band, thus at wavelengths around 1550nm [4, 5], exploiting the SOI technology, see Figure 14. Here, the light is brought to the GC surface via a SMF. Currently, Grating-Coupling is one of the major coupling-technique that constitutes the optical connections used in optical packaging [6]. In fact, they offer a few important technological advantages compared to other coupling techniques such as edge-coupling [6]: (i) usually one etching step is needed during the fabrication processes to create GCs, (ii) no need of additional fabrication processes, such as surface polishing or dicing at the PIC's edged to obtain high-quality facets (iii) due to their small footprints, thousands of structures can be harvested at the same time on the same surface, (iv) GCs can be placed everywhere enabling to couple light in and out from the PIC from almost everywhere, (v) GCs show quite relaxed in-plane

alignment tolerances of roughly ±2.5μm for 1dB penalty [7] with a SMF, see Figure 17, resulting in an easy active alignment procedure during the packaging processes.

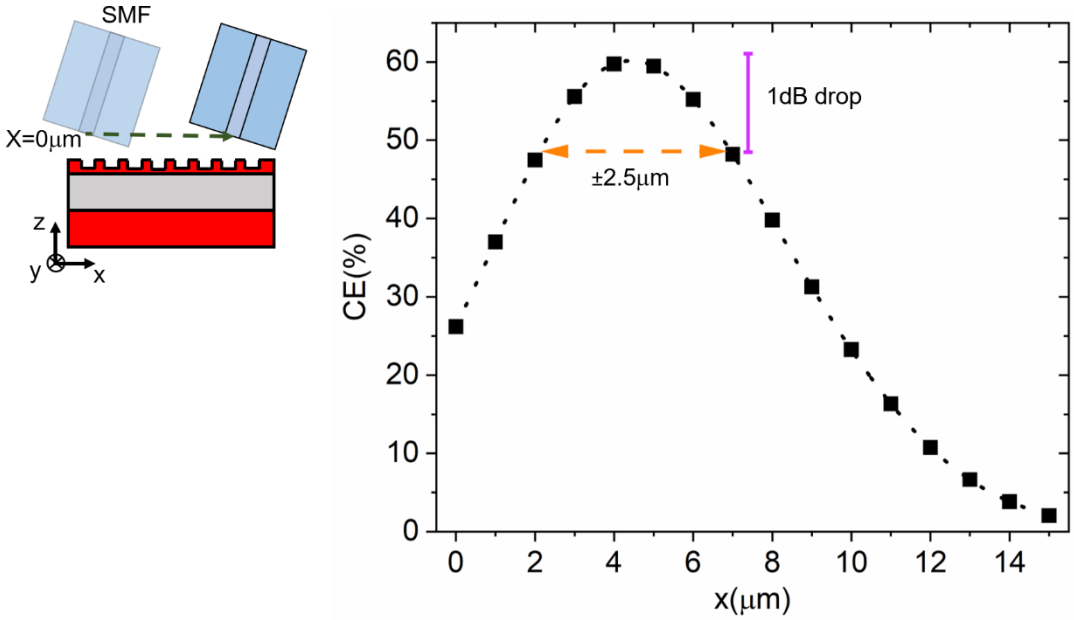

Figure 17: Reference plot of typical in-plane alignment tolerances for grating coupling with a single mode fiber (SMF).

Moreover, it has been demonstrated that the 1dB alignment tolerances can be further improved, up to ±30μm, using standard off-the-shelf μLens arrays opening the path to possible passive alignment of the fiber-to-PIC coupling geometry, leading to the realization of a pluggable photonic connector [8].

These aspects led GCs to establish themselves as a credible light coupling technique also for sensing applications, going beyond research purposes, resulting in being actual products currently available from Photonics foundries. GCs are not strictly limited to couple the MFD proper of a SMF emission; but in principle they might be optimized to work with different MFDs, which is a practical situation that often occur in Photonics Packaging. In this case, an appropriate GC structure has to be optimized through a proper design process in order to overcome additional losses.

Therefore, due to their technological importance, the impact of this achievement can be considered a valuable contribution to Integrated Photonics. This represents one the main topic of this research thesis. In particular, Chapter 2 is divided into the following sections: the first one is focused on general aspects related to the theory behind the physics of GCs and a general overview on the current state-of-the art; the second section is focused on the design routine developed in this research work.

In particular, before moving further, I would like to highlight that the GC designs optimized in this work for the 220nm-thick and 340nm-thick SOIs have been implemented as official PDKs by Cornerstone, the open source Silicon Photonic Foundry of the University of Southampton [9]. Moreover, Cornerstone is currently employing the GC design optimized for the 220nm-thick SOI for a photonic chip design, used for research purposes, in collaboration with ASML [10].

Finally, the same design has been introduced as an official component of the new PIXAPP Integrated Photonics Educational Kit (IPEK), shown in Figure 18 panel (a) and (b).

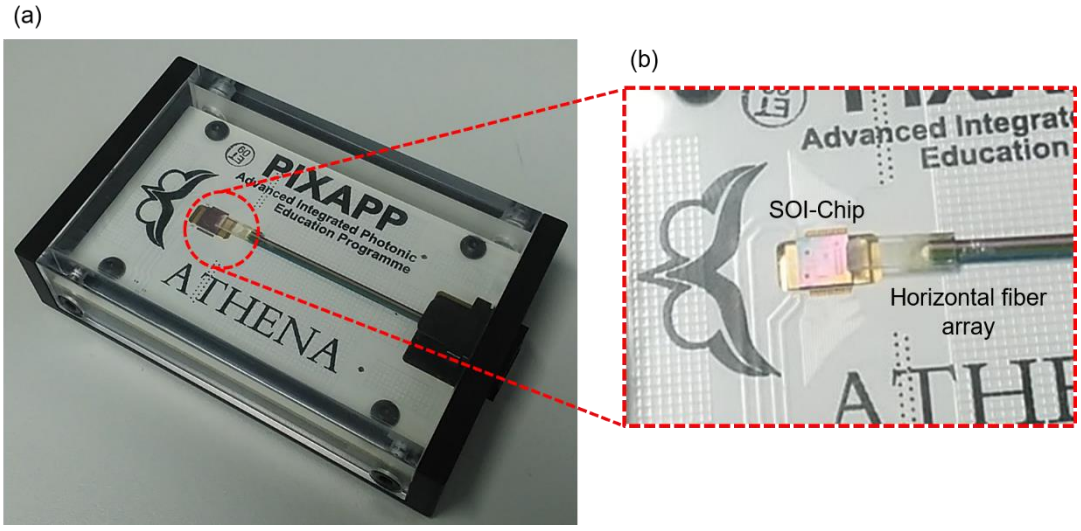

Figure 18: (a) Picture of the PIXAPP Integrated Photonics Educational Kit with the PIC and horizontal fiber array (grating coupled). (b) Closeup image of the PIC and the SOI-Chip.

2.1 General overview on grating coupling structure and theory

The most common GC structures on a SOI architecture are one dimensional (1D) GCs that show a periodicity along one spatial direction resulting in a series of repeating trenches, where the waveguide material is removed through an etching process, and teeth. Consequently, this type of structure is named uniform GC [5].

The “sandwiched” uniform GC structure with its different material layers is displayed in Figure 19.

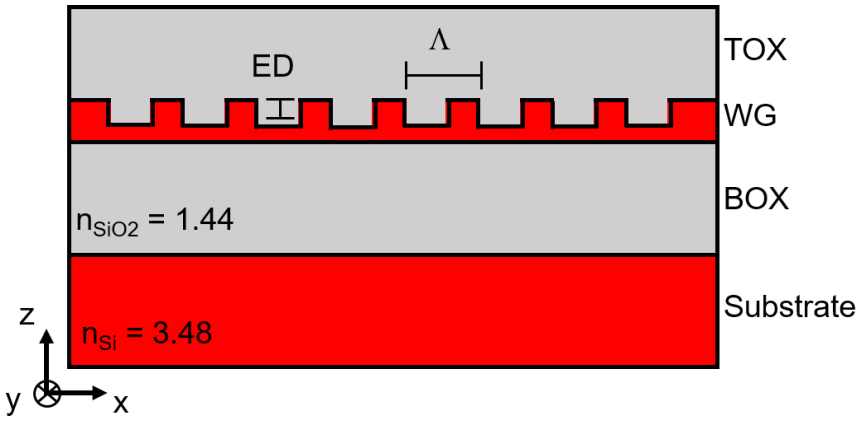

Figure 19: Uniform one-dimensional grating coupler (GC) structure: side view of the layered Silicon-on-Insulator wafer composed by the Substrate, the Bottom Oxide Layer (BOX), the Waveguide layer (WG), and the Top Oxide layer (TOX). The refractive index of Si and SiO_2 at the telecom wavelength of 1550nm is also reported as n_{Si} and n_{SiO2} [11, 12].

The WG layer sits on a 2μm-thick bottom oxide (BOX) layer made of SiO_2, which lays on a substrate layer that has a usual thickness of hundreds of microns. Typically, the WG layer is embedded inside an additional top oxide layer (TOX) made of the same BOX material.

The scope of the TOX is either mechanical offering a protection barrier for the GC from the external environment, and optical introducing a refractive index discontinuity at the TOX air interface, which can be exploitable during the coupling processes. The periodic pattern along the **x** direction, according to Figure 19, enables to introduce a periodic variation of the refractive index, between Si and SiO_2, used to build up the diffraction process to couple light into the WG. Here, each tooth of the grating acts as a discrete scatterer site as per the Huygens-Fresnel principle [13]. Consequently, the scatterer can be treated as a new point source where the sum of all contributes generates the new propagating wave, *i.e.* the m=+1 diffraction order, due to constructive interference.

As depicted in Figure 19, a uniform GC is characterized by four specific geometrical features: the WG layer thickness (T_{WG}), the etching depth (ED), the pitch (Λ), and the ratio of the tooth width to Λ, which is called duty-cycle (DC). By specifying these four quantities, the periodic geometrical GC pattern is fixed and all the parameters involved in the diffraction process are enclosed inside the x-z plane.

To establish constructive interference across the scatterer sites, the GC must be designed properly to ensure the so-called phase matching condition [14], reported in Eq. 2

2

$$k_{mx} = ksin\theta_i + m\frac{2\pi}{\Lambda} = k_x + mK$$

where k_{mx} is the wavevector of the diffracted mode travelling inside the GC, $ksin\theta_i$ is the x-component, in accordance to the spatial directions reported in Figure 19, of the wavevector of the incoming light, θ_i is the incident angle, m is the diffraction order, and K is the GC wavevector.

In order to understand better Eq 2 and the operational behaviour of a GC, the phase matching condition is derived starting from the initial situation reported in Figure 20.

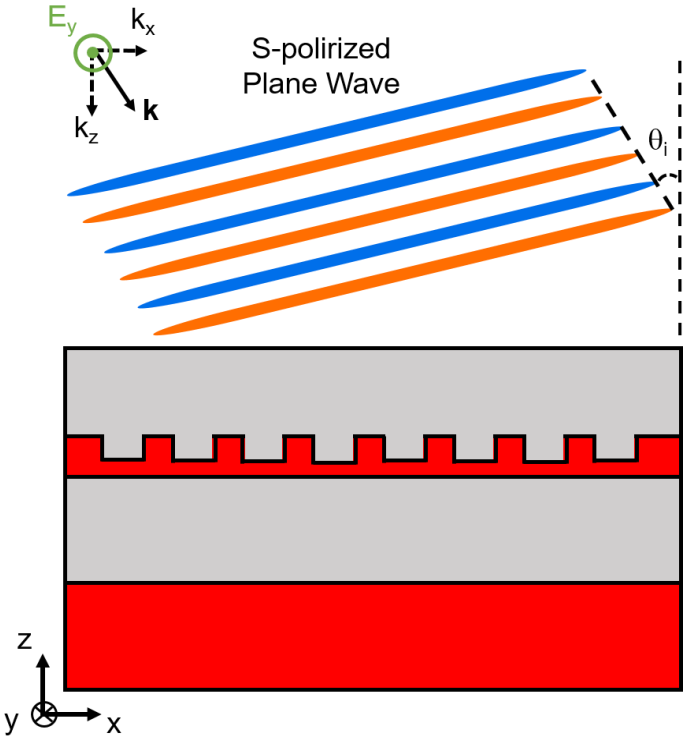

Figure 20: S-polarized incoming plane wave used to derive the phase matching condition: the blue/orange ellipses indicate the wave fronts of the plane wave, θ_i the incident angle, k_x and k_z are the Cartesian components of the wavevector **k**. The electric field oscillates along the **y** direction, *i.e.* E_y.

A S-polarized plane wave, *i.e.* the electric field (**E**) oscillates along the **y** direction, is travelling towards the GC at the incidence angle θ_i in air. When the plane wave enters inside the TOX, the angle of incidence on the GC changes accordingly to the Snell's law, $\sin\theta_i = 1.44 \cdot \sin(\theta_{i,TOX})$. At the interface between the TOX and the GC, the continuity of the E_y is guaranteed by the polarization state, in accordance with the boundary condition of the Maxwell's equations, leading to the following Eq 3, which links the incident (E_y^i) and reflected (E_y^r) waves with the transmitted (E_y^t) one

3

$$\mathrm{E_y^i} e^{-ik(x*\sin\theta_i - \mathrm{f(x)}*\cos\theta_i)} + \mathrm{E_y^r} e^{-ik(x*\sin\theta_i + \mathrm{f(x)}*\cos\theta_i)} = \mathrm{E_y^t} e^{-i(k_x x + k_z \mathrm{z})}$$

where the function f(x) takes into account the varying height profile of the GC. The latter shows a periodic pattern with a pitch equal to Λ, thus it is straightforward to see that this is the periodicity of the GC height profile. Consequently, it follows that f(x) is periodic with period Λ, and the function $e^{-ik\mathrm{f(x)}\cos\theta_i}$ can be expanded in Fourier series, making explicit its fundamental harmonics components [15, 16], as

4

$$e^{-ik\mathrm{f(x)}\cos\theta_i} = \sum_{-\infty}^{+\infty} A_m e^{-im\frac{2\pi}{\Lambda}x}$$

Now, substituting Eq. 4 into Eq. 3, we obtain

5

$$\mathrm{E_y^i} e^{-ik(x*\sin\theta_i)} \sum_{-\infty}^{+\infty} A_m e^{-im\frac{2\pi}{\Lambda}x} + \mathrm{E_y^r} e^{-ik(x*\sin\theta_i)} \sum_{-\infty}^{+\infty} A_n e^{-in\frac{2\pi}{\Lambda}x} = \mathrm{E_y^{tm}} e^{-i(k_x x + k_z \mathrm{z})}$$

To enabling the coupling of the incoming plane wave, the conservation of the momentum must hold leading to Eq. 6

6

$$k\sin\theta_i + m\frac{2\pi}{\Lambda} = k\sin\theta_i + n\frac{2\pi}{\Lambda} = k_{mx}$$

Eq. 6 is the phase matching condition where *m* (or *n*) is an integer number (*m*=0, ±1, ±2...), which expresses the diffraction order of the grating coupler. Thus, the light transmitted through the GC is a sum of travelling plane waves, *i.e.* diffraction orders at different angles.

Now, not all the diffraction order as a physical sense, and this can be understood through a graphical representation of the phase matching condition where the GC is ideally positioned at the centre of two concentric semicircles, with diameters equal to the magnitude of the wavevectors inside the materials that surround the GC.

The wavevector of the *m*th diffraction order is constructed by subtracting *m*-times the *K* wavevector to k_{mx} and drawing vertical lines from the end point of the resulting wavevector. Thus, the diffraction order has a physical sense if and only if this vertical

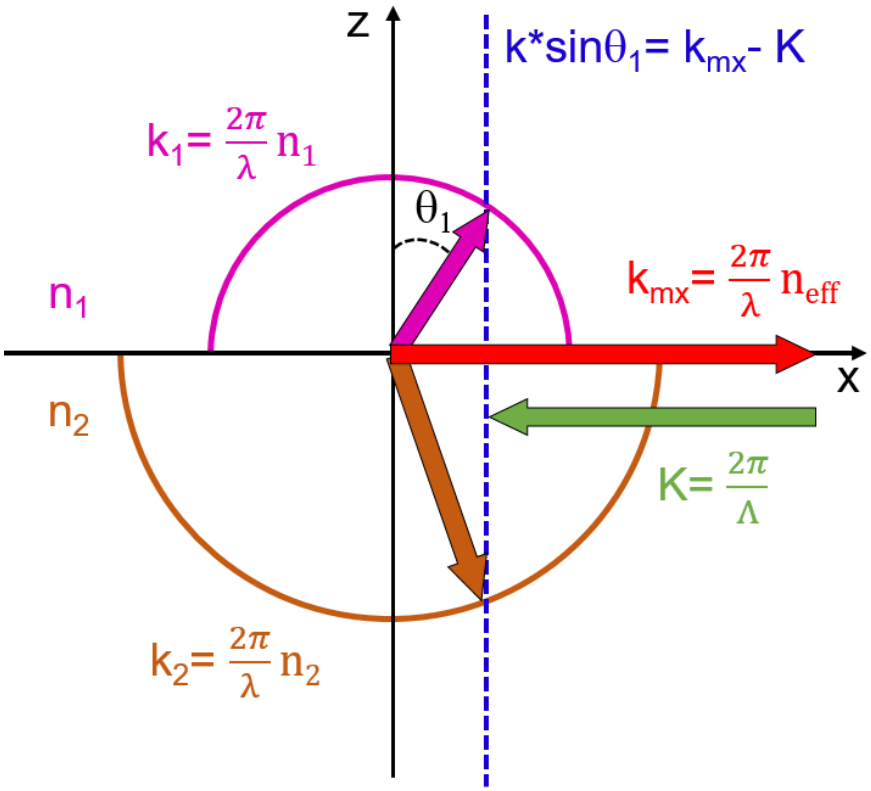

Figure 21: Graphical representation of the phase matching condition in the so-called detuned configuration.

line crosses the semicircles. In the so-called detuned configuration [7], $k_{mx}>K$ and the m=+1 diffraction order is permitted at a certain angle θ_1, as shown in Figure 21, ensuring no reflection inside the waveguide of the m=+2 diffraction mode, and the consequent suppression of higher order modes, reducing the additional losses during the coupling process.

For the sake of completeness, another configuration called resonant can be used. Here, k_{mx} matches K and it can be shown, following an equal graphical representation of the phase matching condition, that the m=+2 diffraction order is reflected back into waveguide [17, 18, 19]. Intuitively, this configuration is disadvantageous if the GC is thought as an optical connector to in- or out-couple light into a preferential channel, as the energy is split half into the first and half into the second diffraction orders [20].

Considering a detuned configuration and with the final aim of coupling the first order of diffraction, Eq. 6 can be recast in a more convenient form known as Bragg equation with little algebraic work; the latter can be directly used to design the GC to couple light at a specific tuning wavelength (λ_t)

7

$$\lambda_t = \Lambda * (n_{eff} - n_{TOX} \sin\theta_i)$$

where n_{eff} is the effective refractive index of the guided mode, and n_{TOX} the refractive index of the TOX material, and *m* is equal to +1. The Bragg equation links directly the incident angle and λ_t to the structural parameters of the GC, explicitly through the period and implicitly via the n_{eff}, which depends on T_{WG}, ED, Λ, and DC. The Bragg equation holds for infinite structures; however, real GCs have a finite number of periods and Eq. 7 can be satisfied at a fixed θ_i by multiple wavevectors around the one derived from the Bragg equation with a consequent coupling of different wavelengths. Consequently, the GC spectral response is not a delta function centred at λ_t, but it has a certain distribution with its own spreading [21].

The ideal S-polarized plane wave striking the GC in the detuned configuration is achieved in practice interfacing a SMF, tilted at a small angle θ_i= 8°, 10°, [22, 23], avoiding second order diffraction, and guaranteeing an almost vertical configuration, as shown from the sketch in Figure 22 panel (a).

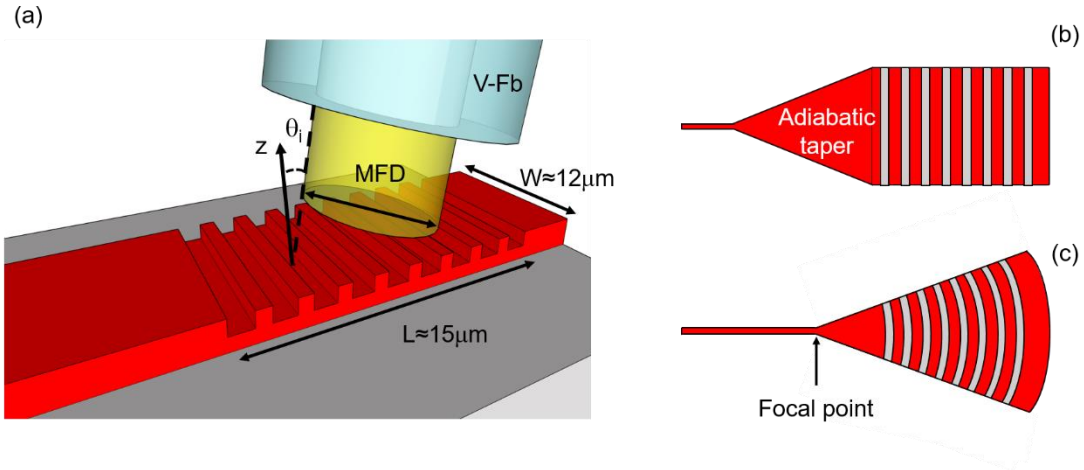

Figure 22: Uniform 1D GC: (a) Vertical coupling geometry with a Single Mode Fiber vertically interfaced (VFb) to the PIC with its Mode Field Diameter (MFD), and angle of incidence θ_i. The typical geometrical dimension length (L) and width (W) of a uniform GC is also reported. (b) Top-view of a uniform GC with the adiabatic taper used to squeeze the coupled mode and inject it efficiently into the waveguide. (c) Top-view of a focusing uniform GC with the curved teeth used to focus the light at the entrance of the PIC waveguide (Focal point).

The SMF emission can be directly coupled by the GC ensuring the flatness of the wavefronts, as in the ideal case, avoiding light striking the GC at different angles. Because the SMF has a Gaussian emission profile with a MFD of 10.4μm at 1550nm

[24], the footprint of a standard GC is represented by a rectangular area of 15x12 μm^2 in order to accommodate the MFD, as shown in Figure 22 panel (a) [25].

These dimensions make impossible to directly couple the diffracted light into a single mode WG of the SOI architecture, due to its tinier geometrical dimension (220nm height and 450nm width). Thus, an adiabatic taper is necessary to collect the diffracted light and gently squeeze it in progressive smaller spatial region, see Figure 22 panel (b) [26, 27].

However, an adiabatic taper displays lengths of the order of hundreds of micrometres to adapt the optical impedance [28], *i.e.* the n_{eff} of the propagating mode, between the GC region to the entrance of the WG reducing, consequently, the back-reflection almost to zero.

A more compact and technological appealing solution is represented by the so-called focusing GC [29], see Figure 22 panel (c). The footprint of the GC is reduced thanks to the concentric curved teeth of the GC, which act as lenses with the same focal point placed at the entranced of the WG; this allows to eliminate the use of an adiabatic taper reducing consistently the GC dimension. Moreover, all the parameters that affect the diffraction process, in accordance with the Bragg law, lie in the x-z plane in accordance with Figure 20. Consequently, an almost equal operational behaviour is expected from the two GC layouts.

It is usually convenient to design and optimize the GC geometrical parameters (ED, Λ, and DC) for configuration with straight teeth and then bending them according to the law

8

$$g\lambda_t = n_{eff}\sqrt{x^2 + y^2} - x * n_{TOX}\cos\theta_i$$

where g refers to the tooth number, n_{eff} is the effective refractive index of the spherical propagating wave, as reported in [29].

The polarization state of a SMF is not uniquely defined due to cylindrical symmetry and the phase matching condition is guaranteed only for a S-polarized wave. This implies that the fundamental mode travelling inside the SMF must be TE, with respect to the x-z plane defined previously, with **E** oscillating parallel to the teeth. This condition is achieved using an external manual polarization controller to change the polarization state. For practical purposes, Polarization Maintaining (PM) fibers are the

easiest solution to pursue, as they keep fixed the polarization state of the light, which can be properly selected before entering into the fibre [30].

However, the cost per meter of PM fibers is one order of magnitude higher with respect to normal SMFs [7]; therefore, two dimensional (2D) GCs have also been proposed to overcome this issue being able to accommodate either the TE and TM polarization states [31, 32, 33, 34, 35, 36, 37]. However, the performance of such structures are not comparable with the one of a 1D GC and implies more complex fabrication steps.

Now that the physics behind the coupling process of a GC has been introduced together with the electromagnetic features of the light impinging on the GC, it is fundamental to define a parameter that quantifies the efficiency of the diffraction process built by the GC: the Coupling Efficiency (CE). The latter defines the percentage of power per wavelength injected inside the WG by the first order of diffraction and it is defined as follow

9

$$CE(\%) = \frac{P_{in}(\lambda)}{P_0(\lambda)}$$

were P_{in} and P_0 are the power coupled into the WG and the initial power emitted by the fiber, respectively, at λ.

From the CE curve, two main parameters are used to calculate the performances of a GC: the CE evaluated at the working wavelength λ_t, and the bandwidth (BW) that is the spectral interval associated to an arbitrary drop of the CE curve from its peak. The BW measures the number of wavelengths coupled efficiently by the GC, and it is not defined uniquely in literature.

Usually, for engineering purposes, the BW is associated with a 1dB or 3dB drop from the CE peak, considering wavelengths efficiently-coupled the one that shows an efficiency difference from CE(λ_t) of roughly 20% and 50% respectively.

Figure 23 panel (a) shows an example of CE curve calculated for a uniform GC with a ED=82nm, Λ=645nm, and DC=0.58 designed for a θ_i=10° inside the TOX layer and illuminated with a Gaussian beam with a MFD equal to 10.4μm. The result has been evaluated using the Finite Difference Time Domain Method (FDTD) which is an

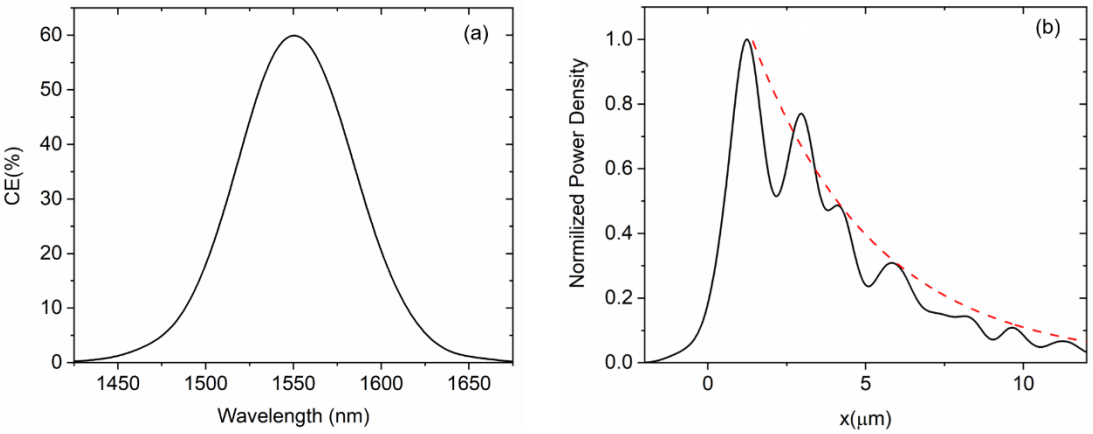

Figure 23: (a) Example of a Coupling Efficiency (CE) curve of a uniform GC calculated using a two dimensional Finite Different Time Domain (2D-FDTD) Simulation where a Gaussian beam with a MFD=10.4μm is used as light source. (b) Emission power density profile of a uniform GC calculated using a 2D-FDTD simulation. The red dashed line refers to an exponential fit of the power profile. The structural parameters of the uniform GC are: DC=0.58, ED=82nm, Λ=645nm.

algorithm that resolves Maxwell's equations in space and time. In particular, the commercial software Lumerial® FDTD Simulations™ is used to perform the FDTD simulations [38]. Further details on the algorithm structure and how it works are reported in Appendix A.

The reported uniform GC displays a CE(λ_t)=60% and a 1dB BW=40nm. In particular, the CE(λ_t) depends on two fundamental parameters in grating coupling: the directionality (D) and the reflectivity (RF), which are respectively the ratio of the power diffracted upward by the GC to the amount of power travelling inside the WG before the GC (P_{WG}), and the ratio of the power back reflected inside the WG to P_{WG} [7].

Before going into more details regarding these two quantities, it is important to understand that, as long as the WG and the SMF are single mode the reciprocity theorem holds [39]. This implies that the in-coupling and out-coupling processes, from the SMF to the WG and from the WG to the SMF, via the GC are equal.

Therefore, it is intuitive to understand that the higher the D and the lower the RF, the grater the ability in coupling the first diffraction order resulting in a higher CE(λ_t). D and RF strongly depend on to the structural parameters of the GC. This relationship can be expressed for D through the so-called scattering strength (α), which quantify the "scattering force" of each tooth, and for RF from the optical impedance matching between the WG and the GC region. For a uniform GC, α depends either on the ED

and the DC, and it can be evaluated from the emission density power profile, which follows an exponential decay law

10

$$P(x) = P_0 e^{-2\alpha x}$$

where P_0 is the maximum value of the out-coupled power density [40]. Figure 23 panel (b) shows the actual normalized exponential decay calculated using the FDTD for the aforementioned uniform GC, and fitting the envelope with an exponential decay law, a value of α equal to $0.257\mu m^{-1}$ is calculated.

From Eq. 10, it is clear that the majority of the power is scattered by the first two/three teeth of the GC, meaning that there is a dependence on the x position of the SMF with respect to the GC. Intuitively and bearing in mind the reciprocity theorem, the centre of the Gaussian beam has to shine on the first periods of the GC to maximize the CE.

From an easy geometrical consideration, it is clear that a significant fraction of the power is physically outside the Grating Coupler. This issue is usually addressed in literature as the overlap problem between the Gaussian emission SMF profile and the exponential profile derived by Eq. 10. Low D and poor mode overlap offered by uniform GC limit the CE(λ_t) at value < 60% [7].

In order to boost the GC CE, different techniques have been developed so far. CE higher than 90% have been reported for uniform GC on a 220nm-thick SOI exploiting a metal mirror or a distributed Bragg reflector (DBR) at the substrate-BOX interface in order to recouple the light, which is usually transmitted through the GC and lost inside the substrate [41, 42, 43].

On the other hand, the use of overlay layer on top of the GC teeth can be used to increase the WG layer thickness of the GC increasing the scattering strength and, hence, the D of the structure [44] with CE up to 70% [25].

However, in both cases, the pure SOI wafer structure has to be customized resulting in non-standard fabrication processes leading to higher final costs and fabrication time.

To overcome such issues, one of the most interesting and exploited approach consists in the apodization of the GC. In this case, the structure does not display a constant DC and Λ, which vary along the $\boldsymbol{x}$ direction for each period, resulting in a non-uniform GC [22]; an example of such structure is reported in Figure 24.

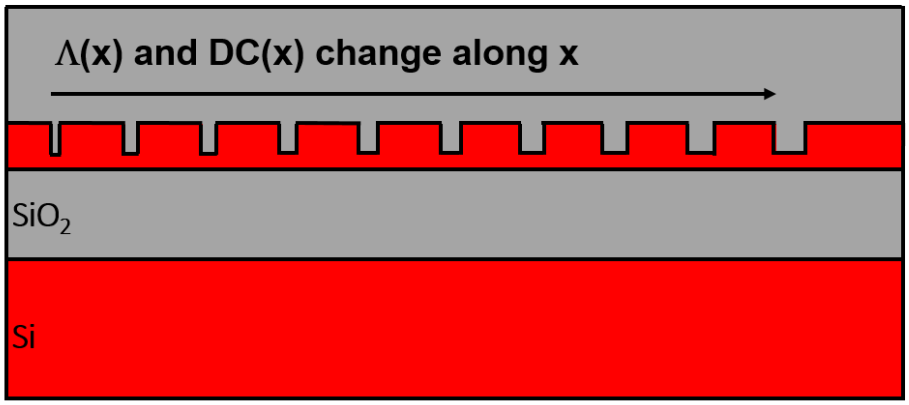

Figure 24: Non-Uniform GC structure where the pitch (Λ) and the duty-cycle (DC) change along the **x** direction.

Thanks to the fine tuning of the DC at each period, the apodization allows to obtain two fundamental advantages to boost the CE: (i) the scattering strength is no longer constant, but is a function of the apodization direction x enabling to reshape and get a Gaussian power density emission profile compatible with the SMF's mode; (ii) the mismatch in the optical impedance between the effective refractive indexes of the WG mode and the GC region can be controlled and tailored to reduce the RF.

In literature, many design techniques are reported for non-uniform GC either by systematically tuning the emission profile of the GC to match a certain field distribution through the variation of α at each period of the GC [5, 45, 46], or using numerical evolutionary algorithm to optimize the structural parameters of the GC showing theoretically CE up to 89% for a 340nm-thick SOI [47].

Moreover, there are examples of apodized GC were either the DC and the ED are varied along ***x*** [48], and even more complicated apodized structures with a 2D pattern, known as subwelength GC, have been proposed [49].

In this framework, linearly apodized GC, where the DC is changed linearly across the apodization direction, have been demonstrated to be one of the highest performer with low discrepancies between the theoretical and experimental results [50]. In particular, a 260nm-thick SOI non-uniform GC with a varying DC and pitch has been demonstrated to show one of the highest CE ever measured with a VFb coupling scheme [51]. Here, a measured CE=81% has been shown with low discrepancy respect to the theoretical predictions.

Besides the previous examples, a "hybrid" approach can be also considered resorting to the application of a specific apodization technique, for instance exploiting the linear variation of the DC, and the use of evolutionary algorithms to carefully tuned

the apodization law and all the other structural parameters of the non-uniform GC. This approach is the one considered in this thesis, and the next paragraph is focused on the explanation of the design routine applied for optimizing GCs for Photonics Packaging purposes.

2.2 Particle Swarm Algorithm for Grating-Coupler Optimization: overview

Electromagnetisms has seen an extensive use of algorithms throughout the past decades for the optimization of the geometrical shape and structural parameters of physical objects, such as antennas [52], where either a non-trivial analytic solution specific to that problem exists or simply the possibility of resolving all the possible geometrical configurations is not feasible. In this frameworks, GCs are not an exception since their operational behaviour is based on a quite complex diffraction process, which necessity of computational methods, as the FDTD, to fully resolve the electromagnetic problem in space and time; moreover, it depends on all the structural features of the GC resulting in being a multi parameter problems.

As a consequence, the idea of numerically testing all the possible various combinations with the final aim of selecting the one with the highest CE can result in a real “computational nightmare” in terms of computational time needed.

Thus, the use of evolutionary methods has been proven to be an effective approach in reducing the time needed during the design process. In particular, the Genetic Algorithm and Particle Swarm Optimization Algorithm (PSO), both heuristic population-based search methods [52], represent one of the most popular evolutionary approach to design GCs.

Genetic algorithms base their working philosophy on the concept of natural selection and adaptation, as life in nature. The algorithm structure is not easy and straightforward to implement as its functioning is based on three different operators known in literature as: selection, cross-over, and mutation to evolve the structural parameters, proper of an ensemble of GCs, from one generation to the next one seeking for the best performer.

PSO was historically invented during the 90s, inspired by the flocking behaviour of swarms of animals, such as birds [53]. In this case, an initial randomly-generated population (swarm), composed by a certain amount of particles also called agents,

undergoes an iterative optimization process moving across the parameter space searching for the best global solution, *i.e.* the GC with the highest CE in our case. The travelling of the swarm at each step is highly influenced by the information shared between the different particles as a social collaborative behaviour is established between the agents.

Generally, the PSO presents various advantages respect to the genetic algorithms: the algorithm has a simpler mathematical structure based on one unique operator, the velocity v_i of the different agents, resulting in being easy to implement inside external computational method.

Various studies have been done comparing the performances of genetic algorithms and PSO with the usual outcome that both the approaches show quite the same optimization capabilities in terms of time needed to complete the optimization process and final results, *i.e.* quality of the optimization process [54].

Due to its easier code and faster implementation and, consequently, debugging, the PSO has been chosen as optimization routine for the GC designs proposed in this work. In this section, the mathematical structure of the PSO algorithm is presented giving an overview and showing the potentialities on its application to the specific problem of GC design.

The computational validation of the design process is also proposed by applying it to the design of GC structures well-known in literature and comparing the final outcomes of the PSO in terms of structural parameters and performances with the corresponding results found in literature.

The work showed inside this section was presented at the: "41st *PhotonIcs & Electromagnetics Research Symposium*" conference in Rome and the related results are reported in the published proceeding [55].

To perform the optimization procedure an Alienware Area 51 (Dell) with liquid-cooled Intel® Core™ processor i9 (16 core) and 64GB of RAM was used.

2.2.1 Particle Swarm Algorithm for Grating Coupler Optimization: mathematical structure and validation

The PSO evolutionary structure is sketched out in Figure 25.

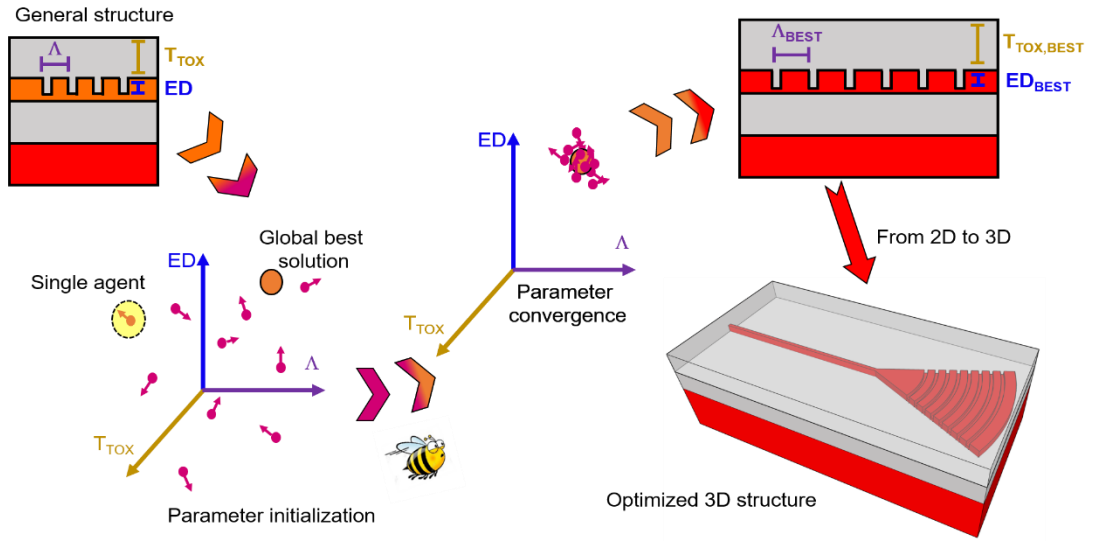

Figure 25: Particle Swarm Optimization Algorithm (PSO) evolutionary structure. The Figure has been taken from [55].

The first step is the definition of the parameters to optimize in order to boost the CE. Here, the TOX height, the etching depth (ED), and the period Λ are chosen as an example to explain the PSO operation. Then, appropriate limits to the parameter space can be imposed in order to limit the searching process inside a specific region. The latter can be selected in accordance with the fabrication constrains of the lithographic procedure intended to exploit to fabricate the optimize structure. For instance, it is possible to respect the limits in terms of resolutions of the geometrical features imposed by foundries during their MPW runs.

At this, point, the PSO randomly selects triads (T_{TOX}, ED, Λ) of parameters, which represent the coordinates that fix the initial positions of the agents inside the parameters space. The number of agents can be chosen depending on the specific problems. Usually, ten agents are sufficient to guarantee the algorithm convergence and an efficient scanning of parameters space.

The triads are then passed to Lumerical in order to build the corresponding 2D-FDTD general structures and to resolve the electromagnetic problem obtaining the corresponding CEs, which are saved by the PSO. The position of the agent with the highest value of CE is recorded as the global best position, g_{best}, inside the parameters

space and all the other triads of agents define the initial local best positions, $p_{i,best}$, where i specify the agent.

Now, the real iterative process takes places and a velocity (v_i) that governs the temporal evolution of each agent's position is created and varied throughout the iterative process in accordance with the following equation

11

$$v_i = w * v_i + c_1 * \text{rand} * (g_{best} - x_i) + c_2 * \text{rand} * (p_{i,best} - x_i)$$

where w is the "inertial weight" that is decreased progressively across the iterations from 0.9 to 0.4, c_1 and c_2 are two separate constants that regulate the "pulling" towards the g_{best} and $p_{i,best}$ positions of the agents governing the acceleration process towards the two positions set both equal to 1.49, rand is a function that returns a random number between 0 and 1, and x_i points out the position of the i-th agent. The position is progressively changed according to the equation

12

$$x_i = x_i + v_i * \Delta t$$

where Δt is usually sets equal to 1.

This is the mathematical structure of the algorithm and, as it can be seen, it is quite simple and intuitive. For further details on the selection of the different constants in Eq. 11, the work of J. Robinson and Y. Rahamat-Samii can be consulted [52].

Then, the PSO compares the CEs at the new positions x_i with the g_{best} and $p_{i,best}$, which are updated if and only if a position x_i has returned higher values of CE; otherwise the local position is simply discarded.

Thus, the optimization process is not memory consuming either. Sometimes it can happen that during the selection of the v_i an agent reaches the boundary along one of the three directions imposed on the parameter space. The results are a triad of structural parameters that are not allowed by our initial conditions. An easy solution to this problem is represented by "reflecting walls" at the boundaries: the sign of the velocity of the agent along that direction is inverted to reflect it back into the limits of the parameters space.

In this way, the PSO explores the whole parameters space calculating the CEs for the corresponding FDTD structures at each iteration till the reaching of the parameter convergence characterized by a global best triad: Λ_{BEST}, ED_{BEST} and $T_{TOX,BEST}$. These three parameters are given by the PSO to Lumerical to generate the corresponding

optimized 2D-FDTD optimized structure, which shows the overall highest CE between all the possible structures that can be built resorting to the values inside the parameter space. For further information on how the PSO is implemented inside Lumerical, how it is structured and the time needed to develop it look at Appendix B.

At this point, a new code is exploited to create the 3D optimized structure inside a different FDTD simulation to study the whole physics behind the scattering process and to test the focusing effect due to the curved teeth of the 3D GC. Besides the evaluation of the CE of the optimized structure, the FDTD is also exploited to evaluate the main channel of losses of the structure, *i.e.* the light back-reflected from the GC and the light transmitted through the WG layer and lost inside the substrate. Figure 26 shows the main FDTD power monitors used to check the 3D optimized structure.

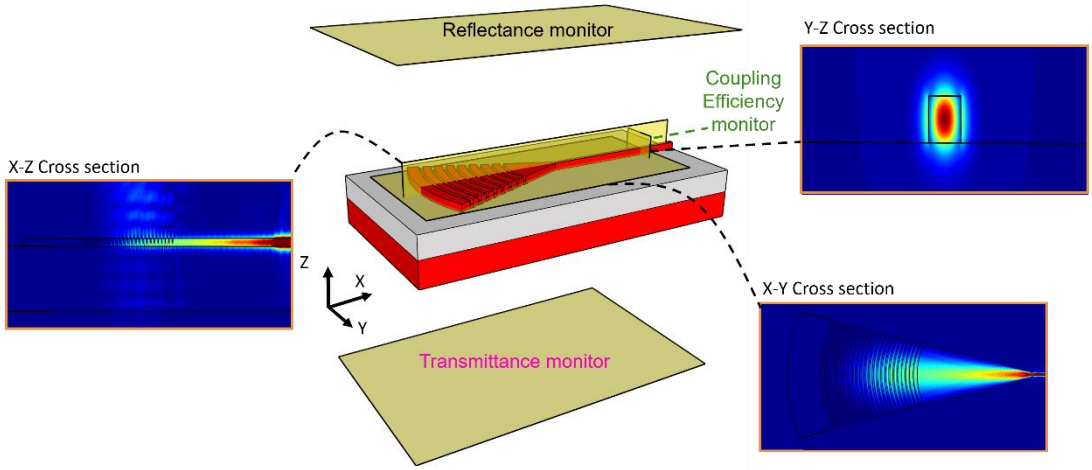

Figure 26: Sketch of the monitors used to study the performances of the GC. The Coupling Efficiency (CE) monitor is used to evaluate the CE curve; while, the reflectance and transmittance monitors are exploited to calculate the losses. In addition, the electric field expansion at the wavelength λ_t=1550nm is analysed thanks to the following monitors: the X-Z cross section gives an overview of the scattering phenomenon, the Y-Z cross section shows the details about the electric field actually injected into the waveguide, and the X-Y cross section displays the electric field injection towards the waveguide. The Figure has been taken from [55].

As depicted in this image, the reflectance and transmittance monitors are exploited to evaluate the energy lost. The X-Z Cross section is used to monitor the diffraction process of the GC and rebuild its pattern: the majority of the electromagnetic field is diffracted towards the WG, another fraction is back-reflected by the structure, and a third one is lost inside the substrate. The X-Y cross section shows the focusing effect and consequently the injection of the light towards the WG; finally, the Y-Z cross section of the GC displays the details regarding the electric field injected into the WG. Furthermore, the Y-Z monitor is also used to evaluate the CE of the GC.

Eventually, the GDSII™ file [56] related to this structure can be extracted and used directly for the lithographic fabrication process.

Two "gold" structures have been rebuilt using this design process. The GCs under investigation are defined on a pure SOI wafer, no use of back reflectors at the substrate-BOX interface, and they are respectively a uniform GC defined on 220nm-thick WG layer with a Si overlay layer used to increase the height of the teeth [25], and a linear chirped, *i.e.* non-uniform, GC defined on a 260nm-thick SOI, [51].

Figure 27, panel (a) and (b), shows the CE, transmittance (T), and the reflectance (R) spectra for both the PSO optimized structures.

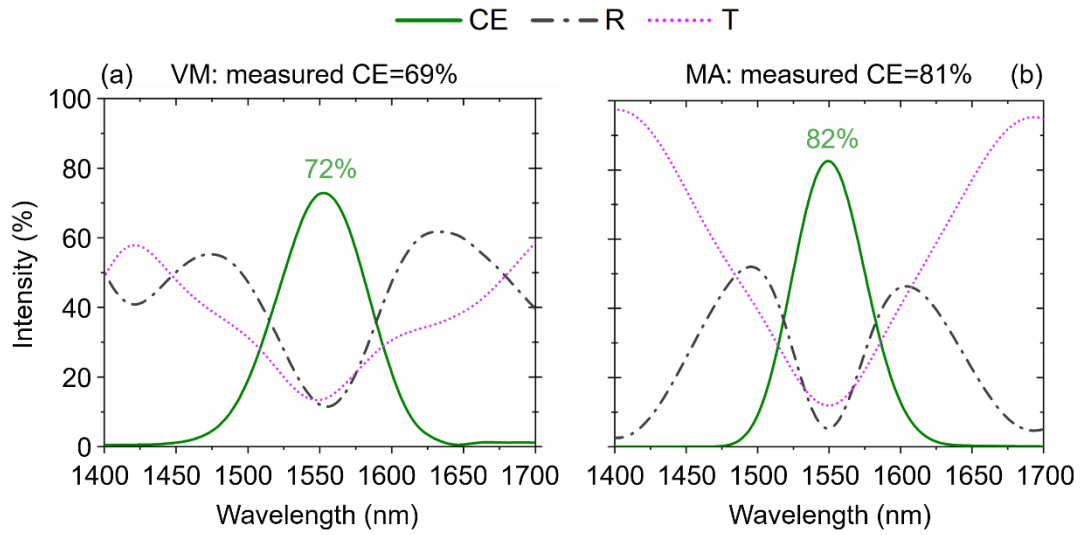

Figure 27: Design-routine validation through the comparison with two known "gold" structures: (a) Uniform GC with a Si overlay, Vermeulen *et al* [25], called VM (b) Non-uniform GC, Marchetti *et al.* [51], called MA. CE (solid green line), R (dash-dot dark grey line) and T (short-dot magenta line) are the simulated Coupling Efficiency, Reflectance, and Transmittance proper of the two GCs enabling a direct comparison between their spectral behaviours. The Figure has been taken from [55].

The light source used for the optimization is a Gaussian source with a 10.4 MFD in a vertical coupling scheme in accordance with the coupling procedure reported in the corresponding literature. The GC parameters in both cases are closed to the geometrical parameters proper of the fabricated structures (*i.e.* below the fabrication tolerances). The corresponding theoretical CEs at 1550nm, our λ_t, show a discrepancy of 3% and 1% compared to the measured values respectively for the uniform and the non-uniform designs. The higher CE found by our PSO can be addressed to a higher value of the overlay found by the PSO respect to the one reported in the article resulting in a better scattering strength. The two panels enable a further comparison between the two designs, which is useful to understand the major physical differences

between these two designs. First, a 10% difference in the CE value at λ_t can be seen and, thus, the non-uniform design results to be more efficient. The reason can be understood looking at the losses. The reflectance and transmittance behaviours are almost the same for both structures in the spectral interval of (1475÷1625) nm for the uniform GC and (1500÷1600) nm for the non-uniform. Outside these spectral regions, the trends show a consistent difference: while the uniform GC maintains values of reflectance and transmittance around 40% and 60%, the non-uniform design shows a sharp decreasing of the reflectance, below 10%, and a fast increasing of transmittance with values higher than 90%.

The non-uniform GC displays a more selective behaviour of the wavelengths around λ_t: the further away from the tuning wavelength we move, the higher the transmittance suggesting that whole the light at these frequencies is transmitted through the GC without interacting with it. On the other hand, this does not happen for the uniform GC where a less selective selection by the structure results in a broadened CE curve. Furthermore, the minima of the reflectance and transmittance curves are precisely fixed at λ_t for the non-uniform GC, while a slight detuning either in the reflectance and in the transmittance is displayed by the uniform design.

In particular, it is easy to see that the 10% higher CE is gained by the non-uniform GC simply reducing the reflectance almost to zero, while the transmittance value remains comparable to the uniform design suggesting that the overall scattering strength of the two structures is almost the same.

For the sake of completeness, the PSO has been applied to compare its outcome with the one obtained from a third study where a genetic algorithm was exploited to optimize a non-uniform GC with a stochastic disposition of the teeth of a GC built on a pure 220nm-thick SOI [47]. The reported CE is 65% at λ_t while the PSO found a best structure with a CE=70%. The 5% discrepancy can be neglected taking into account the fluctuations in the convergence of the algorithms and the different nature of the optimization procedures.

Thus, the design process turns out to be an affordable instrument to seek after a complete optimization model for GC structures and, as already proven, also accurate and reliable.

The power of the proposed design-process is represented by the possibility of optimizing a GC for a different coupling geometry.

GCs are usually optimized for a vertical fibre (VFb) coupling geometry, which is quite fragile and bulky for certain packaging applications. Thus, other alternatives have been developed based on either a horizontal fibre (HFb) [57], where the SMF facet is polished at a required angle in order to inject the light at the right incident angle taking advantage of the total internal reflection; and a third geometry based on a hybrid on-PIC integrated laser source, which exploits a micro optical bench (MOB) to deliver light to the PIC particularly interesting for sensing applications [58]. For further details, see Chapter 5.

Moreover, either the HFb and the MOB have an advantageous form-factor with respect to the VFb, which results in a reduce vertical dimension of the final package due to their planarity. Thus, they allow to obtain an almost 2D structure [59].

However, their electromagnetic modes present features different from the VFb emission resulting in additional extra losses [60] if a GC optimized for a VFb is used for a different coupling scheme. In fact, the HFb mode undergoes an unconfined travelling inside the fibre cladding of about 60μm resulting in a wider MFD at the GC surface.

However, while the MOB can be customized and designed to mimic the VFb emission tuning precisely the distances between the lasers and the μOptics, as it is explained in Chapter 5, a customization of a standard SMF can have dramatic downsides in terms of packaging costs. In this case, the best available option, for keeping low costs, is the optimization of a GC to maximize the overlap between the HFb mode and the GC acceptance profile. This can be done exploiting the FDTD method to rebuilt the HFb structure and simulates its emission. The latter can be used as a new light source inside the PSO process to optimize the GC.

The electromagnetic mode of the SMF has a Gaussian shape and the spatial spreading depends on the initial MFD=$2w_0$, where w_0 is the mode field radius (MFR). Exploiting its circular symmetry, a 2D-FDTD simulation is sufficient to describe the spreading of the mode across the cladding reducing consistently the computational time. This is essential since the usual FDTD simulation region has a cross-section relatively large to simulate (100 x 100)μm rather than the vertical geometry where a cross-section of roughly (10 x 10)μm is needed.

The complexity behind the design of this coupling scheme is one of the main challenge that prevented the optimization of GCs for the HFb, and this represents a

chance for novel research. In fact, a complete characterization of new GC designs explicitly designed for this coupling scheme constitute a valuable contribution for Integrated Photonics.

The uniform design reported in [25] has been tested exploiting 2D-FDTD simulations under a HFb, where the HFb position has been optimized running a sweep to find the best alignment along **x**, and a decreasing of roughly 10% in the CE has been calculated with a CE=60% at 1550nm. This shows that an arbitrary GC design optimized for the VFb cannot be directly used with the HFb without introducing extra losses.

Thus, two separate PSO processes were run using both the emission of the VFb and HFb, as a light source, allowing the algorithm to search for an optimized GC, but this time with a thicker overlay layer with respect to the design of Vemeulen *et al.* in order to increase further the scattering strength. Eventually, both structures have been tested under the HFb to look at the performances and the results are reported in Figure 28.

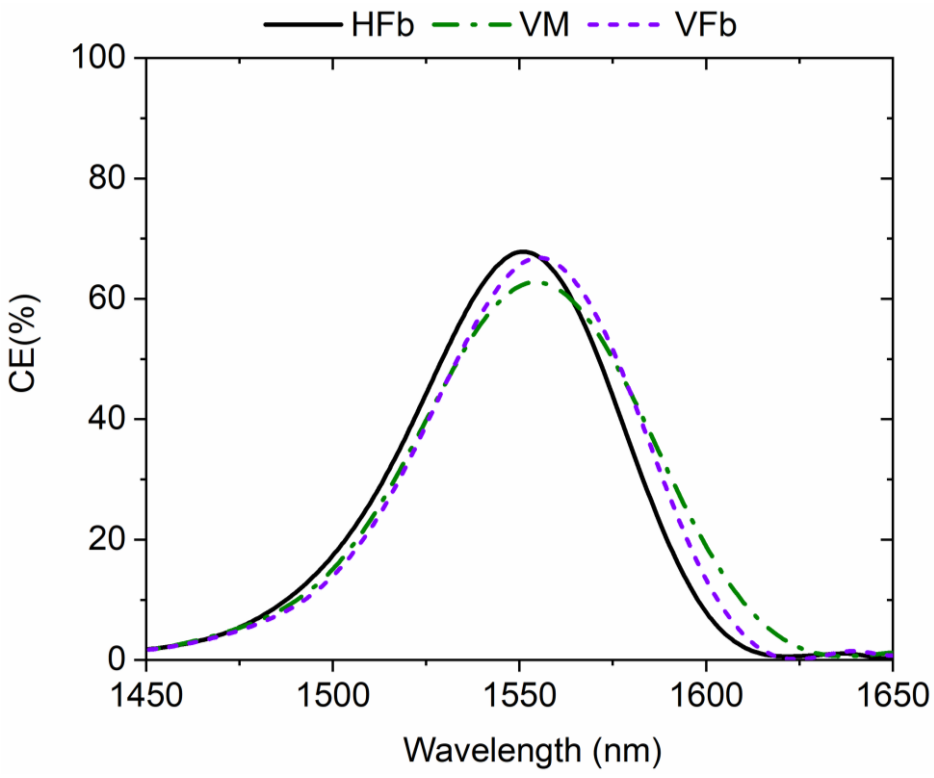

Figure 28: CE curves calculated using 2D-FDTD under the Horizontal Fibre (HFb) coupling scheme for a 220nm-thick SOI uniform GC with an additional overlay layer. In details: HFb refers to the GC optimized for the HFb using the PSO algorithm, the VM GC refers to the design reconstructed using the structural parameters reported in Vermeulen e*t al.* [25], and the VFb is the GC design optimized for the Vertical Fiber coupling scheme (VFb) and tested under the HFb.

The GC structure optimized for the HFb reports the highest CE value, 68%, at 1550nm recovery almost completely the decreasing shown by the GC design of Vermeulen *et al*. Moreover, the other interesting result is displayed by the VFb GC: this structure has the highest overlay layer above all, with a thickness of roughly 210nm, and a deeper etching depth compared to the HFb, suggesting that the further increment in the scattering strength can compensate for the MFD mismatch. As demonstrated, the additional Si overlay is useful to reduce the losses of a uniform GC obtaining also the chance of having a unique design for either the HFb and the VFb. However, even though the deposition of an extra layer is a CMOS compatible technique, it is not considered a standard procedure and requires a modification of the native SOI wafer structure. In this framework, as we saw, the best performers for pure SOI wafer are non-uniform GC.

Encouraged by the previous results, we decided to optimize systematically a series of non-uniform GCs for different SOI thicknesses, spanning between the two standard 220nm-thick and 340nm-thick SOI platforms, in order to boost the CEs at maximum and considering, simultaneously, the effect of the overlay layer by using progressively thicker SOIs.

The next Chapter is focused on the design, fabrication, and experimental characterization of these non-uniform GC designs optimized for the HFb coupling scheme. The following results were published in the *Journal of Lightwave Technology* [61].

2.3 Conclusions

In this Chapter, a detailed introduction to the GC theory is reported with a derivation of the Bragg law as well as the definition of the main parameters involved in grating coupling, *e.g* the CE, the BW, the scattering strength α, *etc.*

An overview of the literature related to the best performers is provided introducing important GC layouts such as uniform-GC with overlay and, more importantly, non-uniform GCs.

The attention is then focused on the design routine developed in this thesis used for the optimization of GCs. Thus, the structure of the PSO algorithm, backbone of the design routine, is pointed out in details showing how the PSO optimizes through

an evolutionary process the structural parameters of a generic GC structure seeking for the highest CE at the desired tuning wavelength.

The design routine is validated optimizing two “gold” structures and the results are compared to the outcomes reported in literature.

Bibliography

[1] F. Hopkinson, and David Rittenhous, “An Optical Problem, Proposed by Mr. Hopkinson, and Solved by Mr. Rittenhouse,” *Transactions of the American Philosophical Society,* vol. 2, pp. 201-206, 1786.

[2] Jesús del Barrio, and Carlos Sánchez-Somolinos, “Light to Shape the Future: From Photolithography to 4D Printing,” *Advanced Optical Materials,* vol. 7, no. 16, pp. 1900598(1-33), 2019.

[3] Yifang Chen, “Nanofabrication by electron beam lithography and its applications: A review,” *Microelectronic Engineering,* vol. 135, p. 57–72.

[4] Dirk Taillaert, et al., “Compact efficient broadband grating coupler for silicon-on-insulator waveguides,” *Optics Letters,* vol. 29, no. 23, pp. 2749-2751, 2004.

[5] Dirk Taillaert, et al., “Grating Couplers for Coupling between Optical Fibers and Nanophotonic Waveguides,” *Japanese Journal of Applied Physics,* vol. 45, no. 8R, p. 6071–6077, 2006.

[6] Lee Carroll, et al., “Photonic Packaging: Transforming Silicon Photonic Integrated Circuits into Photonic Devices,” *Applied Sciences,* vol. 6, no. 12, pp. 426(1-21), 2016.

[7] Riccardo Marchetti, et al., “Coupling strategies for silicon photonics integrated chips,” *Photonics Research,* vol. 7, no. 2, pp. 201-239, 2019.

[8] Carmelo Scarcella, et al., “Pluggable Single-Mode Fiber-Array-to-PIC Coupling Using Micro-Lenses,” *in IEEE Photonics Technology Letters,* vol. 29, no. 22, pp. 1943-1946, 2017.

[9] “Cornerstone,” [Online]. Available: https://www.cornerstone.sotonfab.co.uk/

[10] ASML, [Online]. Available: https://www.asml.com/en

[11] H. H. Li, “Refractive index of silicon and germanium,” *Journal of Physical and Chemical Reference Data,* vol. 9, no. 3, pp. 561-658, 1980.

[12] I. H. Malitson, “Interspecimen Comparison of the Refractive Index of Fused Silica,” *Journal of the Optical Society of America,* vol. 55, no. 10, pp. 1205-1209, 1965.

[13] Max Born, et al., “Elements of the theory of diffraction,” in *Pinciples of Optics* , Cambridge , Cambridge Press, 1999, pp. 413-417.

[14] Amnon Yariv and Pochi Yeh, “Wave Propagation in Periodic Media,” in *Photonics: optical electronics in modern communications*, Oxford, Oxford University Press, 2007, pp. 573-582.

[15] Bahaa E. A. Saleh, and Malvin Carl Teich, “Wave Optics,” in *Fundamentals of Photonics,* Hoboken, New Jersey, John Wiley & Sons, Inc., 2007, p. 56.

[16] Giorgio Quaranta, et al., “Recent Advances in Resonant Waveguide Gratings,” *Laser & Photonics Review,* vol. 12, no. 9, pp. 1800017 (1-31), 2018.

[17] Zan Zhang, et al., “Efficiency Enhanced Grating Coupler for Perfectly Vertical Fiber-to-Chip Coupling,” *Materials (Basel),* vol. 13, no. 12, pp. 2681(1-11), 2020.

[18] Zan Zhang, et al., “Broadband High-Efficiency Grating Couplers for Perfectly Vertical Fiber-to-Chip Coupling Enhanced by Fabry-Perot-like Cavity,” *Micromachines,* vol. 11, no. 9, pp. 859(1-12), 2020.

[19] Lirong Cheng, et al., “Perfectly Vertical Grating Coupler for O and C-band,” in *Frontiers in Optics + Laser Science APS/DLS,*, Washington, DC United States, 2019.

[20] Gyeongho Son, et al., “High-efficiency broadband light coupling between optical fibers and photonic integrated circuits,” *Nanophotonics,* vol. 7, no. 12, p. 1845–1864, 2018.

[21] John C. Brazas and Lifeng Li, “Analysis of input-grating couplers having finite lengths,” *Applied Optics,* vol. 34, no. 19, pp. 3786-3792, 1995.

[22] Lirong Cheng, et al., “Grating Couplers on Silicon Photonics: Design Principles, Emerging Trends and Practical Issues,” *Micromachines,* vol. 11, no. 7, pp. 666(1-25), 2020.

[23] Siddharth Nambiar, et al., “Grating-Assisted Fiber to Chip Coupling for SOI Photonic Circuits,” *Applied Sciences* , vol. 8, no. 7, pp. 1142(1-22), 2018.

[24] Corning® SMF-28®, [Online]. Available: https://www.corning.com/media/worldwide/coc/documents/Fiber/SMF-28%20Ultra.pdf

[25] Deidrick Vermeulen, et al., “High-efficiency fiber-to-chip grating couplers realized using an advanced CMOS-compatible Silicon-On-Insulator platform,” *Optics Express,* vol. 18, no. 17, pp. 18278-18283, 2010.

[26] Europractice, “CORNERSTONE STANDARD COMPONENTS LIBRARY,” [Online]. Available: https://europractice-ic.com/wp-content/uploads/2020/07/CORNERSTONE-Standard-Components-Library_SOI.pdf

[27] Rongrui Liu, et al, “A high-efficiency grating coupler between single-mode fiber and silicon-on-insulator waveguide,” *Journal of Semiconductors May 2017,* vol. 38, no. 5, pp. 054007(1-4), 2017.

[28] Yunfei Fu, et al., “Efficient adiabatic silicon-on-insulator waveguide taper,” *Photonics Research,* vol. 2, no. 3, pp. A41-A44, 2014.

[29] Frederik Van Laere, et al., “Compact Focusing Grating Couplers for Silicon-on-Insulator Integrated Circuits,” *IEEE Photonics Technology Letters,* vol. 19, no. 23, pp. 1919-1921, 2007.

[30] Juichi Noda, et al., “Polarization-maintaining fibers and their applications,” *Journal of Lightwave Technology,* vol. 4, no. 8, pp. 1071-1089, 1986.

[31] Xia Chen, et al., “Two dimensional silicon waveguide chirped grating couplers for vertical optical fibers,” *Optics Communications,* vol. 283, no. 10, p. 2146–2149, 2010.

[32] Lee Carroll, et al., “Broad parameter optimization of polarization-diversity 2D grating couplers for silicon photonics,” *Optics Express,* vol. 21, no. 18, pp. 21556-21568, 2013.

[33] Jinghui Zou, et al., “Single step etched two dimensional grating coupler based on the SOI platform,” *Optics Express*, vol. 23, no. 25, pp. 32490-32495, 2015.

[34] Jinghui Zou, et al., “Two-dimensional grating coupler with a low polarization dependent loss of 0.25 dB covering the C-band,” *Optics Letters*, vol. 41, no. 18, pp. 4206-4209, 2016.

[35] Yanyun Xue, et al., “Two-dimensional silicon photonic grating coupler with low polarization-dependent loss and high tolerance,” *Optics Express*, vol. 27, no. 16, pp. 22268-22274, 2019.

[36] Tatsuhiko Watanabe, et al., “2-D Grating Couplers for Vertical Fiber Coupling in Two Polarizations,” *IEEE Photonics Journal*, vol. 11, no. 4, pp. 1-9, 2019.

[37] Tatsuhiko Watanabe, et al., “Coherent few mode demultiplexer realized as a 2D grating coupler array in silicon,” *Optics Express*, vol. 28, no. 24, pp. 36009-36019, 2020.

[38] Ansys / Lumerical , “Lumerical FDTD,” [Online]. Available: https://www.lumerical.com/products/fdtd/

[39] Frank Olyslager, Electromagnetic Waveguides and Transmission Lines, Oxford: Oxford University Press, 1999.

[40] Ralf Waldhäusl, et al., “Efficient coupling into polymer waveguides by gratings,” *Applied Optics*, vol. 36, no. 36, pp. 9383-9390, 1997.

[41] Frederik Van Laere, et al., “Compact and Highly Efficient Grating Couplers Between Optical Fiber and Nanophotonic Waveguides,” *Journal of Lightwave Technology*, vol. 25, no. 1, pp. 151-156, 2007.

[42] Wissem Sfar Zaoui, et al., “Cost-effective CMOS-compatible grating couplers with backside metal mirror and 69% coupling efficiency,” *Optics Express*, vol. 20, no. 26, pp. B238-B243, 2012.

[43] Wissem Sfar Zaoui, et al., “Bridging the gap between optical fibers and silicon photonic integrated circuits,” *Optics Express*, vol. 22, no. 2, pp. 1277-1286, 2014.

[44] Günther Roelkens, et al., “High efficiency Silicon-on-Insulator grating coupler based on a poly-Silicon overlay,” *Optics Express,* vol. 14, no. 24, pp. 11622-11630, 2006.

[45] Xia Chen, et al., “Apodized Waveguide Grating Couplers for Efficient Coupling to Optical Fibers,” *IEEE Photonics Technology Letters,* vol. 22, no. 15, pp. 1156-1158, 2010.

[46] Zhexin Zhao and Shanhui Fan, “Design Principles of Apodized Grating Couplers,” *Journal of Lightwave Technology,* vol. 38, no. 16, pp. 4435-4446, 2020.

[47] Angelo Bozzola, et al., “Optimising apodized grating couplers in a pure SOI platform to −0.5 dB coupling efficiency,” *Optics Express,* vol. 23, no. 12, pp. 16289-16304, 2015.

[48] Chao Li, et al., “CMOS-compatible high efficiency double-etched apodized waveguide grating coupler,” *OPTICS EXPRESS,* vol. 21, no. 7, pp. 7868-7874, 2013.

[49] Shuyi Li, et al., “Deterministic design of focusing apodized,” *Optics Express,* vol. 28, no. 93, pp. 35395-35412, 2020.

[50] Li He, et al., “A High-Efficiency Nonuniform Grating Coupler Realized With 248-nm Optical Lithography,” *IEEE PHOTONICS TECHNOLOGY LETTERS,* vol. 25, no. 14, pp. 1358-1361, 2013.

[51] Riccardo Marchetti, et al., “High-efficiency grating-couplers: demonstration of a new design strategy,” *Scientific Reports,* vol. 7, no. 16670, pp. 1-8, 2017.

[52] Jacob Robinson and Yahya Rahmat-Samii, “Particle Swarm Optimization in Electromagnetics,” *IEEE Transactions on Antennas and Propagation,* vol. 52, no. 2, pp. 397-407, 2004.

[53] James Kennedy and Russell Eberhart, “Particle Swarm Optimization,” in *Proceedings of ICNN'95 - International Conference on Neural Networks*, Perth, WA, Australia, 1995.

[54] Rania Hassan, et al., “A Comparison of Particle Swarm Optimization and the Genetic Algorithm,” in *46th AIAA/ASME/ASCE/AHS/ASC Structures, Structural Dynamics and Materials Conference*, Austin, Texas,USA, 2005.

[55] Luca Zagaglia, et al., “Optimized Design Procedure for Low-cost Grating-couplers in Photonics-packaging,” in *2019 PhotonIcs & Electromagnetics Research Symposium - Spring (PIERS-Spring)*, Rome, Italy, 2019.

[56] Klayout, “About The Project,” Klayout, [Online]. Available: https://www.klayout.de/intro.html

[57] Bradley Snyder, and Peter O'Brien, “Packaging Process for Grating-Coupled Silicon Photonic Waveguides Using Angle-Polished Fibers,” *IEEE Transactions on Components, Packaging and Manufacturing Technology*, vol. 3, no. 6, pp. 954-959, 2013.

[58] Bradley Snyder, et al., “Hybrid Integration of the Wavelength-Tunable Laser With a Silicon Photonic Integrated Circuit,” *Journal Of Lightwave Technology,* vol. 31, no. 24, pp. 3934-3942, 2013.

[59] Lee Carroll, et al., “Photonic Packaging: Transforming Silicon Photonic Integrated Circuits into Photonic Devices,” *Applied Sciences,* vol. 6, no. 12, pp. 426(1-21), 2016.

[60] Chao Li, et al., “Silicon photonics packaging with lateral fiber coupling to apodized grating coupler embedded circuit,” *Optics Express,* vol. 22, no. 20, pp. 24235-24240, 2014.

[61] Luca Zagaglia, et al., “Experimental Characterization of Particle Swarm Optimized Focusing Non-Uniform Grating Coupler for Multiple SOI Thicknesses,” *Journal of Lightwave Technology,* pp. 1-7, 2021.

Chapter 3

Design, Fabrication and Tests of the Optimized Non-Uniform Grating Designs

In the previous chapter, the theory of grating couplers (GCs) was presented together with a detailed explanation of the design routine with particular attention on the structure of the Particle Swarm Optimization Algorithm (PSO). Chapter 3 reports its application to the optimization of non-uniform GCs for the horizontal fiber (HFb) coupling scheme. Then, it focuses on the fabrication and optical characterization of the optimized structures with the analysis of the experimental coupling efficiencies (CEs) at 1550nm, comparing them with the computational expectations. An insight on the physics behind such non-uniform GCs is provided exploiting the FDTD method to calculate the integrated scattering strength and the effective refractive index variation for each optimized design.

3.1 Design and optimization of the non-uniform GCs

The designed rule developed by Marchetti *et al.* [1] for the apodization of the GC periods represents the beginning of the design process, as proven to be reliable in showing high-performances and small-discrepancy respect to the theoretical predictions due to well tolerance in tight variations of the structural parameters. The duty-cycle changes along the apodization direction **x** following the equation

13

$$DC(x) = \mathrm{DC}_0 - Ax$$

Where DC_0 is the initial duty-cycle and A is the apodization parameter. The local pitches (Λ_i) are calculated taking advantage of Bragg's equation

14

$$\Lambda_i(x) = \frac{\lambda_t}{n_{eff}^{AVG} - n_{SiO2} * \sin(\theta_i)}$$

where λ_t=1550nm, n_{eff}^{AVG} is the averaged effective refractive index of the local pitch, n_{SiO2} =1.44 is the refractive index of the TOX layer, and θ_i=10° the angle of incidence inside the TOX. The n_{eff}^{AVG} is calculated through geometrical assumptions as described in [1] resorting to an external Python code that resolves numerically the 2D WG electromagnetic problem, where the refractive index of the Si layer is set equal to 3.48.

Then, the structure is precisely tuned at each step of the PSO through an iterative process that introduces a mismatch compensation factor accounting for the approximate estimation of n_{eff}^{AVG}, as described by Passoni *et al.* in [2]. This apodization rule has been implemented inside the PSO routine in order to seek for the best apodization parameter (*A*), etching depth (ED), and initial duty cycle (DC_0), where opportune boundary conditions at the parameter space are imposed on the initial DC_0, in order to respect the constrains imposed by e-beam lithography and limit the minimum features size at 50nm.

The flow diagram representing the process flow of the optimization routine is reported in Figure 29.

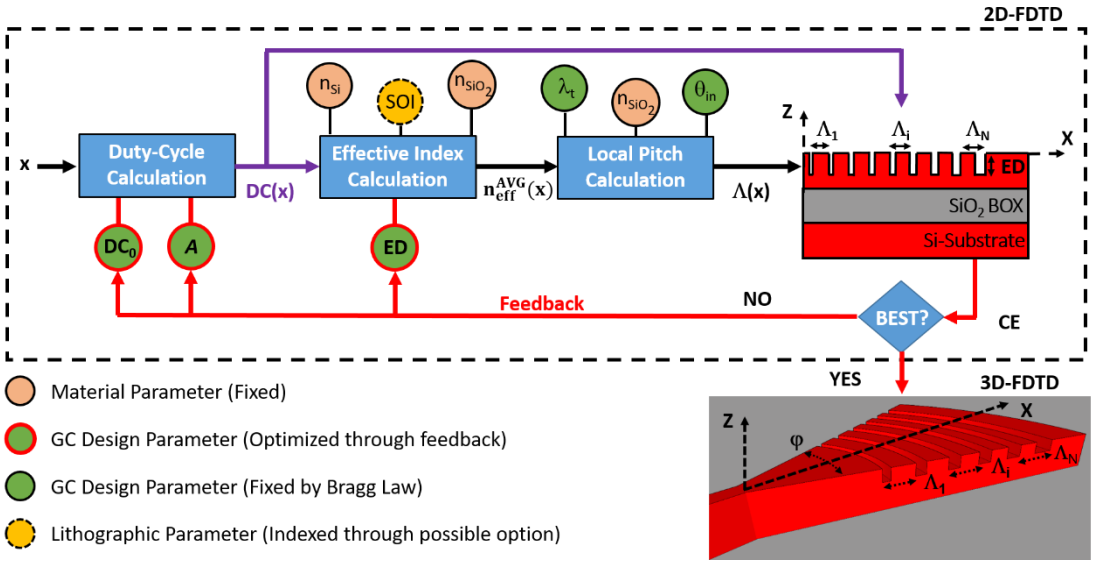

Figure 29: Visual representation of the flow diagram related to the PSO routine used to optimize the non-uniform GCs. The Figure has been taken from [3].

2D-FDTD simulations were exploited to compute the HFb emission, which MFD was capture at the interface between the fiber cladding and the PIC top-oxide layer. In

this way, a corresponding Gaussian source, reproducing the HFb emission, was exploited as a light source inside the PSO, resulting in a dramatic reduction of the simulation time due to the reduced dimension of the FDTD simulation region.

In particular, the TOX thickness was not optimized during the design routine as an Epoxy resin with a refractive index of 1.44 was selected to be used for the measurements to fill the air gap between the HFb and the TOX layer.

The e-beam lithographic technique was targeted as it can guarantee the required resolution at the nanometres scale to: (i) reproduce with the best degree of fidelity offered by todays fabrication processes the features of the different best designs, (ii) resolve the small geometrical features proper of non-uniform GCs that require a resolution at the nanometres scale, (iii) compete with the best performers reported in literature for the VFb coupling scheme.

The final 2D optimized structure for each SOI thickness is used to construct the corresponding 3D focusing non-uniform GC, in order to test the focusing effect and the corresponding injection inside the WG. In particular, a best focusing angle (φ) equal to 40° guarantees an excellent injection into the WG for all the SOI thicknesses and all the best theoretical parameters for each GC design are summarized in Table 1.

Table 1: PSO optimized structural parameters for each SOI thickness. Data taken from [3].

SOI Thickness (nm)	**Apodization factor (*A*) (nm^{-1})**	**Etching Depth (ED) (nm)**	**Initial Duty-Cycle (DC_0)**	**Compensation Factor**
220	**27477E-9**	**94**	**0.9**	**1.002**
260	**27072E-9**	**133**	**0.9**	**1.016**
290	**27162E-9**	**176**	**0.9**	**1.024**
320	**28369E-9**	**189**	**0.9**	**1.023**
340	**28675E-9**	**209**	**0.9**	**1.024**

3.2 Fabrication, Test, and Analysis of the non-uniform GCs

The final 3D focusing non-uniform GC structures were fabricated at the University of Southampton through CORNERSTONE [4], its open source silicon photonics foundry.

Here, multiple samples for each design were fabricated introducing different biases on purpose in order to lithographically tune the structures together with additional

spiral structures in order to account for the additional WG propagation losses for each chip.

The detail layouts of the measurement coupling scheme and the chip are reported in Figure 30. An optical shunt WG is used to actively align the input (IC) and output

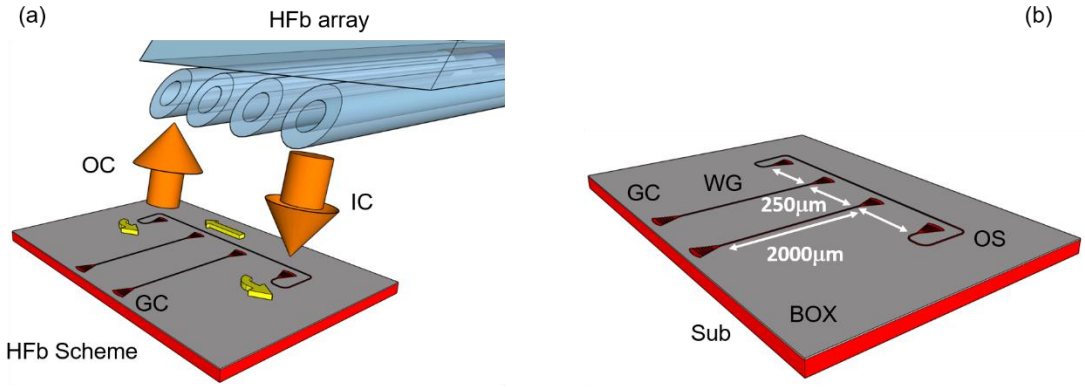

Figure 30: Measurement layout: (a) Horizontal fiber coupling scheme (HFb array). The light is injected into the chip via the Input Channel (IC) and collected through the Output Channel (OC). The light propagation is pointed out by the orange arrows in the farfield and yellow arrows inside the chip WG. (b) Chip layout with the optical shunt waveguide (OS), two straight WGs, all the GCs, the BOX, and the Substrate (Sub). The Figure has been taken from [3].

(OC) channels of the HFb and two additional straight WGs are used as additional control channels for the WG losses.

A campaign of broadband measurements was conducted to obtain the transmittance used to evaluate the CEs; in particular, Figure 31 panel (a) shows a picture of the HFb coupling scheme taken during the measurements, while a picture of the chip layout for one of the sample is showed in Figure 31 panel (b).

A superluminescence diode (SLD) Superlum SLD-761-LP was employed as a broadband light source. The SLD emission was directly coupled into a manual fibre polarization controller, Thorlabs FPC030, to manage the polarization state. A standard fiber connector was used to connect the polarization controller with the single channel of a 12 core HFb array by CXFIBER. Each channel is composed of a single mode fibre with a MFD=10.4μm, and polishing angle of 50°. A customize auto-aligner machine, composed by Newport components, was exploited to perform the alignment

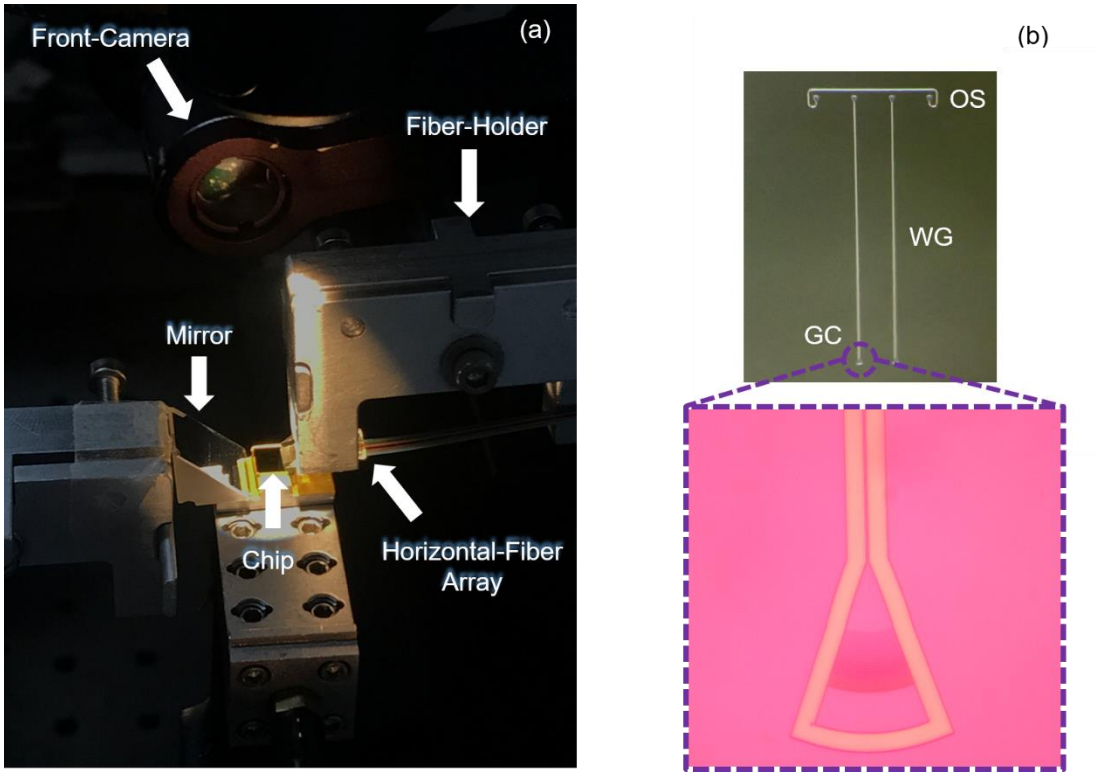

Figure 31: (a) Picture of the HFb coupling scheme used for the experimental characterization. The front-camera, the fiber-holder, the mirror, the HFb array, and the chip are pointed out. (b) Picture taken with the optical microscope of the chip layout. The OS, and WGs are pointed out as well as a zoom of the GC structure.

process with a half micron accuracy in in-plane alignment of the fibre array respect to the input and output channels on the chip. The output channel was connected to a calibrated power meter, Newport Dual-Channel Power Meter model 2832C, to execute the active alignment with the aim of maximizing the signal. The Norland Optical Adhesive 144 EPOXY resin was employed to obtain a refractive index matching condition between the cladding of the HFb and the TOX layer. Eventually, an optical spectrum analyser, Anritsu model MS910C, was used to record the spectrum of the SLD (P_{in}), which represented the reference to measure the CE, and the transmitted light through the output channel (P_{out}) at the optimized position. The optical spectrum analyser measures the two transmittances in dBm and the IL can be obtained directly subtracting P_{out}, the WG and the fiber connectors losses from P_{in}. Being the system invariant under time-reversal symmetry [5], the input and output channels can be reversed, thus the IL proper of a single GC can be evaluated dividing P_{out} by two. Then, the result is converted in percentage to obtain the CE.

The samples that showed the highest value of CEs, for each SOI thickness, were than selected to compare the results with the theoretical predictions related to the 2D- and 3D-FDTD simulations. The results are reported in Figure 32.

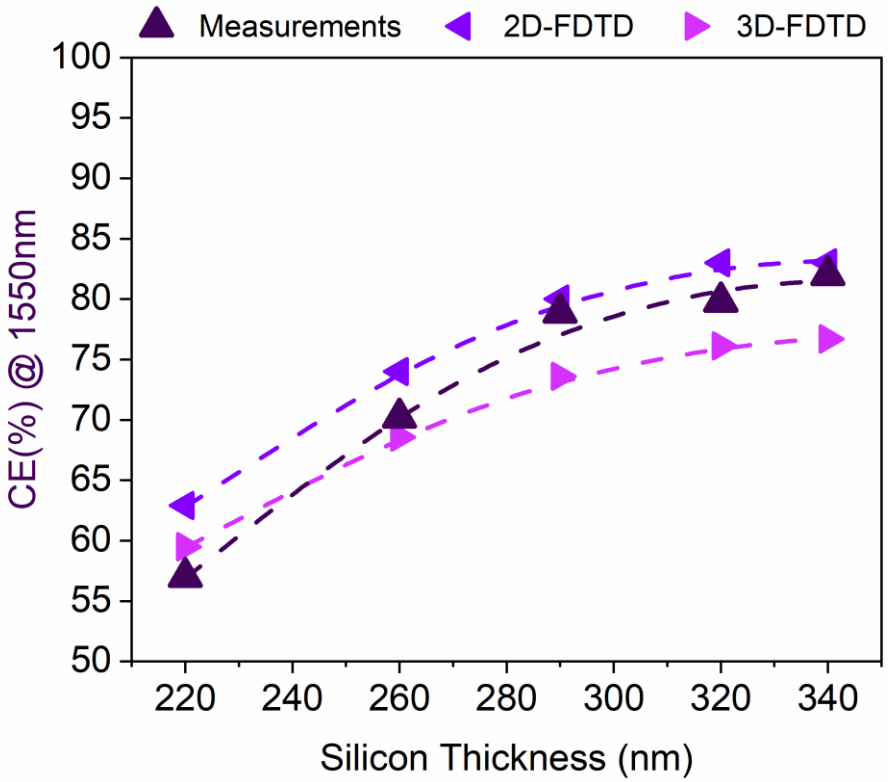

Figure 32: Comparison of the best measured CEs values at 1550nm and the corresponding 2D-FDTD, and 3D-FDTD results. The Figure has been taken from [3].

The experimental results are shown together with the computational predictions extracted from the 2D- and 3D-FDTD simulations. The three frameworks are in excellent agreement with an average difference across the all the data of about 3%. In addition, the 2D-FDTD data can be compared with the results reported in literature for a similar study where a VFb coupling scheme is considered [6]. Here, a 5% reduction in the CEs respect to the values reported in the article is reasonable as the structures proposed in this thesis are optimized for a wider MFD resulting in a lower scattering strength.

The agreement between the 2D and 3D CEs is better than 95% and the higher decreasing seen at thicker SOIs can be linked to the mesh accuracy that influences the sampling capacity of the curved shape of the GC teeth. Furthermore, the thicker the SOI layer, the grater the amount of material that can be potentially under-sampled resulting in a higher difference between the 2D and 3D predictions.

The measured CEs increase monotonically from 56% for the 220nm-thick platform to 83% for the 340nm-thick SOI with a behaviour compatible with a quadratic fit of the data in accordance with the FDTD results. This drastic improvement of the performance can be related to a greater scattering strength offered by thicker SOI layers. Moreover, Figure 32 can be divided into two separate regions: the first one formed by the 220nm- and 260nm-thick SOI, and the second one composed by the remaining thicknesses.

While the first one shows a drastic increment of the CEs from 56% to almost 70%; the second region is characterized by an almost equal CE value across the different Si thicknesses varying only of few percentage resulting in an almost flat behaviour. This suggests the existence of an upper limit in the scattering strength achievable by simply increasing the Si layer as direct consequence of a limitation in the reduction of the channel of losses, *i.e.* the reflectance and transmittance. Moreover, in [6], the authors optimized non-uniform GCs going beyond the 340nm Si thickness showing computationally a progressive reduction in the CE at thicker SOIs.

Finally, the measured CEs for the two standard platform display competitiveness compared to the best performers reported in literature so far for the well-established VFb scheme [7, 8]. For the sake of completeness, the measured and the computational 2D- and 3D-FDTD multiwavelength CEs for each SOI thickness are reported for each SOI in Figure 33. Again, the excellent agreement between the three frameworks can be appreciated.

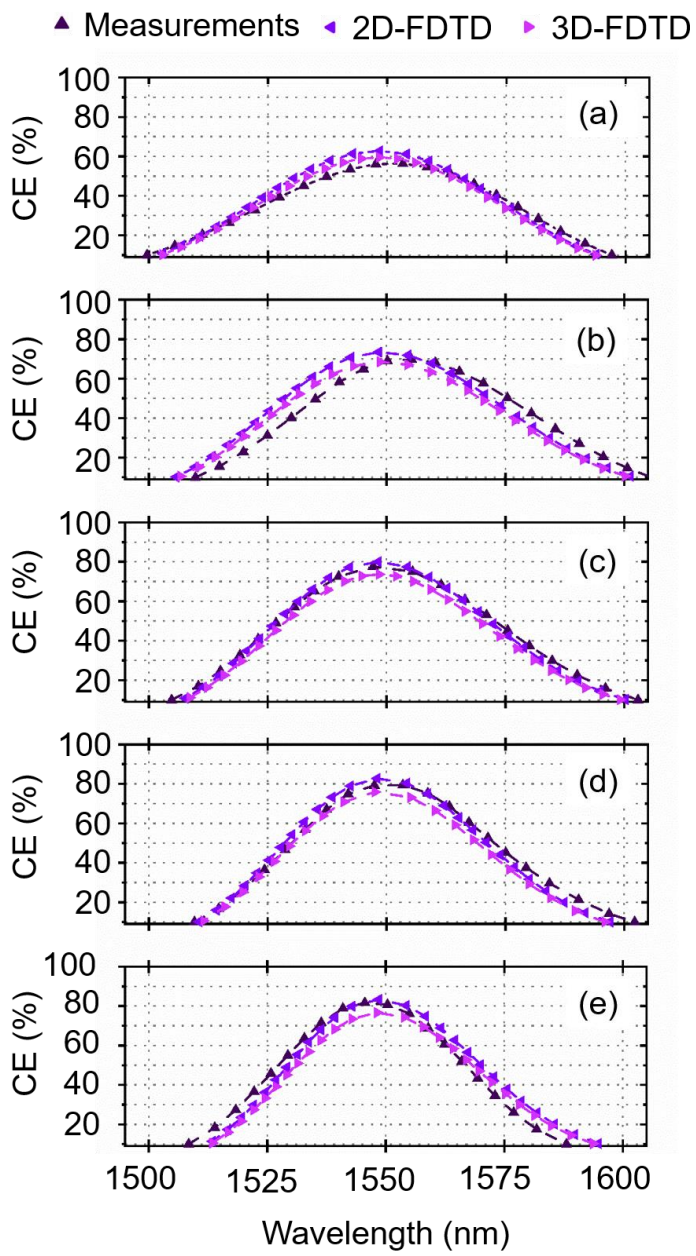

Figure 33: Multi-wavelength CEs: (a) 220nm-thick SOI, (b) 260nm-thick SOI, (c) 290nm-thick SOI, (d) 320nm-thick SOI, and (e) 340nm-thick SOI. The Figure has been taken from [3].

In particular, the 1dB and 3dB BWs were calculated exploiting Figure 33 and the results regarding the measurements are summarized, below, in Table 2.

Table 2: Measured 1dB and 3dB BWs for each SOI thickness. Data taken from [3].

SOI Thickness (nm)	**1dB BW (nm)**	**3dB BW (nm)**
220	**37**	**63**
260	**33**	**58**
290	**33**	**57**
320	**30**	**52**
340	**27**	**46**

The behaviour of the CEs(λ_t) can be studied resorting to the two main parameters that fix the performances of a GC: the directionality and the reflectivity. These two depend exclusively from the structural parameters of the GC and give information on the scattering process that takes place inside the WG layer. However, the function that links the directionality and the reflectivity directly to the GC structure are respectively the scattering strength (α) and the effective refractive index (n_{eff}), that affects the impedance matching along the GCs.

Thus, these parameters are the core concepts behind the analysis of the physics that governs the performances of each structure.

As seen previously, the scattering strength α is a constant value that affects the exponential decay of the emission profile proper of a uniform GC. For non-uniform GC, the latter is a function of x as the duty cycle changes across the GC length. In particular, the scattering strength can be used to design non-uniform GC as the tuning parameter for the emission profile of the GC, making it as closer as possible to a Gaussian profile to guarantee the best overlap with the fibre mode [9]. This parameter can be defined as

15

$$2 * \alpha(x, \lambda_t) = \frac{I^2(x, \lambda_t)}{I_0^2 - \int_{x_0}^{x} I^2(t, \lambda_t) dt}$$

where $I^2(X)$ is the scattered power intensity evaluated point by point, I_0^2 is the initial power intensity coming from the injection medium.

As it can be seen, the scattering strength is the emission power normalized at each

spatial position for the remaining power inside the GC layer. Thus, it weights the ability of each period of the GC in scattering out the light propagating inside the WG layer. As a consequence, the integral of $\alpha(x,\lambda_t)$ along the apodization direction can be used to obtain a spatial integrated scattering strength independent from x, in analogy with the uniform GC, indicated as α_{int}, useful to compare the different GC designs. The $\alpha(x,\lambda_t)$ can be evaluated through the FDTD method simply considering the GC in an outcoupling configuration where the light is injected from the WG, and collected directly outside the GC, as depicted in Figure 34.

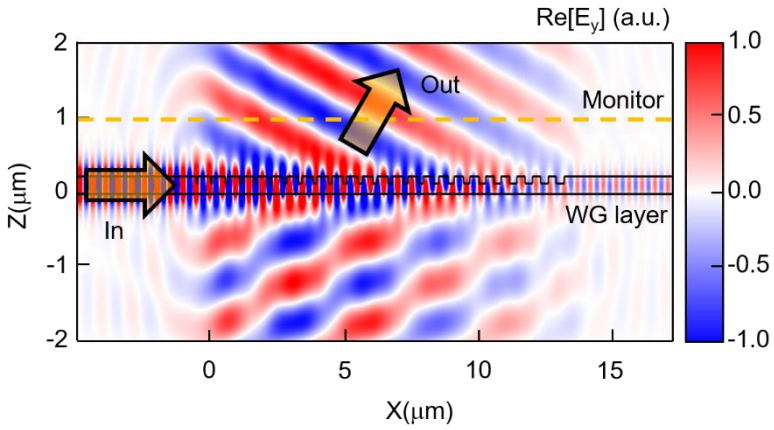

Figure 34: Example of a 2D-FDTD simulation used to evaluate the integrated scattering strength (α_{int}) exploiting the GC in an outcoupling configuration. The light injection and travelling is described by the yellow IN and OUT arrows. The power density is collected through the Monitor. The Figure has been taken from [3].

The same procedure is performed for all the SOI thicknesses and the α_{int} variation as a function of the SOI thickness is reported in Figure 35.

As it can be noticed, α_{int} increases monotonically with the SOI thickness and its behaviour is compatible with a second order polynomial fit, as pointed out for the CE, resulting in a better directionality for thicker SOI, and consequently a superior ability in diffracting in- and out- the incoming light.

Again, a drastic increment is appreciated between the 220nm- and 260nm-thick SOIs, while a progressive flattening of the curve can be pointed out approaching the 340nm platform. These behaviours are in agreement with the computational and measured results displayed in Figure 32 showing the important role of the scattering strength in defining the performance of the GCs.

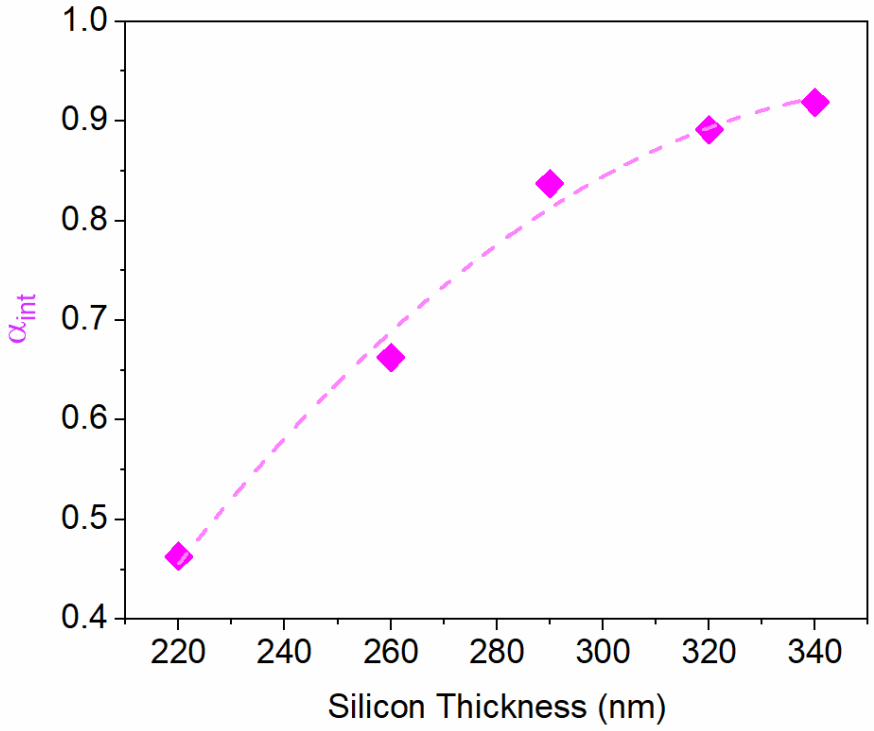

Figure 35: Integrated scattering strength (α_{int}) calculated through 2D-FDTD simulation for the different SOI thicknesses. The pink dashed-line represents a second order polynomial fit. The Figure has been taken from [3].

Instead, the impedance matching variation along each GC is calculated exploiting a photonic bandstructure approach [10, 11], where the bandstructure effective refractive index (n_{eff}^{BS}) at each Λ_i is calculated going beyond the simple n_{eff}^{AVG} evaluation used during the PSO optimization. Here, the non-uniform GC is considered as a series of pitch junctions [12], each of them treated as a locally uniform GC, scanning the entire length of each structure. The FDTD method can be exploited to calculate the dispersion relation curves, *i.e.* ω vs k, for each GC and the corresponding n_{eff}^{BS} can be evaluated as $n_{eff}^{BS} = \frac{\lambda_t}{2\pi}k = \frac{c}{\omega}k$. The results are reported in Figure 36 where n_{eff}^{BS} is plotted as a function of the pitch number i.

The linear trends suggest that the linear apodization of the duty cycle, which is a structural parameter, results in a linear decreasing of the impedance from the 1st to the 24th GC pitch, property related to the electromagnetic field.

Figure 36 enables a direct comparison between each GC structure. The n_{eff}^{BS} depends from the etching depth and, in particular, the ratio between the etching depth and the SOI thickness increases for thicker platforms, as can be calculated from Table

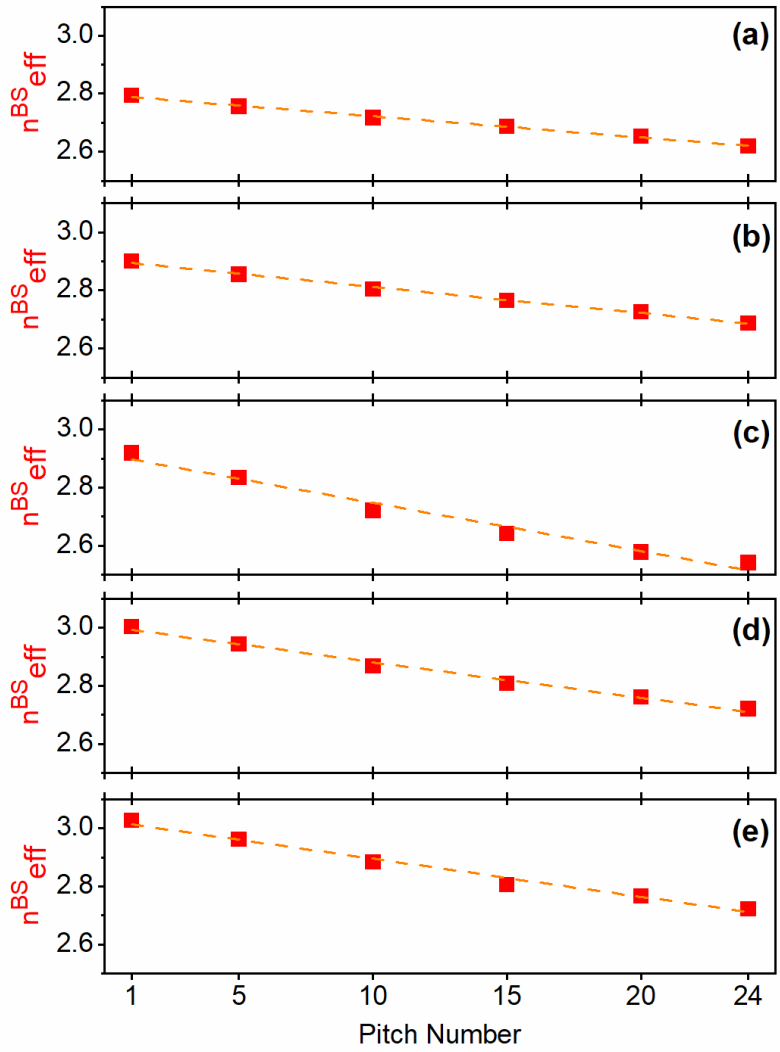

Figure 36: Effective refractive index calculated exploiting 2D-FDTD simulations and a bandstructure approach for the different pitch number of the optimized GC designs for each SOI thickness: (a) 220nm-thick SOI, (b) 260nm-thick SOI, (c) 290nm-thick SOI, (d) 320nm-thick SOI, and (e) 340nm-thick SOI. The Figure has been taken from [3].

1, resulting in a higher deviation between the impedance of the waveguide and the one proper of the contiguous local pitch, i.e. 1st.

As a consequence, the slope of the linear variations tends to increase from panel (a) to panel (e) guaranteeing the closure in the impedance matching gap for an equal number of pitches. The 290nm-thick SOI represents the only variation in this behaviour and further investigation may be considered. If a linear fit of the data is performed, an average slope of 0.013 can be evaluated showing a smoother apodization of the n_{eff}^{BS} compared to the linear apodization of either the duty cycle and the Λ_i.

The linear variations of the PSO optimized duty cycle and the corresponding Λ_i as a function of the period number are reported in Figure 37 for each SOI thicknesses.

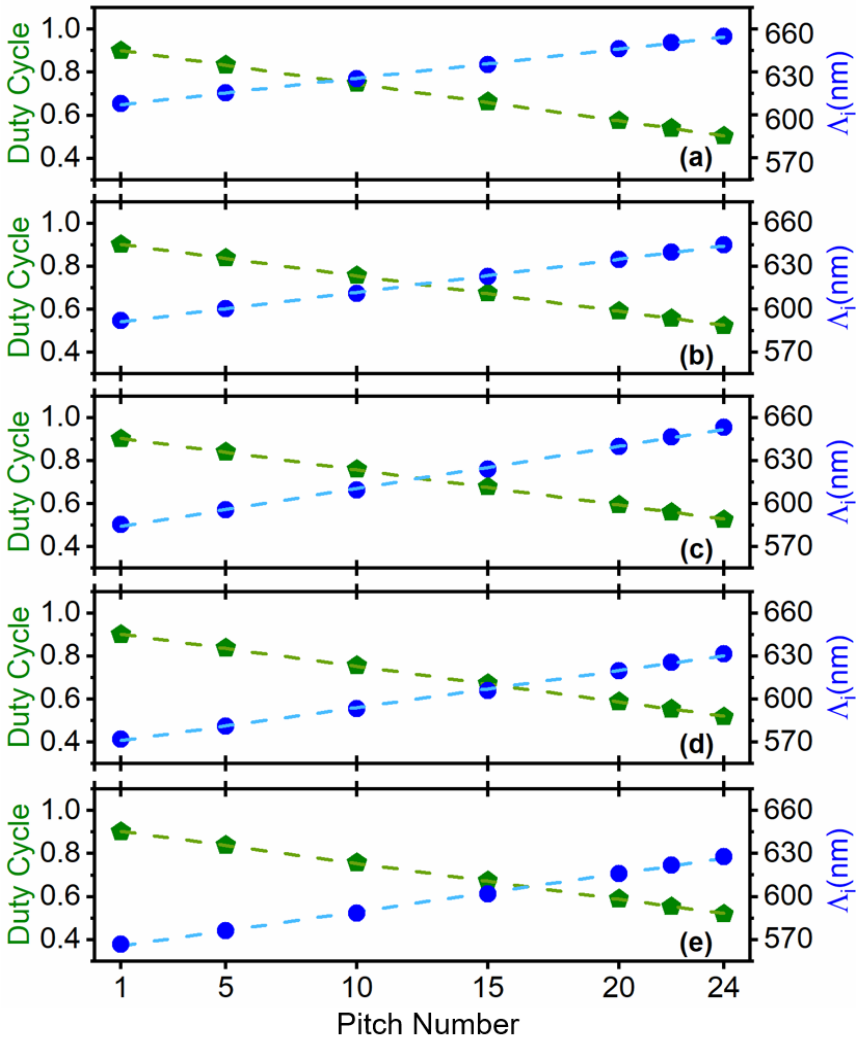

Figure 37: Comparison between the PSO optimized duty cycles and local pitches (Λ_i) as a function of the period number for each SOI thickness: (a) 220nm-thick SOI, (b) 260nm-thick SOI, (c) 290nm-thick SOI, (d) 320nm-thick SOI, (e) 340nm-thick SOI. The Figure has been taken from [3].

As a consequence, a smoother impedance matching variation guarantees low values of the reflectivity, increasing the CE.

In summary, looking at the directionality and the reflectivity, it is easier to understand why the 340nm platform is the best performer above all. In fact, while the impedance matching with its linear trend is similar for all the structures resulting in low reflectivity values comparable between the platforms; the α_{int} shows a drastic improvement moving from the 220nm to the 340nm platforms affecting the CE behaviour.

In particular, the reflectivity around λ_t can be estimated exploiting the Fabry-Pérot ripples of the experimental multiwavelength CEs to have a feedback on back reflections arising due to the difference, in the effective refractive index, between the

WG and the GC regions, following the same procedure reported in [13]. The corresponding results are reported in Table 3 for each SOI thickness.

Table 3: Measured Reflectivity values for each SOI thickness. Data taken from [3].

SOI Thickness (nm)	Reflectivity (%)
220	0.3
260	0.2
290	0.5
320	0.2
340	0.4

The reflectivity values do not show a dramatic difference across the different SOIs in accordance with the analysis of the n_{eff}^{BS} reported in Figure 36, supporting the good quality of the optical impedance matching ensured by the apodization of the local pitches. Moreover, 2D-FDTD simulations were also performed in order to go beyond the reflectivity dependence simply around λ_t, expanding the previous analysis to a spectral interval of about 100nm, and the corresponding results are reported in Figure 38.

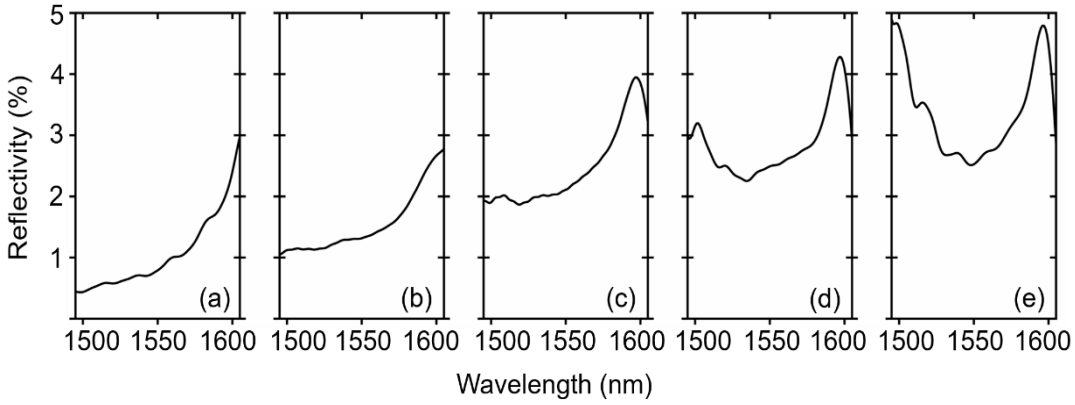

Figure 38: Computational Reflectivity spectra calculated for each SOI thickness exploiting 2D-FDTD simulations for: (a) 220nm-thick SOI, (b) 260nm-thick SOI, (c) 290nm-thick SOI, (d) 320nm-thick SOI, and (e) 340nm-thick SOI. The Figure has been taken from [3].

A slight increase of the reflectivity at λ_t is calculated with values growing from 0.8%, for the 220nm platform, to 2.5%, 340nm-thick SOI. Overall, an increment of 1.5% can be considered negligible from the final CE(λ_t) prospective, compared to the effect introduced by the drastic increment of the α_{int}, between the 220nm- and 340nm-

thick SOI. Again, this computational outcome is in accordance with the analysis of the n_{eff}^{BS}.

On the contrary, the behaviour of the wavelength dependence of the reflectivity changes substantially between the SOI thicknesses. In particular, the 220nm SOI shows an almost flat curve in the (1500÷1550) nm interval, then the reflectivity starts increasing faster and monotonically. A similar situation is seen for either the 260nm and 290nm SOIs, where, for the latter, a peak arises around 1600nm. While, for the 320nm and 340nm SOIs, the behaviour displays a decreasing between (1500÷1550) nm, and a growth across the wavelength interval (1550÷1600) nm, resulting in a minimum around λ_t.

Even though, an explicit link between the reflectivity behaviours and the BW variations across the SOIs is not provided here; a parallelism between the two must hold as both depend on the optical impedance matching. The multiwavelength analysis provided in Figure 38 suggests that the number of wavelengths supported by the local pitches of the non-uniform GC reduces with the SOI thickness, behaviour in accordance with the decreasing of the BWs, *i.e.* the number of wavelength coupled efficiently, as shown in Table 2. This outcome is quite important as the multiwavelength response of such non-uniform GCs is the key-concept of the next chapter.

In addition, a computational check of the optical power ratio (OPR) at λ_t related to the power scattered either upward (OPR_U), downward (OPR_D), forward (OPR_F), and backward (OPR_B), to the input power was conducted through 2D-FDTD simulations, following the scheme shown in Figure 39 and the corresponding data are summarized in Table 4.

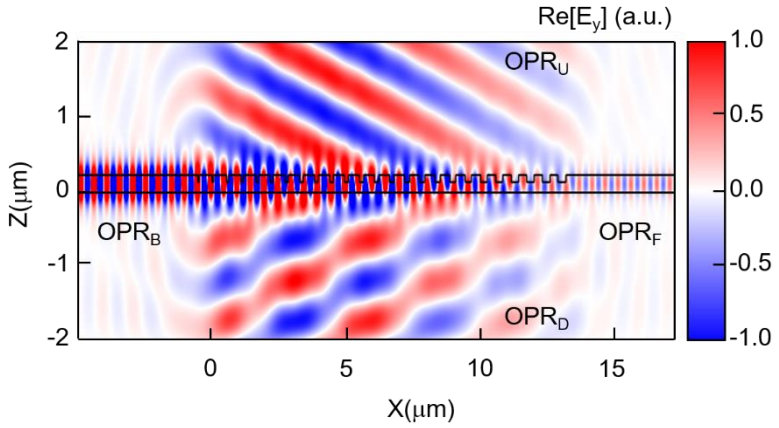

Figure 39: Profile of the real part of the electric field (Ey) computed exploiting a 2D-FDTD simulation at λ_t. The optical power ratio (OPR) are pointed out for the upward channel (OPR_U), downward (OPR_D), forward (OPR_F), and backward (OPR_B). The Figure has been taken from [3].

Table 4: Optical Power Ratio (OPR). Data taken from [3].

SOI Thickness (nm)	OPR_U (%)	OPR_D (%)	OPR_F (%)	OPR_B (%)
220	**66.8**	**31.2**	**1.2**	**0.8**
260	**79.7**	**18.8**	**0.2**	**1.3**
290	**87.3**	**10.4**	**0.2**	**2.1**
320	**88.7**	**7.9**	**0.9**	**2.5**
340	**89.1**	**7.5**	**0.9**	**2.5**

Both the directionality and the reflectivity can be potentially improved further, resulting in higher OPR_U and lower OPR_B, considering more complicated structures based on two-step etching subwavelength L-shaped GCs, as reported in [13, 14, 15, 16, 17].

A study of the structural parameter has been conducted by CORNERSTONE providing an estimation of the etching depth and the first and last trenches widths for the different samples showing low discrepancies of the fabricated features with respect to the computational requirements. The apodization of the local pitches is a non-trivial task to accomplish since the widths of the trenches change from 55/60nm to 300/325nm, across the first and the last one, and the etching rate depends on the trench width. Thus, the widths of the first and last trenches for each samples were checked through the SEM technique.

Regarding the best performers, an averaged deviation, across the different SOIs, of 10nm and 20nm form the targeted values was measured for the first and the last trenches, respectively.

On the other hand, the etching depth was measured exploiting the ellipsometry technique resulting in a deviation of few nanometres from the targeted values, with a maximum estimated deviation of less than 10nm. Indeed, the variation of the etching rate, slower for shallower trenches, can potentially lead to etching depth values equal or smaller than the targeted ones for the first trenches. However, the mode emitted by the fiber has a Gaussian shape profile and its peak strikes the grating coupler around the tenth tooth. Thus, the first few teeth do not participate to large extent to the diffraction process.

An additional investigation based on SEM analysis has been conducted on an optically characterized 260nm-thick SOI, which was sacrificed to measure the various Λ_i, in order to use the measured local pitches to rebuild the GC inside the FDTD software and check its CE. Figure 40 shows the SEM image of the entire GC structure, panel (a), and a zoom on the i-th and i+1-th pitches, panel (b).

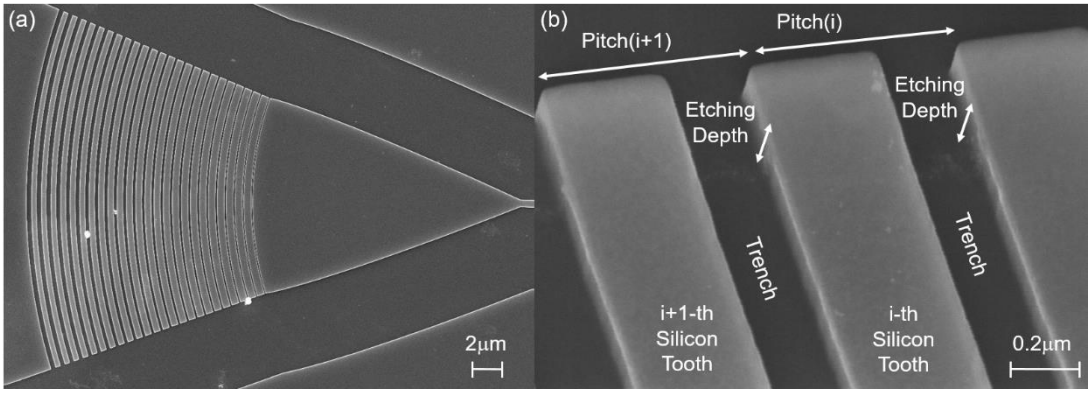

Figure 40: SEM images of a 260nm-thick non-uniform GC: (a) Top-view of the entire GC structure, (b) zoom of the i-th and i+1-th pitches where the etching depth, the trenches, the corresponding teeth are pointed out for clarity purposes. The Figure has been taken from [3].

A discrepancy of 1% respect to the optimized one was verified and the corresponding CE curve is reported in Figure 41.

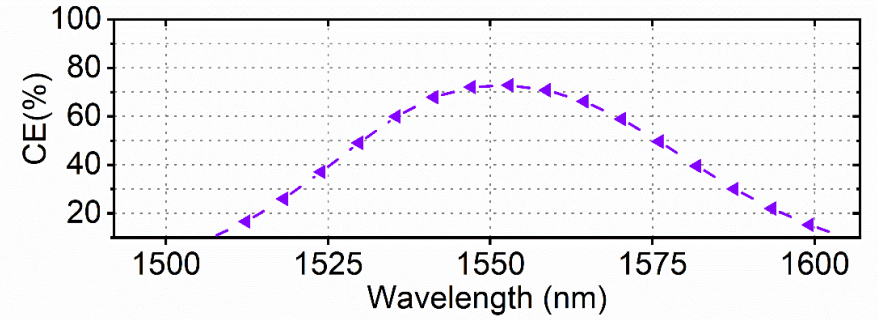

Figure 41: 2D-FDTD CE related to the 260nm-thick non-uniform GC reconstructed through the estimation of the local pitches and trenches widths exploiting the SEM technique. The Figure has been taken from [3]

The choice of this specific structure was done considering the trend of Figure 35. The 290nm-, 320nm-, and 340nm-thick SOIs display a similar α_{int} values flattening the curve, while the 220nm shows the lower value. The 260nm-thick SOI falls inside the plot region where the fastest increment of the α_{int} is appreciated resulting in being the most critical and sensitive in any deviation between each computational α_{int} and the corresponding real one due to a discrepancy in the Λ_i. Thus the 260nm thickness was chosen as the midpoint of this specific region. Moreover, the Λ_i were used to compare the slope of the linear computational and measured trends and a 0.1% difference in their values were evaluated. The variation of the Λ_i is reported in Figure 42.

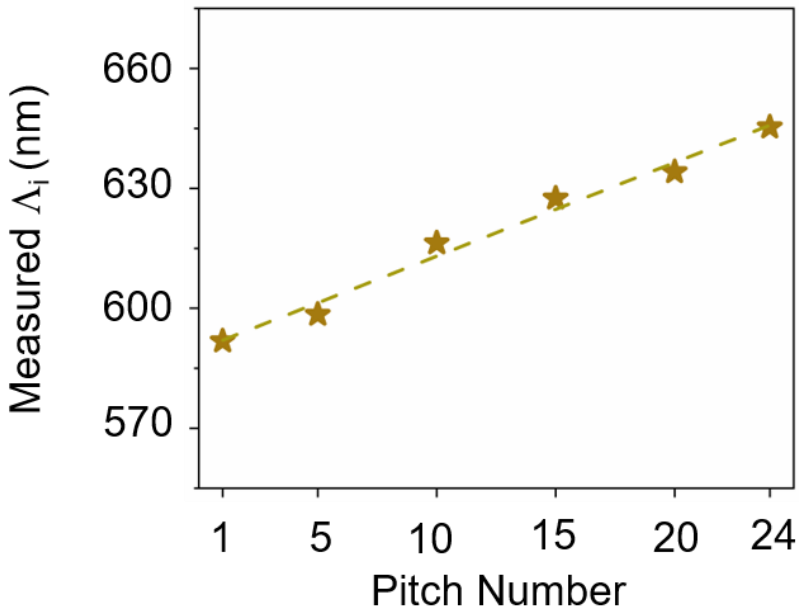

Figure 42: SEM measurements of the local pitches Λ_i for the 260nm-thick SOI non-uniform GC. The Figure has been taken from [3].

In summary, the theoretical and experimental characterizations of the CE of a series of non-uniform GC spanning between the 220nm and 340nm platforms designed for the HFb coupling scheme has been conducted explaining the physics behind their scattering process, which governs and affects their performance.

The PSO reliability in optimizing these structures has been proven with a low discrepancy between the computational and experimental CEs, which show value up to 83% for the 340nm platform.

Due to the introduction and the study of the α_{int} and n_{eff}^{BS}, the CE trend has been directly linked to the structural parameters showing why the 340nm SOI is the best performer above all demonstrating the competitiveness of the HFb, with respect to the VFb, because of the combination of the highest α_{int} and the excellent impedance matching, behaviour similar to the one observed for the uniform-GC with overlay.

To support this result, the 340nm non-uniform design was also optimized and the corresponding samples were fabricated by CORNERSTONE and tested through the same equal measurement set-up at Tyndall exploiting now a VFb coupling scheme and the best measured CE was of the order of 85% with just 2% difference respect to the HFb, [18].

The performances of a GC are not simply limited to the CE(λ_t), but also to either the 1dB or the 3dB BW. Considering the 1dB BW, uniform GCs show values of the order of approximately 40/50nm for 220nm Silicon platform with a VFb coupling scheme, which are two times smaller if compared to the edge coupling technique where a 1dB BW greater than 100nm have been demonstrated [5]. The tighter GC BWs represent a limit for some telecom applications where a flat transmission signal is desirable, such as WDM or frequency-comb generation.

Therefore, in the last few years the research community have put great effort to improve the BW of GCs in order to close the gap with respect to the edge coupling without losing the advantages offered by grating coupling.

In particular, Z. Xiao *et al.* proposed a BW analysis for uniform GC deriving, in [19], an analytic equation to calculate the 1dB BW for uniform GC, showing its dependence on either the dispersion in wavelength of the effective index proper of the GC region and the MFD of the external light source.

Typically, the BW is improved acting on the effective refractive index with the final goal of reducing it exploiting a second uniform GC, which can be made of a

different material such as SiN, created on top of the actual GC [20, 21, 22, 23], or a dispersive cladding [24], or even more complicated 2D-Grating-couplers [25].

An interesting approach to the study of the nature of the BW in uniform GC have been theoretically investigated by Passoni *et al.* in [26] exploiting the photonic crystal theory [10]. In this paper, the authors base their analysis on the coupling process between a quasi-guided mode and a radiative mode showing how the spectral spreading of the CE is caused by two main contributions: one related to the overlap between the spreading in k-space of the fibre mode and the dispersion curve of the GC quasi-guided mode, and the second one to the intrinsic linewidth proper of the dispersion curve related to the quasi-guided mode of the GC.

In this framework, the typical MFD of either the VFb and HFb coupling schemes can be considered "small" enough to guarantee a wide spreading in k-space resulting in a BW dominated by the first aforementioned contribute.

However, to the best of my knowledge, neither a theoretical nor a measurement investigation have been reported so far for non-uniform GCs. Thus, a detailed analysis of the CE curves can be interesting in understanding the effect introduced by the apodization on the actual multiwavelength CE shape and, hence, the BW. In the spirit of the work [26], the physics behind the spectral behaviour of non-uniform GCs represents the main argument of Chapter 4 starting with the work presented at the *10th Young Research Meeting* conference where a first qualitative investigation of the nature of the BW in non-uniform GCs was conducted in reciprocal space showing how it affects the CE curve shapes [27].

3.3 Conclusions

In this chapter, the design routine is applied to optimize multiple non-uniform GCs for different SOI thicknesses for a specific coupling scheme based on a HFb. The latter is quite interesting for Photonics Packaging applications due to its improved mechanical stability and form-factor.

The corresponding optimized designs were fabricated and tested showing excellent agreement in terms of CE with the computational outcomes. In particular, for the standard 340nm-thick platform a CE(λ_t) = 83% was measured, which is one of the highest value ever reported and the results were published in [3]. In addition, an extensive analysis of the physics behind such complex non-uniform GCs is provided

taking into account the spatial integrated scattering strength, a new parameter in this field, and the optical impedance matching through the study of the variation of the effective refractive index, performed through a photonic bandstructure approach.

Finally, a SEM investigation of the local pitches for a 260nm-thick non-uniform GC sample to show the adhesion of such structure to the computational counterpart. The measured local pitches were used to rebuild in a separate 2D-FDTD simulation the corresponding GC, demonstrating that its CE is in excellent agreement with the experimental one.

Bibliography

[1] Riccardo Marchetti, et al., “High-efficiency grating-couplers: demonstration of a new design strategy,” *Scientific Reports,* vol. 7, no. 16670, pp. 1-8, 2017.

[2] Marco Passoni, et al., “Co-optimizing grating couplers for hybrid integration of InP and SOI photonic platforms,” *AIP Advances,* vol. 8, no. 9, pp. 095109(1-7), 2018.

[3] Luca Zagaglia, et al., “Experimental Characterization of Particle Swarm Optimized Focusing Non-Uniform Grating Coupler for Multiple SOI Thicknesses,” *Journal of Lightwave Technology,* pp. 1-7, 2021.

[4] “Cornerstone,” [Online]. Available: https://www.cornerstone.sotonfab.co.uk/

[5] Riccardo Marchetti, et al., “Coupling strategies for silicon photonics integrated chips,” *Photonics Research,* vol. 7, no. 2, pp. 201-239, 2019.

[6] Angelo Bozzola, et al., “Optimising apodized grating couplers in a pure SOI platform to −0.5 dB coupling efficiency,” *Optics Express,* vol. 23, no. 12, pp. 16289-16304, 2015.

[7] Xia Chen, et al., “Apodized Waveguide Grating Couplers for Efficient Coupling to Optical Fibers,” *IEEE Photonics Technology Letters,* vol. 22, no. 15, pp. 1156-1158, 2010.

[8] Li He, et al., “A High-Efficiency Nonuniform Grating Coupler Realized With 248-nm Optical Lithography,” *IEEE PHOTONICS TECHNOLOGY LETTERS,* vol. 25, no. 14, pp. 1358-1361, 2013.

[9] Zhexin Zhao and Shanhui Fan, “Design Principles of Apodized Grating Couplers,” *Journal of Lightwave Technology,* vol. 38, no. 16, pp. 4435-4446, 2020.

[10] John D. Joannopoulos, Photonic Crystals: Molding the Flow of Light (second edition), Princeton, New Jersey, US: Princeton University Press, 2008.

[11] Jelena Notaros, et al., “Ultra-Efficient CMOS Fiber-to-Chip Grating Couplers,” in *Optical Fiber Communication Conference*, Anaheim, California, US, 2016.

[12] Steven G. Johnson, et al., “Adiabatic theorem and continuous coupled-mode theory for efficient taper transitions in photonic crystals,” *Physical Review E,* vol. 66, no. 6, pp. 066608(1-15), 2002.

[13] Daniel Benedikovic, et al., “L-shaped fiber-chip grating couplers with high directionality and low reflectivity fabricated with deep-UV lithography,” *Optics Letters,* vol. 42, no. 17, pp. 3439-3442, 2017.

[14] Daniel Benedikovic, et al., “Sub-decibel silicon grating couplers based on L-shaped waveguides and engineered subwavelength metamaterials,” *Optics Express,* vol. 27, no. 18, pp. 26239-26250, 2019.

[15] Tatsuhiko Watanabe, et al., “Perpendicular Grating Coupler Based on a Blazed Antiback-Reflection Structure,” *Journal of Lightwave Technology*, vol. 35, no. 21, pp. 4663-4669, 2017.

[16] Daniele Melati, et al., “Mapping the global design space of nanophotonic components using machine learning pattern recognition,” *Nature Communications,* vol. 10, no. 4775, pp. 1-9, 2019.

[17] Mohsen Kamandar Dezfouli, et al., “Perfectly vertical surface grating couplers using subwavelength engineering for increased feature sizes,” *Optics Letters,* vol. 45, no. 13, pp. 3701-3704, 2020.

[18] Callum Littlejohns, et al., “CORNERSTONE’s Silicon Photonics Rapid Prototyping Platforms: Current Status and Future Outlook,” *Applied Sciences,* vol. 10, no. 22, pp. 8201(1-34), 2020.

[19] Zhe Xiao, et al., “Bandwidth analysis of waveguide grating,” *Optics Express,* vol. 21, no. 5, pp. 5688-5700, 2013.

[20] Zhe Xiao, et al., “Design for broadband high-efficiency grating couplers,” *Optics Letters,* vol. 37, no. 4, pp. 530-532, 2012.

[21] Mark T. Wade, et al., “75% efficient wide bandwidth grating couplers in a 45 nm microelectronics CMOS process,” in *2015 IEEE Optical Interconnects Conference (OI),* San Diego, CA, US, 2015.

[22] Jason C. C. Mak, et al., “Silicon nitride-on-silicon bi-layer grating couplers designed by a global optimization method,” *Optics Express,* vol. 26, no. 10, pp. 13656-13665, 2018.

[23] Wesley D. Sacher, et al., “Wide bandwidth and high coupling efficiency Si3N4-on-SOI dual-level grating coupler,” *Optics Express,* vol. 22, no. 9, pp. 10938-10947, 2014.

[24] Niklas Hoppe, et al., “Bandwidth-Enhancement of Silicon Grating Couplers Using Dispersive Coatings,” in *2019 International Conference on Numerical Simulation of Optoelectronic Devices (NUSOD)*, Ottawa, ON, CA, 2019.

[25] Qiuhang Zhong, et al., “Focusing-curved subwavelength grating couplers for ultra-broadband silicon photonics optical interfaces,” *Optics Express*, vol. 22, no. 15, pp. 18224-18231, 2014.

[26] Marco Passoni, et al., “Grating couplers in silicon-on-insulator: The role of photonic guided resonances on lineshape and bandwidth,” *Applied Physics Letters,* vol. 110, no. 041107, pp. 1-5, 2017.

[27] Luca Zagaglia, et al., “Analysis in reciprocal space of the band-pass filter effect in uniform and non-uniform grating couplers,” in *Journal of Physics: Conference Series, 10th Young Reseracher Meeting*, Rome, IT, 2020.

Chapter 4

Analysis of the multiwavelength response of non-uniform Grating Couplers

The previous thesis chapter was focused mainly on the results of the optical characterization of the fabricated optimized designs with an analysis of the Coupling Efficiencies (CEs) at 1550nm of the best performing samples. This new chapter is focused on the study of the multiwavelength response of such non-uniform grating couplers (GCs) with particular attention on the CE curve shape, its dependence on either the external mode field diameter and the optical impedance matching enabled by the non-uniform GC pattern, as well as the nature of the BW.

4.1 Qualitative study and analysis in reciprocal space of the band-pass filter effect in non-uniform GCs

The first step in this approach was a computational investigation behind the qualitative multiwavelength response of a uniform and non-uniform GC optimized through the PSO procedure for the VFb coupling scheme.

Figure 43 displays a comparison between the CE curve of a uniform GC designed on a 220nm-thick SOI with a maximum CE(@1550nm)=60% with respect to the CE of a non-uniform GC designed o a 290nm-thick SOI with a CE(@1550nm)=85%. This particular thickness was selected at the time since it was the one with the highest CE value and the greatest asymmetry in the spectrum amongst the different available GC designs.

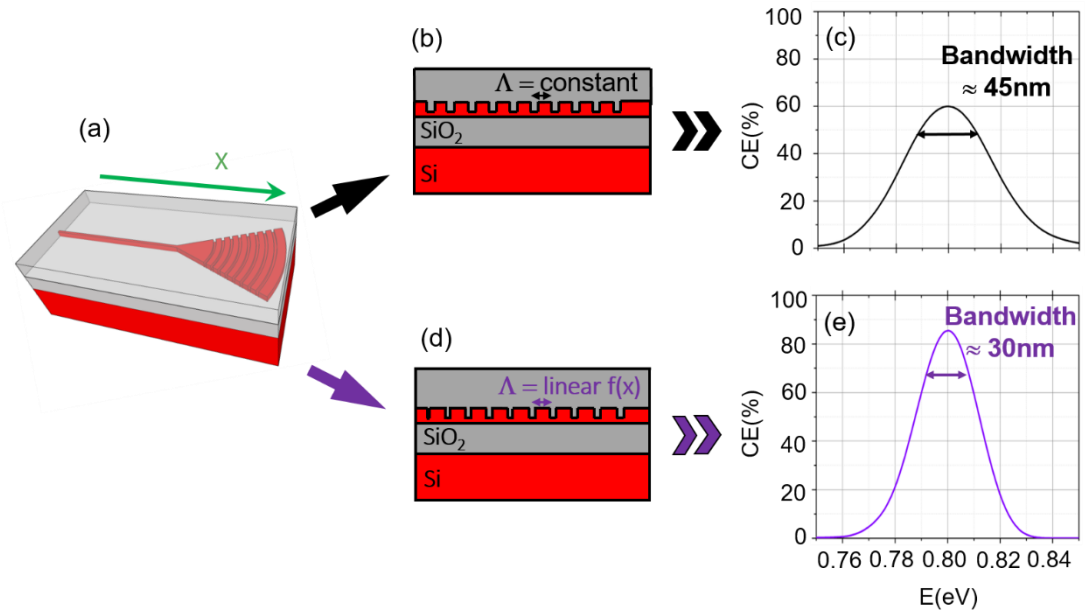

Figure 43: (a) General GC structure on a SOI platform. The GC is developed along the **x**-direction. (b) Cross-section of a uniform-GC and the layers of the SOI wafer. (c) CE curve, evaluated performing the 2D-FDTD simulation of a uniform-GC with a SOI layer thickness of 220nm tuned at E=0.80eV (corresponding to λ_t=1550nm) for an impinging angle of θ_i=10° in the TOX. The 1dB-bandwidth (1dB BW) is equal to 45nm. (d) Cross-section of a non-uniform GC, with a Λ and DC changing linearly along **x**. (d) CE curve of the non-uniform GC with a SOI layer thickness of 290nm tuned at E=0.80eV and designed for a VFb coupling scheme for an equal impinging angle θ_i. The1dB BW is 30nm. The Figure has been taken from [1].

Here, the BW was estimated directly from the CE curve considering the wavelength interval associated with a drop of the 20% from the apex, in analogy with the 1dB definition associated with the 1dB drop from the apex of the IL curve. In addition, the simple and well-known equation $\lambda(nm) = \frac{1240}{E(eV)}$ can be used to convert the energy (E(eV)) into the corresponding wavelength in nm.

Thus, a 1dB BW of 45nm and 30nm was evaluated respectively for the uniform- and non-uniform GC representing a reduction of 15nm, roughly 35% lower, in the amount of wavelengths that can be coupled efficiently by the GC. In addition, the non-uniform GC shows a sharper decay at energies lower than 0.8eV or 1550nm; while, for higher energies the decay assumes a gentler variation.

In this framework, the CE curve can be divided into two separate regions: a red side where the energies are lower respect to 0.8eV and a blue side for higher energy values in analogy with the spectroscopy jargon. The reduction of the 1dB BW and the asymmetry behaviour of the CE curve derive form the non-uniformity of the local pitches, which introduces a band pass filtering effect that filters unequally the energies around 0.8eV. The main challenge behind the study of this filtering effect is

represented by the non-uniformity of the GC structure, which turns into a non-trivial light matter interaction. The FDTD, by simply resolving Maxwell's equation without any further assumption, represents an ideal computational method to investigate the multiwavelength response in details. In particular, two approaches based on this computational method have been proposed: the first one takes advantage of the Spatial Fourier Transform (sFT) of the electromagnetic field emitted by the GC in the near field to give an intuitive insight on the band pass filtering effect and a second one, more rigorous, based on a photonic crystal bandstructure approach.

4.2 Spatial Fourier Transform approach

The sFT can be calculated resorting again to the same out-coupling configuration reported in Figure 34 in order to collect the electric field outside the structure; then performing a Fast Fourier Transform, the relation between the energies and

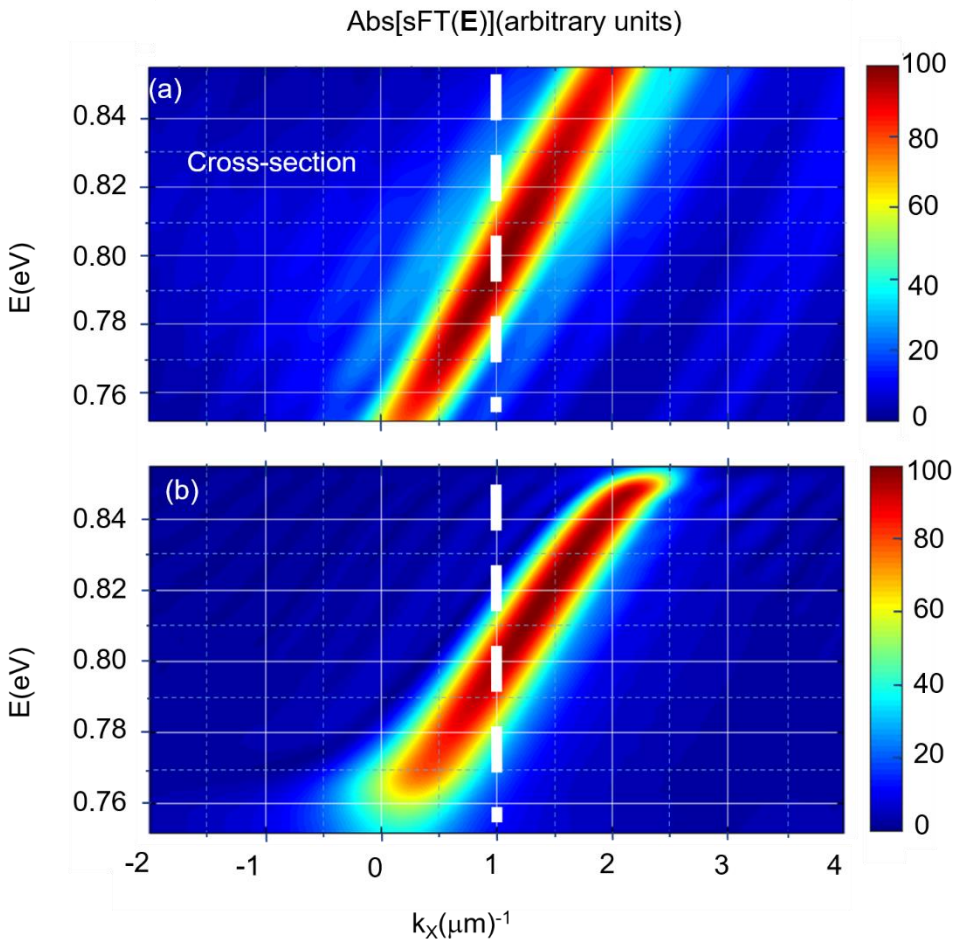

Figure 44*:* (a) Spatial Fourier Transform (sFT) of the electromagnetic field proper of the 220nm-thick uniform-GC as a function of energies E(eV) and the in-plane wavevector k_x calculated exploiting FDTD simulations. (d) sFT of the electromagnetic field related to the 290nm-thick non-uniform GC. The Figure has been taken from [1].

wavevectors k_x out-coupled by the GC can be obtained. Figure 44 panel (a) and (b) reports the sFTs for the uniform- and non-uniform GCs, respectively. The uniform-GC shows a linear relation of the energies and wavevectors with a homogeneous shape across the energy interval with an equal and symmetric broadening of the sFT.

The non-uniform GC, on the contrary, displays two clear "stop-band" regions at the limit of the energy interval, around 0.75eV and 0.85eV where the linear behaviour of the sFT is no longer sustained. Here, the slopes of the curve approach zero defining a clear accessible energy window, as in a filter. Moreover, the broadening of the sFT is not symmetric and homogeneous anymore. In fact, the lower-left region presents a thicker shape, which shrinks moving to the higher energies.

Keeping fixed the k_x value and taking a cross-section of the sFT at this specific value, the corresponding curve is asymmetric showing a different energy filtering around the apex of the sFT. Both the GCs have been tuned to work at E=0.8eV (*i.e.* 1550nm) for an incident angle of 10° that corresponds to an in-plane wavevector component of $k_x = \frac{2\pi}{1.24} E(\text{eV}) \cdot n_{TOX} \cdot \sin(10°) = 1\mu\text{m}^{-1}$, where n_{TOX} is the

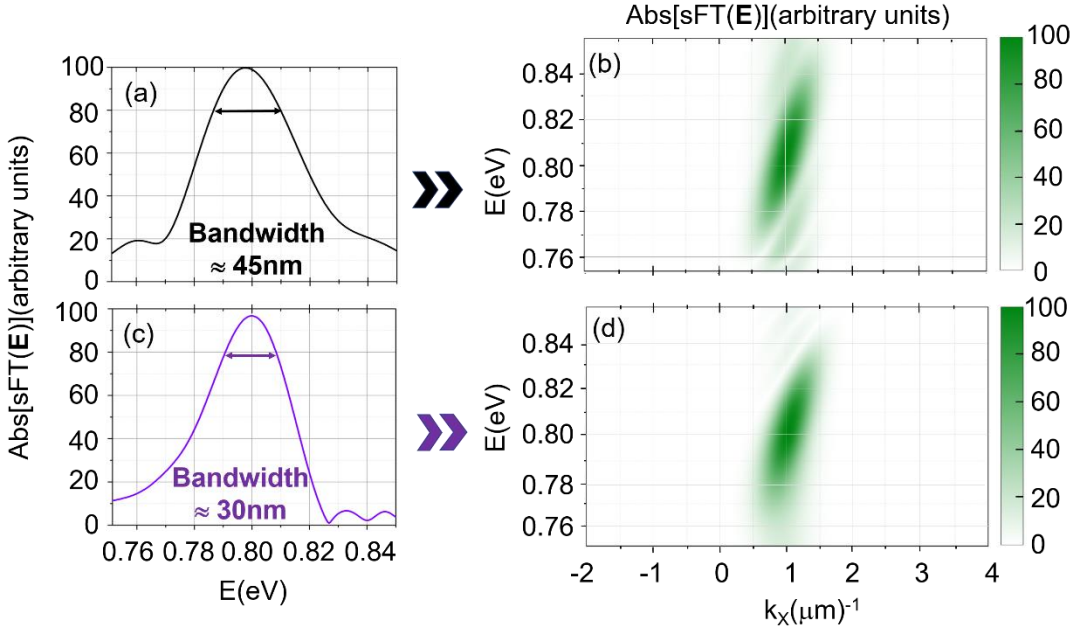

Figure 45: (a) Cross-section of the sFT at k_x=1μm^{-1} related to the energy E=0.80eV and an incident angle θ_i=10°. A 1dB BW=45nm is calculated, in accordance with the value obtained from the CE spectrum. (b) Overlap region between the sFTs associated to the electromagnetic field proper of the uniform-GC emission and the fundamental mode of a vertical SMF. (c) Cross-section of the sFT at k_x=1μm^{-1}. A 1dB BW=30nm is obtained, in accordance with the value calculated from the CE spectrum. (d) Overlap region between the sFTs associated to electromagnetic field proper of the non-uniform GC emission and the fundamental mode of a vertical SMF. The Figure has been taken from [1].

refractive index of the TOX layer, *i.e.* 1.44.

Taking the cross section of panel (a) and (b) at this specific k_x value, the one dimensional sFT can be obtained and the corresponding results are shown in Figure 45 panel (c) and (d).

Considering the spectral width of the sFT, the associated BW can be calculated again, following the same methodology of the CE spectra with a value of 30nm and 45nm for the uniform and non-uniform GCs. Furthermore, form the cross-section it is visible how the asymmetry around the apex affects the sFT of the non-uniform GC showing how the structure sustains better the lower energies, and filtering more selectively the one in the blue side, behaviour in accordance with the CE curves.

The sFT gives the energies and wavevectors sustained by the GCs, however the k_x that are actually coupled can be obtained looking at the overlap sections between the sFTs of the GC and the source, as reported in panels (b) and (d) of Figure 45.

The overlap regions display the same behaviours seen in panel (a) and (b) of Figure 44 with a symmetric and homogenous broadening for the uniform-GC, and an asymmetric and inhomogeneous profile for the non-uniform GC with a characteristic enlargement at lower energies, which can be brought back to the band pass filtering effect.

4.3 Bandstructure-like approach

Figure 46 panel (b) shows the bandstructure for the uniform-GC calculated around the 0.8eV energy region together with the spreading of the source sFT, evaluated in analogy with the CE spreading.

The projection onto the energy axis associated with the overlap between the sFT and the dispersion curve gives the BW limits (*i.e.* the maximum MB and the minimum mB), consequently subtracting MB-mB a BW of 45nm can be calculated.

The situation becomes more complicated for the non-uniform GC, where the structure does not display a periodic behaviour.

Again, the non-uniform GC can be considered as a sequential series of uniform GC junctions and the bandstructures associated to each single pitch can be evaluated.

Panel (c) shows the dispersion curves around 0.8eV for the first, fifth, tenth, and fifteenth pitches in order to cover the whole GC structure that is actually shined by the source mode. Three distinct regions can be identified: the filtered out energies, the

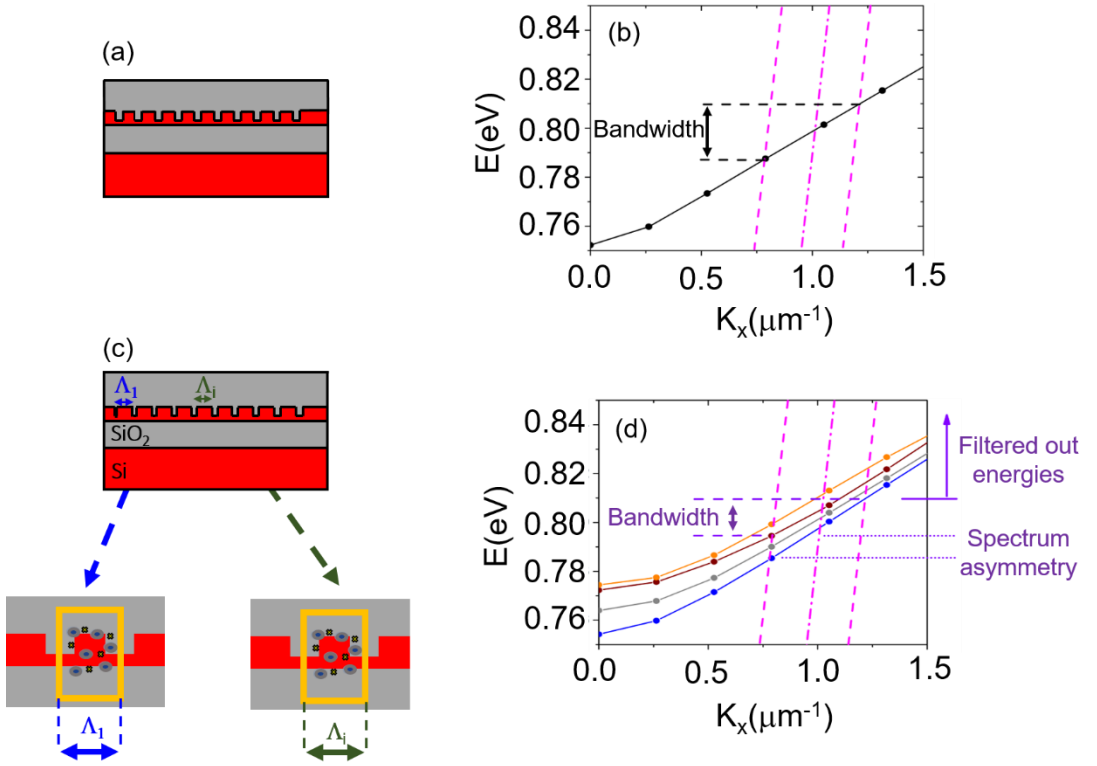

Figure 46: (a) Picture of the uniform-GC, (b) Overlap region between the bandstructure-black line around E=0.80eV and the **k** spreading, in pink lines, related to the incoming light line. The projection of the overlap onto the E(eV) axis gives a 1dB BW=45nm. (c) Bandstructure calculation process for each uniform-GC associated to each local pitch of the non-uniform GC. The two small pictures, under the GC structure, show the differences between the FDTD simulation boxes for two local pitches. (d) Overlap-sections between the bandstructure lines around E=0.80eV and the **k** spreading of the incoming light line for five local pitches: first (blue line), fifth (grey line), tenth (brown line), fifteenth (orange line). Three different energy regions can be found: the filtered out region, the 1dB BW=30nm, and the spectrum asymmetry region. The Figure has been taken from [1].

bandwidth, and the spectrum asymmetry. The MB value can be set as the intersection between the source sFT and the dispersion curve of the first period.

This fix a minimum in the filtered out energies, as the light travelling across the GC is filtered at each step by the various local pitches till the first one.

The region around the tenth tooth can be considered the most important for the scattering process as the one with the highest scattering strength and actually exploited to diffract the "centre of gravity" of the incoming SMF mode. Thus, the intersection between the source sFT and the dispersion curve of the tenth tooth can be identified as the mB point, and consequently the BW can be evaluated as MB-mB=30nm in accordance with the CE curve.

The intersection points below the mB constitutes the spectrum asymmetry region as these energies are allowed to travel inside the GC without being selectively filtered by the structure. Here there is not a single intersection point, as displayed for the MB

case. The first period does not represent a lower limit and all the energies above it can travel towards the WG. Furthermore, the intersection points are not separate anymore by the same energy width, reaching the bandedge, due to the different slopes of the curves. This affects the CE spectrum resulting in a more “gentle” decay at lower energies and in a less selective band pass filtering effect.

Now, taking advantage of the concepts behind the proposed bandstructure investigation, the previous analysis can be extended to the investigation of the multiwavelength response, not only limited to the 1dB BW, of the previously optimized non-uniform GC comparing the outcomes with the computational predictions.

At the same time, the best samples, tested with the HFb coupling scheme, were also measured exploiting a VFb coupling schemes in order to investigate additionally the effect due to a variation in the impinging MFD, and hence a different associated SFTs. These are the key-concepts of the following section.

4.4 Detailed Experimental and Computational analysis of the multiwavelength response of non-uniform GCs for two different MFDs

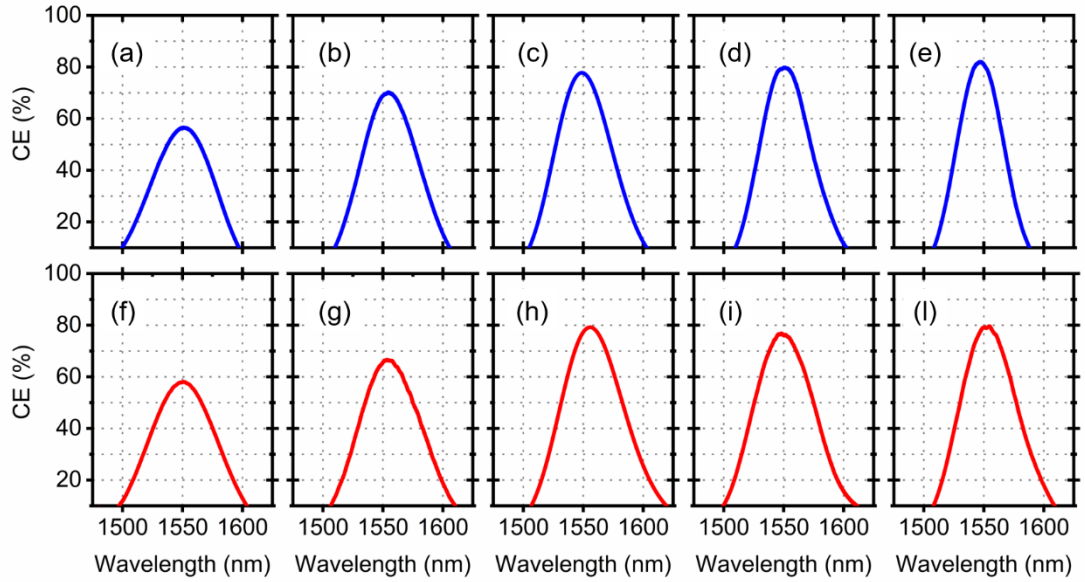

Figure 47: Measured CEs for the best non-uniform GC samples, where the blue curves refer to the HFb coupling scheme, while the red curves refer to the VFb coupling scheme for, respectively: (a), (f) the 220-nm thick SOI; (b), (g) the 260nm-thick SOI; (c), (h) 290nm-thick SOI; (d), (i) 320nm-thick SOI; and (e), (j) 340nm-thick SOI.

The multiwavelength CEs for the best samples were measured through a VFb array following the same procedure already reported previously, and Figure 47 summarizes

the results for each sample for either the HFb coupling scheme, blue curves, and VFb coupling scheme, red curves.

On the other hand, the computational multiwavelength CEs for each GC were calculated performing 2D-FDTD simulations of the VFb coupling scheme. Again, the fibre emission was modelled by reconstructing the VFb inside the software and the guided mode was injected inside the FDTD BOX computing the SMF fundamental mode using the mode source object. In particular, the effect of the material dispersion was neglected on purpose maintaining constant the refractive indexes of the SOI materials in the wavelength range under considerations, *i.e.* n_{Si}=3.48 and n_{SiO2}=1.44, as already done for the HFb. Figure 48, panels (a) and (b), shows a sketch of the two coupling schemes under investigation where the corresponding MFDs are indicated as V-MFD, and H-MFD, for the VFb and HFb respectively.

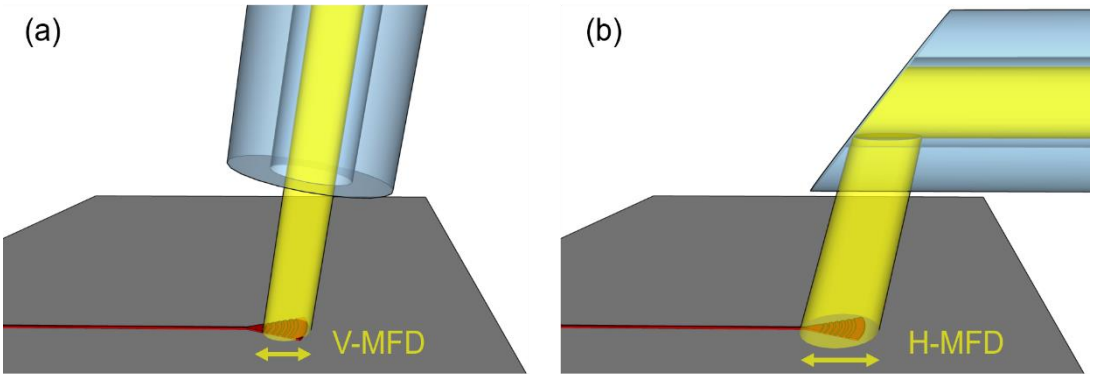

Figure 48: Sketch of the two Coupling schemes under investigation: (a) Vertical-Fiber (VFb) coupling scheme characterized with its Mode Field Diameter (V-MFD), (b) Horizontal Fiber coupling scheme (HFb) with its H-MFD.

The parameter $\eta^{\text{i-th BW}}$, associated to the i-th BW, for each GC design is evaluated performing the Riemann integral over a wavelength interval $\Delta\lambda^{i-th\ BW}=[\lambda_L^{i-th\ BW}, \lambda_R^{i-th\ BW}]$, for either the computational and measured CE curves as stated by the equation below

16

$$\eta^{i-th\ BW} = \int_{\lambda_L^{i-th\ BW}}^{\lambda_R^{i-th\ BW}} CE(\lambda)d\lambda$$

In particular, the $\Delta\lambda^{i-th\ BW}$ are taken spanning from the 1dB BW till the 10dB BW, called for consistency BW number. The $\eta^{\text{i-th BW}}$ parameter allows to take into account, at the same time, both the intensity and the spectral spreading of the CE summarizing the performances of a GC into a single number. Consequently, $\eta^{\text{i-th BW}}$ enables to

compare the multiwavelength CEs not only across different SOI platforms, but also for multiple coupling schemes characterized by different MFDs.

Figure 49 shows the $\eta^{\text{i-th BW}}$ values calculated from the measured CEs, panel (a)-(e), and the corresponding 2D-FDTD results, panel (f)-(j), for either the VFb coupling scheme, dark red and pink bars, and the H-Fb coupling scheme, dark blue and violet bars, for the different BW numbers. The dark blue bar diagrams in panel (a)-(e) display

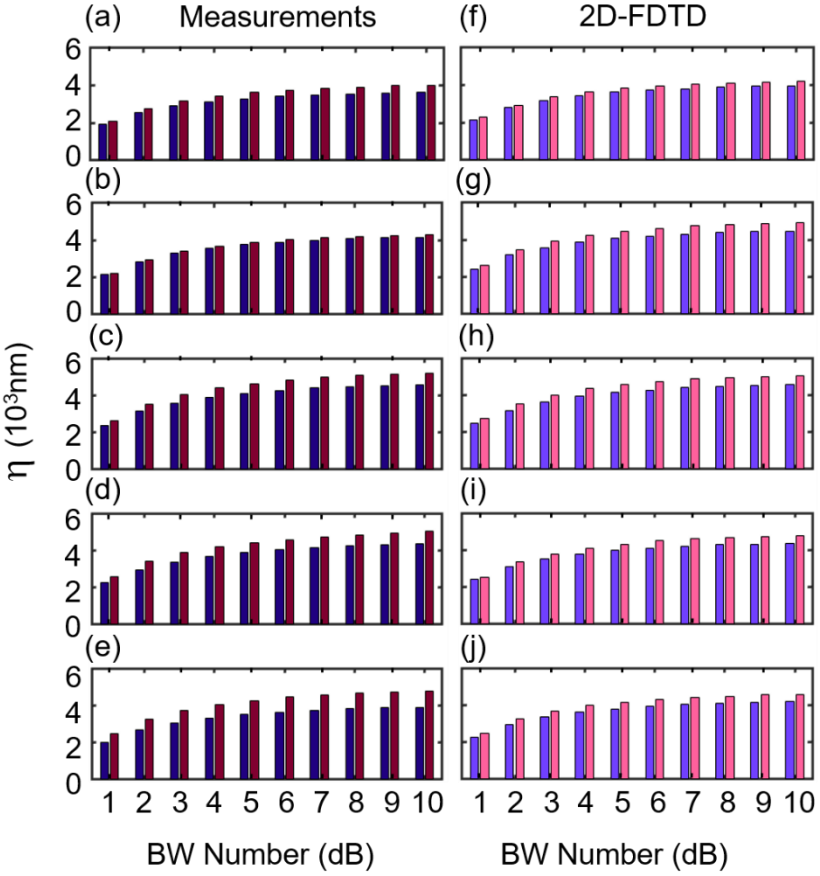

Figure 49: Bar diagrams of the Riemann integral ($\eta^{\text{i-th BW}}$) of the measured and 2D-FDTD CE curves calculated exploiting Eq. 16 for each BW number for either the VFb, dark red and pink bars, and the HFb, dark blue and violet bars, for: (a), (f) the 220nm-thick SOI; (b), (g) 260nm-thick SOI; (c), (h) 290nm-thick SOI; (d), (i) 320nm-thick SOI; (e), (j) 340nm-thick SOI.

increasing values between the 1dB and 10dB BW numbers, as progressively wider $\Delta\lambda^{i-th\ BW}$ intervals are associated to the different BW numbers, leading to greater values of the corresponding Riemann integrals.

In particular, the trend for all the SOI thicknesses is not homogeneous and a faster increment characterized the data between the 1dB and 6dB BW number; while, the $\eta^{i\text{-th BW}}$ values tend to saturate from the 7dB to 10dB BW number, as can be seen from Figure 50 panel (a). Again, this behavior can be expected as a greater portions of the CE curve are considered as directly related to the progressively wider $\Delta\lambda^{i-th\ BW}$ associated to the Riemann integral, which for 10dB accounts already for approximately the 90% of the total area. In addition, form Figure 50 panel (a),

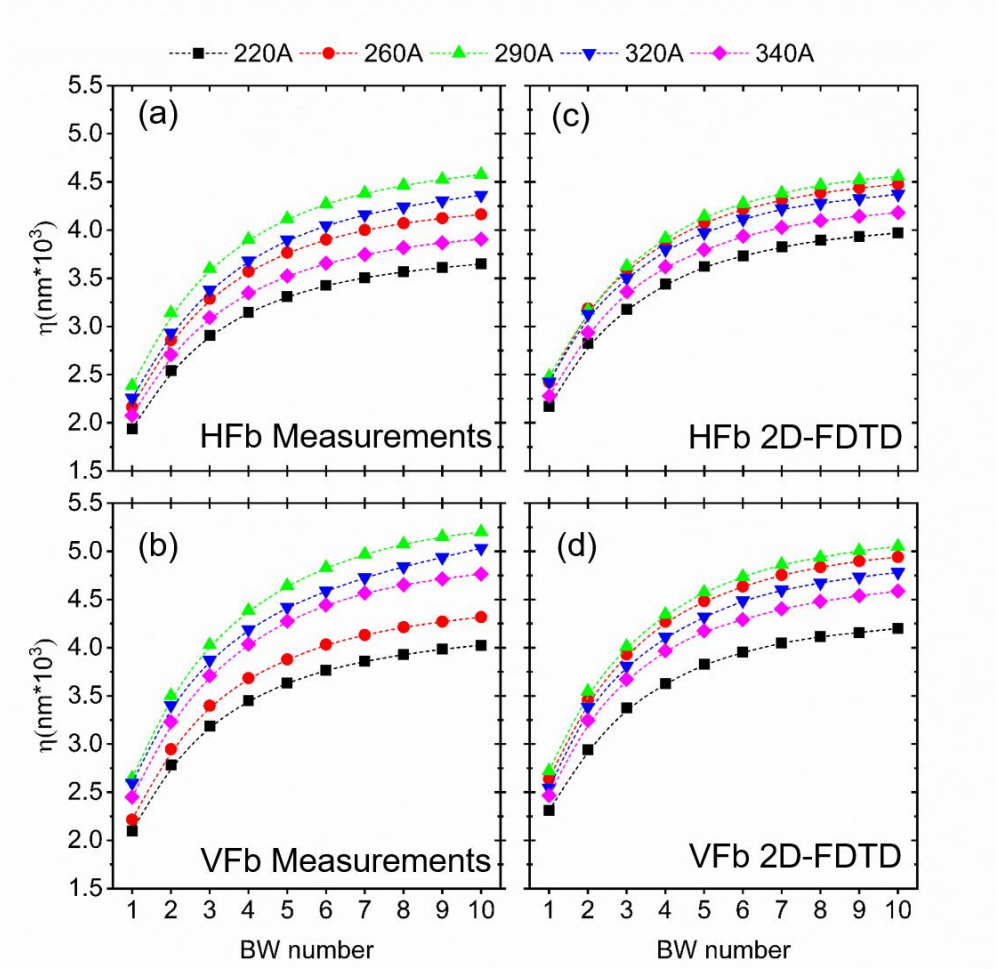

Figure 50: Plot of the Riemann integrals calculated for all the SOI thickness from: (a) the measured CEs for the HFb; (b) the measured CEs for the VFb; (c) the 2D-FDTD CEs for the HFb; (d) the 2D-FDTD CEs for the VFb.

the variation of $\eta^{i\text{-th BW}}$ between the 1dB and 10dB BW number can be estimated as approximately 1712nm for the 220nm-thick SOI, 1999nm for 260nm-thick SOI, 2191nm for 290nm-thick SOI, 2107nm for 320nm-thick SOI, and 1830nm for the 340nm-thick SOI. The 290nm-thick SOI platform displays always the highest values above all followed by the 320nm-thick SOI and 260nm-thick SOI, while the 220nm, and the 340nm platforms show the lowest values. This is not intuitive looking

separately at the CE(λ_t) and the BWs. In fact, while the CE increases with thicker SOI, the BW decreases resulting in a narrowing of the CE curve; thus, the performances grow with the SOI thickness between the 220nm and 290nm platforms, while they decrease between the 290nm and 340nm.

An analogous behavior holds for the VFb coupling scheme as well, as it can be seen form the dark red bars of Figure 49, and Figure 50 panel (b). In this case, the variation between the 1dB and 10dB BW number are 1928nm for the 220nm-thick SOI, 2102nm for the 260nm-thick SOI, 2557nm for the 290nm-thick SOI, 2437nm for the 320nm-thick SOI, and 2317nm for the 340nm-thick SOI. Again, the 290nm-thick SOI is found the most performant.

From Figure 49 panels (a)-(e), the VFb coupling schemes displays values of $\eta^{\text{i-th BW}}$ always greater with respect to the HFb coupling scheme for each SOI platform.

Being the GC under the fibres the same, the MFD is the only parameter that changes between the two coupling schemes. As a consequence, the tinier V-MFD enables to obtain wider $\Delta\lambda^{i-th\ BW}$, respect to the H-MFD, behavior in analogy with the work of Passoni *et. al* [2] and the MFD dependence of the analytic formula for the 1dB BW reported in [3].

In fact, the smaller dimension of the V-MFD in real space turns into an intrinsically wider sFT in the momentum-space, with respect to the sFT of the HFb, and therefore, due to the finite dimension of the GC, more **k**-components can satisfy at the same time the Bragg law resulting in greater $\Delta\lambda^{i-th\ BW}$, and hence higher $\eta^{\text{i-th BW}}$.

Figure 49 panel (f)-(j) show the values calculated from the 2D-FDTD multiwavelength CEs for each SOI thickness and for either coupling schemes. In particular, the data increase across the BW number with a similar behaviour to the measured counterpart, as it can be seen form Figure 50 panel (c) and (d). Here, the computational difference of $\eta^{\text{i-th BW}}$ between the 1dB and 10dB BW numbers for the HFb is 1803nm for the 220 nm-thick SOI, 2055nm for the 260 nm-thick SOI, 2078nm for the 290nm-thick SOI, 1949nm for the 320nm-thick SOI, and 1903nm for the 340nm-thick SOI. The 290nm-thick SOI is confirmed as the most perfomant platform, followed by the 260nm- and 320nm-thick SOI, while the 220nm and 340nm platforms display again the lowest values.

For the VFb, the same difference becomes 1890nm for the 220nm-thick SOI, 2304nm for the 260nm-thick SOI, 2331nm for the 290nm-thick SOI, 2240nm for the

320nm-thick SOI, and 2122nm for the 340nm-thick SOI. Finally, the computational $\eta^{\text{i-th BW}}$ values for the VFb are always higher with respect to the HFb counterparts for each SOI thickness.

Overall, the computational behaviours for each SOI thickness and for both coupling schemes are in accordance with the measurement counterparts.

Thanks to the previous results, the consistency of our FDTD models in describing the whole light-coupling schemes from the fibres emission to the diffraction processes of each non-uniform GC is verified.

However, the multiwavelength response of these non-uniform GCs is relatively complex and a finer analysis of $\eta^{\text{i-th BW}}$ can be undertaken to explore the filtering features.

Now, the Riemann integral described in Eq. 16 can be revaluated considering the two contributes derived from $\lambda_L^{\text{i-th BW}} < \lambda_t$ and $\lambda_R^{\text{i-th BW}} > \lambda_t$ defined through the equations below

17

$$\eta_L^{i-th\ BW} = \int_{\lambda_L^{i-th\ BW}}^{\lambda_t} CE(\lambda)d\lambda$$

and

18

$$\eta_R^{i-th\ BW} = \int_{\lambda_t}^{\lambda_R^{i-th\ BW}} CE(\lambda)d\lambda$$

in order to weight the two numbers and define the effect on the total $\eta^{\text{i-th BW}}$ showing the asymmetry in $\Delta\lambda_L^{i-th\ BW}$ respect to λ_t, *i.e.* $\Delta\lambda_L^{i-th\ BW} = \lambda_t - \lambda_L^{\text{i-th BW}} \neq \Delta\lambda_R^{i-th\ BW} = \lambda_R^{\text{i-th BW}} - \lambda_t$. A visual representation of the Riemann integral related to the Eq. 17 and 18 is shown in Figure 51 for clarity purposes.

Intuitively, the asymmetry respect to λ_t of the CE profile is already visible looking at the curves shown in Figure 47.

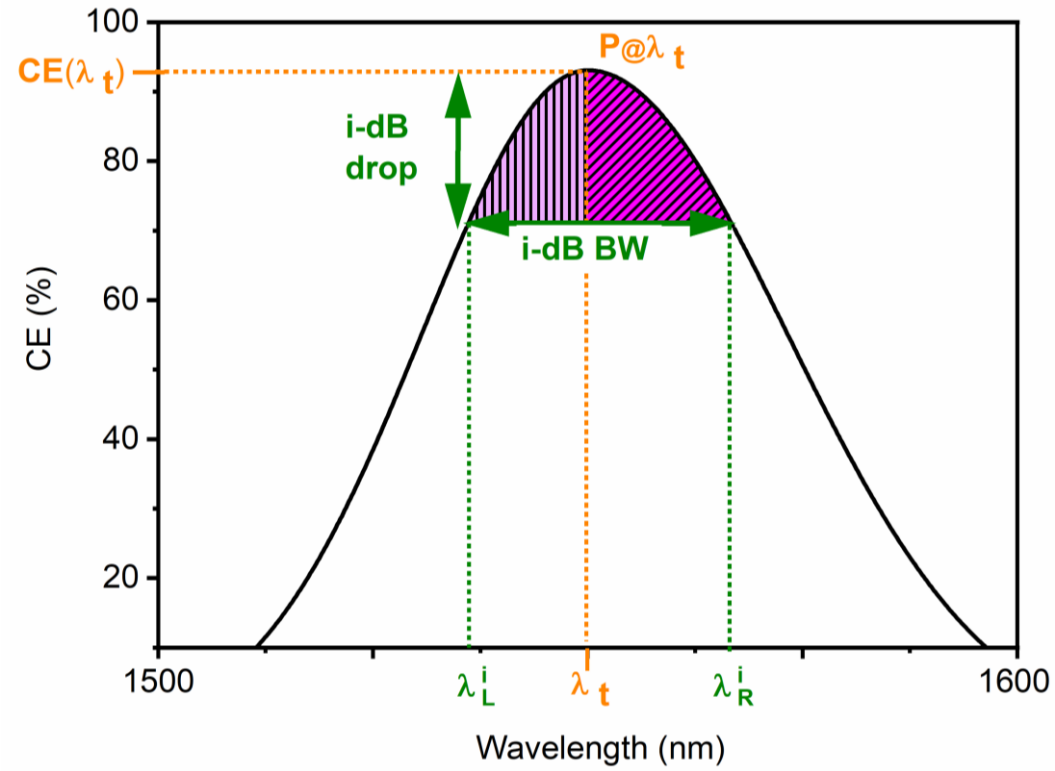

Figure 51: Visual sketch of the Riemann integrals evaluated through the Eq. 17 and 18. The left contribute ($\eta_L^{i-th\ BW}$) is pointed out for a generic i-th BW number by the light violet shaded area with vertical lines, while the right contribute ($\eta_R^{i-th\ BW}$) is indicated by the dark violet shaded area with oblique lines. The peak of the curve is called P@λ_t.

Figure 53 shows the two weights calculated for all the SOI thicknesses and for both coupling schemes; in particular: panels (a)-(e) display $\eta_L^{i-th\ BW}$ (brighter blue bars) and $\eta_R^{i-th\ BW}$ (darker blue bars) related to the measurements referred to the HFb coupling scheme; panels (f)-(j) display the $\eta_L^{i-th\ BW}$ (brighter light-blue bars) and $\eta_R^{i-th\ BW}$ (darker light-blue bars) calculated through the 2D-FDTD model related to the HFb coupling scheme; panels (k)-(o) show the $\eta_L^{i-th\ BW}$ (brighter red bars) and $\eta_R^{i-th\ BW}$ (darker red bars) for the measurements performed exploiting the VFb coupling scheme; and panel (p)-(t) report the $\eta_L^{i-th\ BW}$ (brighter orange bars) and $\eta_R^{i-th\ BW}$ (darker orange bars) calculated running the corresponding 2D-FDTD simulations with the VFb coupling scheme.

Figure 53 panels (a)-(e) show the bar diagrams related to the overall variation of the measured $\eta_L^{i-th\ BW}$. The values increase across the BW number for all the SOIs; in particular, the growth of their intensities tends to saturate moving towards the 10dB BW number. Again, this behavior is expected for the same aforementioned reason reported for the $\eta^{\text{i-th BW}}$.

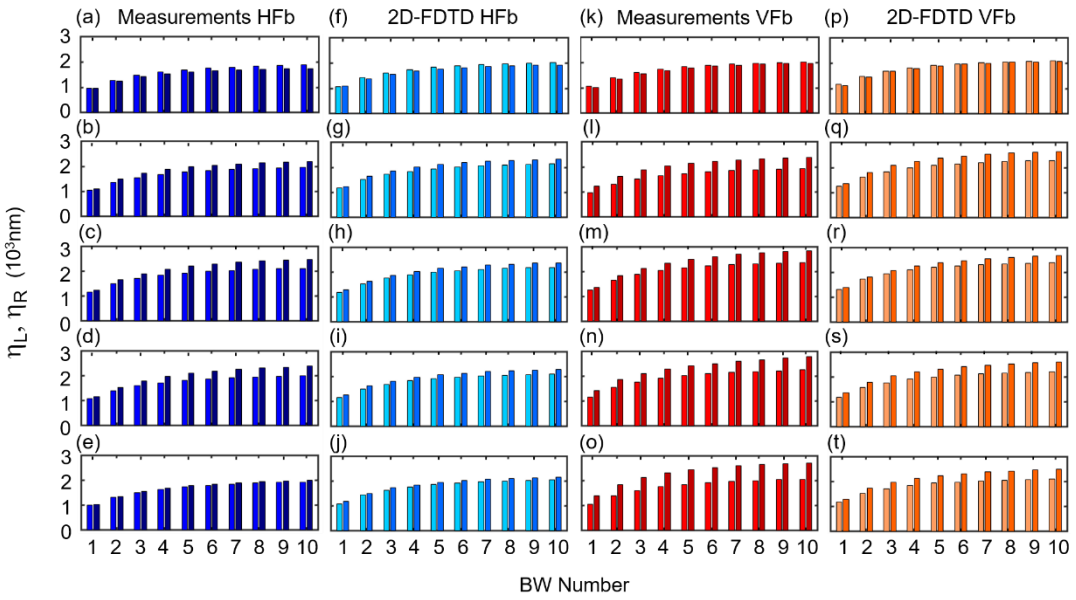

Figure 53: η_L and η_R contributes evaluated for each SOI thickness and both coupling schemes: panels (a)-(e) and (f)-(j) show the two contributes for the HFb coupling scheme for the measurements and the 2D-FDTD results respectively. The lighter blue shades represent the η_L values and the darker blue one refer to the η_R for: (a), (f) the 220nm-thick SOI; (b), (g) the 260nm-thick SOI; (c), (h) the 290nm-thick SOI; (d), (i) the 320nm-thick SOI; (e), (j) the 340nm-thick SOI. Panels (k)-(o) and (p)-(t) display the η_L and η_R for the VFb coupling scheme for the measurements and the 2D-FDTD results, respectively. The lighter red and orange shades refer to η_L and the darker red and orange one to the η_R for: (k), (p) the 220nm-thick SOI; (l), (q) the 260nm-thick SOI; (m), (r) the 290nm-thick SOI; (n), (s) the 320nm-thick SOI; (o), (t) the 340nm-thick SOI.

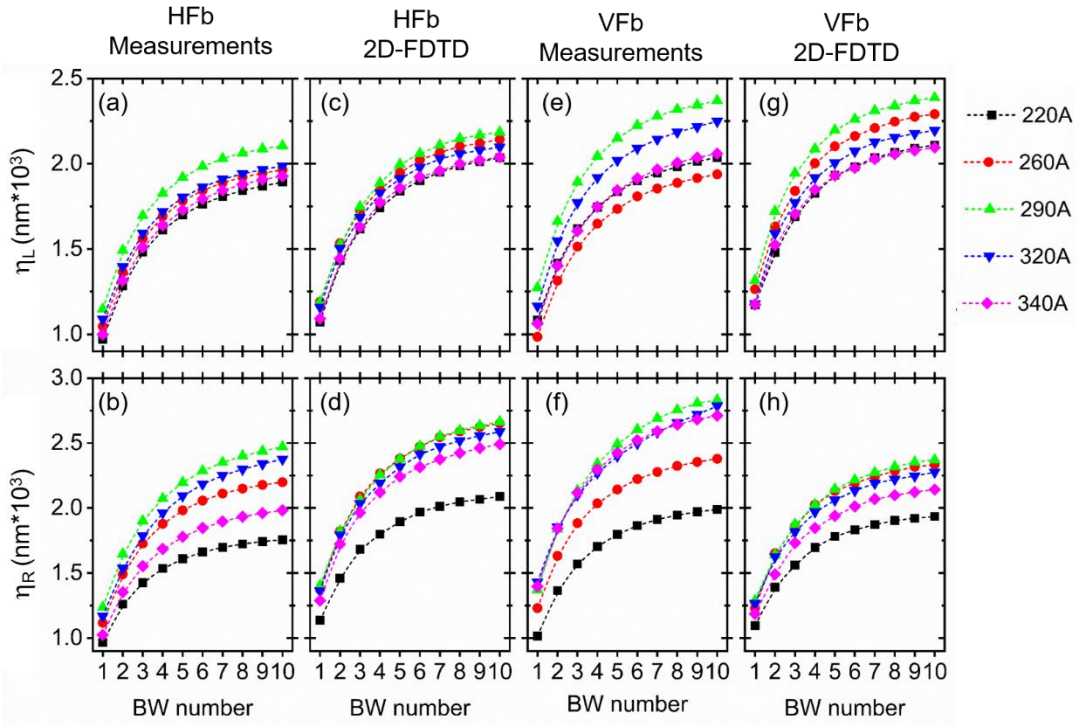

Figure 52: η_L and η_R contributes evaluated for each SOI thickness and both coupling schemes for: (a), (b) experimental data for the HFb coupling scheme; (c), (d) computational data for the HFb coupling scheme; (e), (f) experimental results for the VFb coupling scheme; (g), (h) computational results for the VFb coupling scheme.

In particular, while the 220nm-thick SOI shows the lowest $\eta_L^{i-th\ BW}$ values, the 290nm-thick SOI displays the highest, with a trend of $\eta_L^{i-th\ BW}$ across the platforms that grows between the 220nm- and 290nm-thick SOI and then, decreases between the 290nm- and 340nm-thick SOI, as it can be seen from the corresponding curves reported in Figure 52 panel (a).

Similarly, the overall variation of the measured $\eta_R^{i-th\ BW}$ rises across the BW number for all the SOI thicknesses, showing a behavior analogous to the left counterpart with the 220nm platform displaying the lowest data across all the other SOIs. The 290nm-thick SOI shows the highest with a trend across the different platforms that again grows between the 220nm- and 290nm-thick SOI and then drops, as reported in Figure 52 panel (b).

The overall variation of the computational $\eta_L^{i-th\ BW}$ increases across the BW number for all the SOI thicknesses, as shown in Figure 53 panels (f)-(j), with a behavior similar to the experimental counterpart. Again, the 220nm-thick SOI displays the lowest values of $\eta_L^{i-th\ BW}$ followed by the 340nm-, 320nm-, 260nm-, and 290nm-thick SOI, which displays the greatest values, as reported in Figure 52 panel (c). On the other hand from Figure 53 panel (f)-(j), the overall variation of the computational $\eta_R^{i-th\ BW}$ increases across the BW number for all the SOI thicknesses in a similar manner as done by the experimental counterparts. Also in this case, the 220nm-thick SOI shows the lowest values, while the 290nm-thick SOI the highest one with a trend across the platforms in agreement with the one displayed by the experimental results, see Figure 52 panel (d).

For the VFb coupling scheme, panels (k)-(o) of Figure 53, the overall variation of the measured $\eta_L^{i-th\ BW}$ grows across the BW number for all the SOI thicknesses with a trend of their intensities that tends to saturate moving towards the 10dB BW. Here, the 260nm-thick SOI displays the lowest values followed by the 220nm-, 340nm-, 320nm- and 290nm-thick SOI, which again shows the highest numbers, see panel (e) of Figure 52.

From Figure 53 panel (k)-(o), the measured $\eta_R^{i-th\ BW}$ for the VFb coupling scheme increases across the BW number for each SOI thickness. The lowest numbers are exhibited by the 220nm-thick SOI followed by the 260nm, then the 320nm and 340nm

platforms, with close values, and the 290nm-thick SOI, which is confirmed again the highest one, see Figure 52 panel (f).

On the other hand, from Figure 53 panel (p)-(t), the overall variation of the computational $\eta_L^{i-th\,BW}$ grows across the BW number for all the SOI thicknesses, in accordance with the measurements, and the 220nm-thick SOI, together with the 340nm-thick SOI, displays the lowest $\eta_L^{i-th\,BW}$ intensities, followed by the 260nm- and 320nm-thick platforms; while the 290nm shows the highest values above all, see Figure 52 panel (g). In particular, the trend across the SOIs shows an increment between the 220nm and 290nm platforms and a decreasing between the 290nm- and the 340nm-thick SOI.

The $\eta_R^{i-th\,BW}$ values displays a similar behavior to $\eta_L^{i-th\,BW}$ across the BW number, see Figure 53 panel (p)-(t), where the 220nm-thick shows the lowest numbers followed by the 340nm-, 320nm-, 260nm-, and 290nm-thick SOI, with an increasing trend between the 220nm- and 290nm-thick SOI and a consequent decreasing, see Figure 52 panel (h).

From the analysis of either Figure 53 and Figure 52, a good agreement between the computational and experimental frameworks holds for the two weights displaying a similar growth and ranges of values.

In particular, both the experimental and the computational right weights are always greater that the left counterparts for all the SOI thicknesses, with the only exception of the 220nm SOI, behavior seen for both the HFb and the VFb, and supported by the computational data as well.

This outcome is interesting and fundamental since the dispersion of the material have been neglected on purpose in the simulations, suggesting that the nature of such asymmetry depends, almost entirely, on the actual non-uniform pattern of each GC, in agreement with the predictions of [1].

The previous analysis is fundamental to demonstrate the asymmetry of the $\Delta\lambda^{i-th\,BW}$ as it enables to simultaneously compare the left and right weight intensities, displaying the presence of a different contribution to $\eta^{\text{i-th BW}}$.

Now, the effect due to $\eta_L^{i-th\,BW}$ and $\eta_R^{i-th\,BW}$, on the redistribution of the coupled energy inside the spectral intervals $\Delta\lambda_L^{i-th\,BW}$ and $\Delta\lambda_R^{i-th\,BW}$ and across the BW number can be studied taking advantage of their ratio showing explicitly the asymmetry in $\Delta\lambda^{i-th\,BW}$.

Figure 54 panel (a)-(e) show the ratio calculated for the experimental values for either the HFb (dark-blue square points) and VFb (dark-red dots) for each SOI thickness from the 220nm platform, panel (a), to the 340nm platform, panel (e).

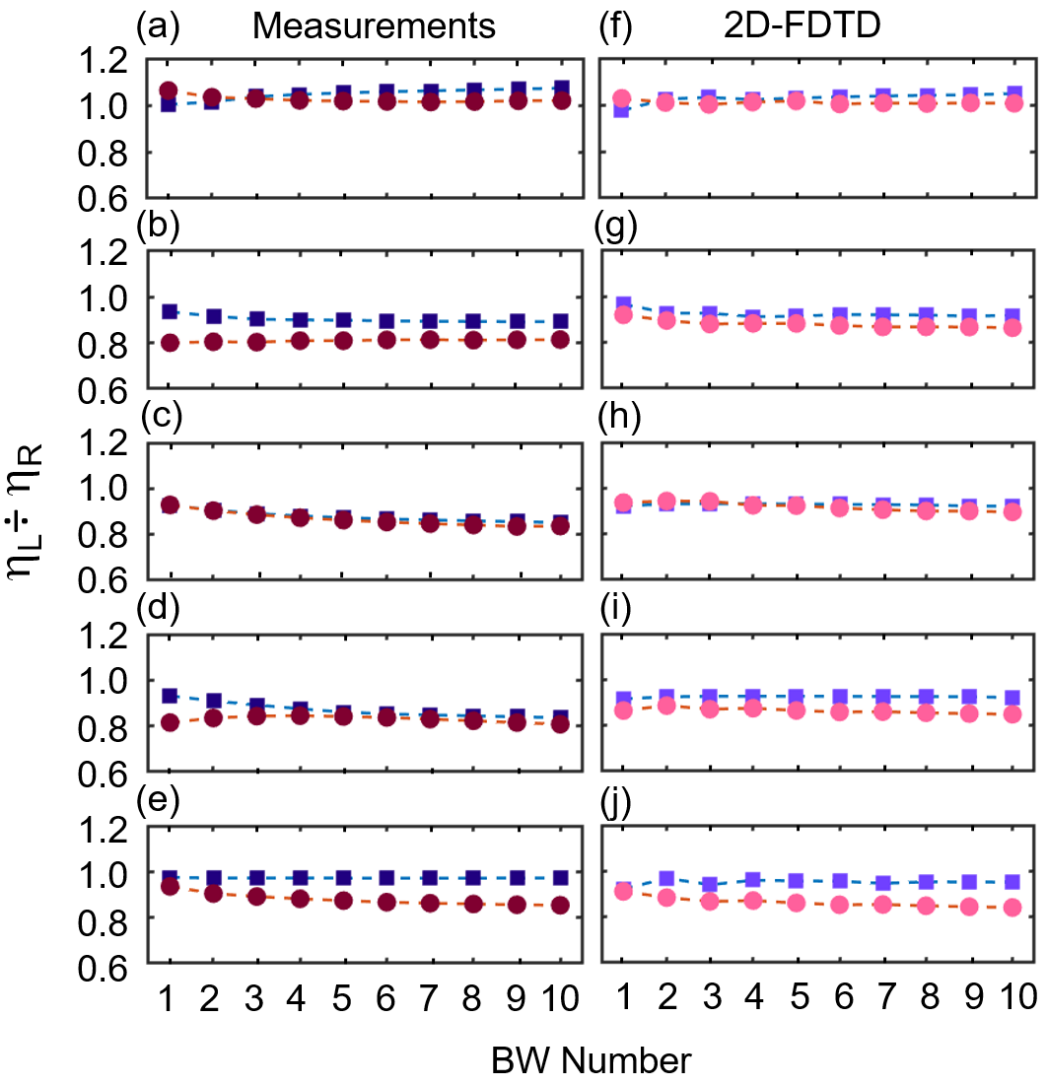

Figure 54: Behaviour of the ratio $\frac{\eta_L^{\text{i-th BW}}}{\eta_R^{\text{i-th BW}}}$ across the BW number for: (a), (f) the 220nm-thick SOI; (b), (g) 260nm-thick SOI; (c), (h) 290nm-thick SOI; (d), (i) 320nm-thick SOI; (e), (j) 340nm-thick SOI. The left panels refer to the experimental results, while the right panel to the computational outcomes. The dark-blue and violet curves (square points) refer to the HFb coupling scheme, while the dark-red and pink curves (dot points) to the VFb coupling schemes.

First, the behaviors of both the HFb and VFb curves for each SOI is investigated. The 220nm-thick SOI shows growing values of the ratio across the BW number for the HFb data, while the results related to the VFb slightly decrease moving towards the 10dB BW number displaying an interchange between the two curves approximately about the 3dB BW number. On the other hand, the 260nm-thick SOI shows a reduction of the ratio values for the HFb across the BW number, while a flat

behavior can be seen from the VFb data. However, the two curves remain separate without showing any interchange. The 290nm-thick SOI displays a decreasing of the ratio for either the HFb and VFb with a similar behavior across the BW number, with data that almost overlap on top of each other; while the 320nm-thick SOI shows a decreasing of the ratio related to the HFb for progressively higher BW numbers, and an almost flat behavior for the VFb data. In particular, the values of the two curves nearly overlap moving towards higher BW numbers. On the contrary, the 340nm platform shows results between the HFb and VFb close to each other at the beginning of the two curves. However, while the HFb data remain constant across the BW number, the ratio values of the VFb decreases resulting in an increment of the gap between the HFb and VFb data.

Now, the attention can be focused on the comparison between the different SOI platforms to look at the major differences in the behavior of the data across the BW number for both the coupling schemes. In particular, the 220nm-thick SOI is the only platform that shows values of the ratio greater than 1. This suggests that the resulting redistribution in $\eta^{\text{i-th BW}}$ of the coupled energy is always in favour of the left weight, with consequently higher perfomances of the spectral intervals $\Delta\lambda_L^{i-th\ BW}$ with respect to the $\Delta\lambda_R^{i-th\ BW}$ for either the HFb and VFb coupling schemes.

In contrast, the remaining SOIs have a redistribution of the coupled energy always in favour of the right weight guaranteeing higher performances related to the $\Delta\lambda_R^{i-th\ BW}$ intervals. Here, while the 290nm-thick SOI shows a redistribution that progressively shifts the weight on the right contribute moving across the BW number for both the VFb and HFb approaching a ratio value of 0.8; the 260nm- and 320nm-thick SOI have a behavior analogous to the 290nm-thick SOI only for the HFb, while the flatness of the VFb data suggests no redistribution in energy across the BW number between the two weights, with values around 0.8. On the contrary, the redistribution in energy for the 340nm-thick SOI displays a gradually shift of the weight in favour of the right contribute, which becomes predominant moving towards the 10dB BW number for the VFb. Regarding the HFb, the flat behavior of the curve suggests no redistribution, in particular with almost comparable numbers between the two weights since the ratio shows values in proximity of 1 across the BW numbers.

Figure 54, panel (f)-(j), displays the values of the ratio calculated from the 2D-FDTD results for the HFb (violet square point) and VFb (pink dots) from the 220nm

platform, panel (f), to the 340nm platform, panel (j). Overall, the behaviours of the computational curves for each SOI are in good agreement with the experimental counterparts displaying a variation of the data across the BW number inside the same range of values. In particular, the 220nm-thick SOI shows a growth of the values moving towards the 10dB BW number, and an almost flat behavior for the VFb, resulting in an interchange between the two curves. The 260nm SOI displays a decreasing behavior for both the HFb and VFb curves at the beginning of the curve that flattens moving towards the 10dB BW number without any interchange between them. The 290nm-thick SOI displays a similar behavior for the HFb and VFb curves across the BW number, which almost overlap one on top of each other; while the 320nm-thick SOI shows an almost flat behaviour for either the VFb and HFb curves across the BW number. The 340nm-thick SOI shows values of the ratio between the HFb and VFb in proximity of each other at the beginning of the curves, but while the HFb data display a flat behaviour across the BW number, the values for the VFb decrease across the BW number. Again, also from the computational outcomes, the 220nm-thick SOI is the only one having values greater than 1 resulting in a redistribution of the coupled energy in favour of the left weight. On the contrary, all the other SOIs show an opposite behavior with data always smaller than 1, resulting in a predominance of the right weight on the left counterpart supporting the experimental outcomes.

Maintaining fixed the MFD, Figure 54 shows different behaviours across the SOI platforms analogous in both the experimental and computational outcomes, even though the dispersion of the material has been neglected. This suggests that the redistribution of the coupled energies depends on the specific non-uniform GC structure, which affects the propagation of the light across its local pitches. This is a consequence due to the varying impedance matching, as already seen from the computational analysis of the effective refractive index shown in Figure 36.

On the other hand, for a fixed non-uniform GC design, the variation of the data differs between the V-MFD and the H-MFD as a result of the different width related to the corresponding sFTs. This results in a different number of available **k**-components to be coupled.

Therefore, to capture the whole physics behind the multiwavelength response of such non-uniform structures, either the MFD dimension and the specific non-uniform GC pattern must be considered at the same time.

In particular, the redistribution between $\eta_L^{i-th\ BW}$ and $\eta_R^{i-th\ BW}$ weights affects the corresponding width of the $\Delta\lambda_L^{i-th\ BW}$ and $\Delta\lambda_R^{i-th\ BW}$ spectral intervals. In fact, the higher the left or right weight, the greater the width of the associated spectral interval with respect to the other.

An easy geometrical demonstration regarding the Riemann integrals of Eq. 17 and 18 can be taken into account to understand the aforementioned statement. The left and right weights are calculated inside the $\Delta\lambda_L^{i-th\ BW}$ and $\Delta\lambda_R^{i-th\ BW}$ spectral intervals and the corresponding CE(λ) values evaluated at $\lambda_L^{i-th\ BW}$ and $\lambda_R^{i-th\ BW}$, *i.e.* namely CE($\lambda_L^{i-th\ BW}$), and CE($\lambda_R^{i-th\ BW}$), are the same by definition. Thus, it can be stated that the equality CE(λ_t)-CE($\lambda_L^{i-th\ BW}$) = CE($\lambda_R^{i-th\ BW}$)-CE(λ_t) is always true for each i-th BW number. Therefore, a greater $\eta_L^{i-th\ BW}$ or $\eta_R^{i-th\ BW}$ turns into a larger area under the CE curves, condition that can be fulfilled only if $\Delta\lambda_L^{i-th\ BW}$ is wider than $\Delta\lambda_R^{i-th\ BW}$, or vice versa.

Finally, this inequality demonstrates the asymmetry of $\Delta\lambda^{i-th\ BW}$around the λ_t, affecting the shape of the CE. Incidentally, the asymmetry related to either the measurements and the computational results, proper of the 1dB BW number and for the 290nm-thick SOI, is in agreement with the one reported in [1].

To summarize, the study of Figure 53 and Figure 52 allowed to demonstrate that there is a difference in the coupled energies between the $\Delta\lambda_L^{i-th\ BW}$ and $\Delta\lambda_R^{i-th\ BW}$, which affects the $\eta_L^{i-th\ BW}$ and $\eta_R^{i-th\ BW}$ values, leading to an asymmetry of the $\Delta\lambda^{i-th\ BW}$. This asymmetry can be quantified exploiting the ratio $\eta_L^{i-th\ BW} \div \eta_R^{i-th\ BW}$ and interpreted in terms of a filtering-effect, which affects the coupling process related to the energies at different wavelengths, around λ_t, displaying a different selectivity depending on the spectral intervals $\Delta\lambda_L^{i-th\ BW}$ and $\Delta\lambda_R^{i-th\ BW}$. Hence, this selectivity has an important role in determining the shape of the multiwavelength CE and, consequently, the final BW values. In particular, the filtering effect comes from the optical impedance matching established by the variation of effective refractive index (n_{eff}), which is a consequence of the apodization of the non-uniform GC designed through the Bragg's law.

Indeed, the n_{eff} and its variation are a consequence of either the specific materials of the SOI platform, through the material dispersion, and the metastructure through the design of the non-uniform GC pattern.

In this framework, the main scope of the previous Chapter 3 was related to the optimization of the metastructure. Thus, the combination of the material and the pattern dispersions was discriminated in order to show that the behavior of the BW can be tailored through the GC pattern.

Following the spirit of the analysis proposed in [1], the BW of each GC design was calculated at each BW number and for either MFDs: (i) directly from the CE curves (either measured and simulated), and (ii) exploiting the reciprocal space analysis performing the overlap between the dispersion curves E(**k**) calculated for each GC and the sFTs of the Gaussian modes associated to both the VFb and HFb.

Demonstrating the agreement of the reciprocal space analysis predictions with the BW evaluated from the CE curves allows to show that the BW behavior depends from the pattern dispersion, and together with the MFD, determines the multiwavelength response of such non-uniform designs. Figure 55 shows the calculation procedure of the 1dB BW exploiting the reciprocal space analysis. First, the dispersion curves E(**k**) associated to the local pitches of every non-uniform GC designs where calculated exploiting the FDTD method. The non-uniform GC is treated as locally made of

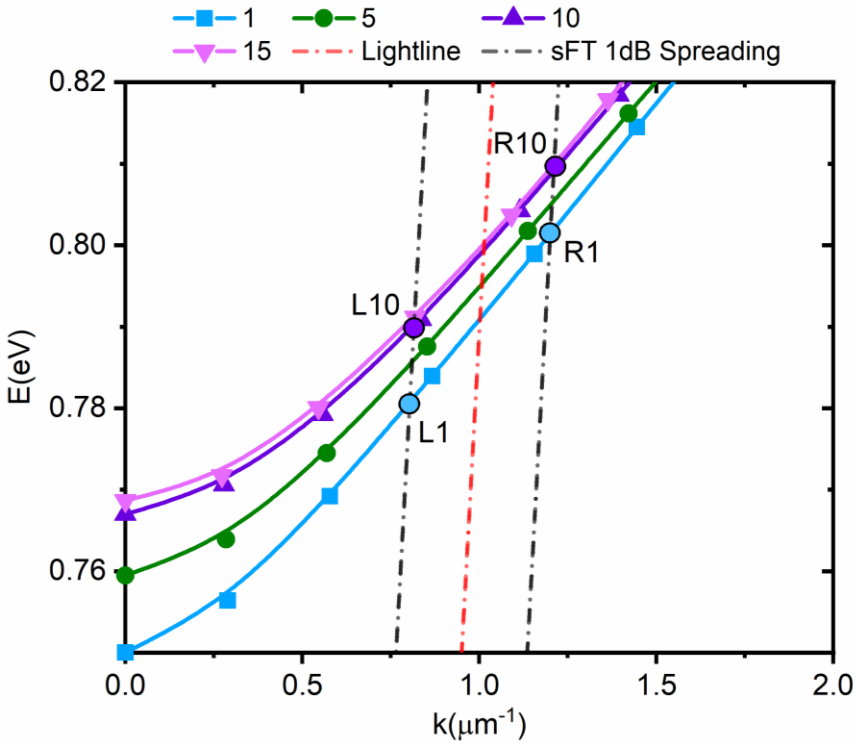

Figure 55: Overlap of the 1dB spreading of the Spatial Fourier Transform (sFT) associated to a certain MFD and the E(k) dispersion curves, i.e. bandstrcutures calculated through 2D-FDTD simulations, of the first, fifth, tenth, and fiftieth teeth of a generic non-uniform GC. The overlap points are indicated as L1 and R1 for the first tooth and L10 and R10 for the tenth. The lightline associated to the incoming beam is also reported for sake of completeness.

uniform-GCs with their own local pitches (Λ_i) and duty-cycles, where i is the index that runs over the GC pitches.

Then, the resonance condition between the E(**k**) curves and the fibre emission is evaluated performing the overlap between the bandstructures related to each local uniform-GC and the **k**-spreading associated to the 1dB drop from the sFT peak of the VFb and HFb Gaussian beams, characterized by its own V-MFD or H-MFD. In this context, the overlap of the sFTs with the E(**k**) curves proper of the 1st and 10th local pitches are take into consideration, for the same reasons explained in section 4.3, resulting in four separate points: L1, L10, R1, and R10, as shown in Figure 55.

Eventually, the 1dB BW, in nanometres, is evaluated taking into account separately the left and right contribute, with respect to the λ_t, performing the arithmetic mean of the 1st and 10th local pitches, as displayed by the following equation 19

$$1\text{dB BW} = 620eV \cdot nm \left(\frac{1}{E_{R1}} + \frac{1}{E_{R10}} - \frac{1}{E_{L1}} - \frac{1}{E_{L10}} \right)$$

The same procedure is applied for the other BW number where the overlap is now calculated considering a **k**-spreading associated to the corresponding dB drop form the sFT peak of the VFb and HFb.

Figure 56 panel (a)-(e) shows the BW for the HFb calculated from the measured and computational CE curves (blue dot and violet asterisk, respectively) and from the reciprocal space analysis (green triangle) from the 220nm-thick SOI, panel (a), to the 340nm-thick SOI, panel (e). Panel (f)-(j) show the corresponding results for the VFb calculated directly from the measured and simulated CE curves (red dot and pink asterisk, respectively) and from the reciprocal space analysis (green triangle).

The BW values increases monotonically with the BW number of approximately an order of magnitude for both the HFb and VFb, and for all the GC designs. A good

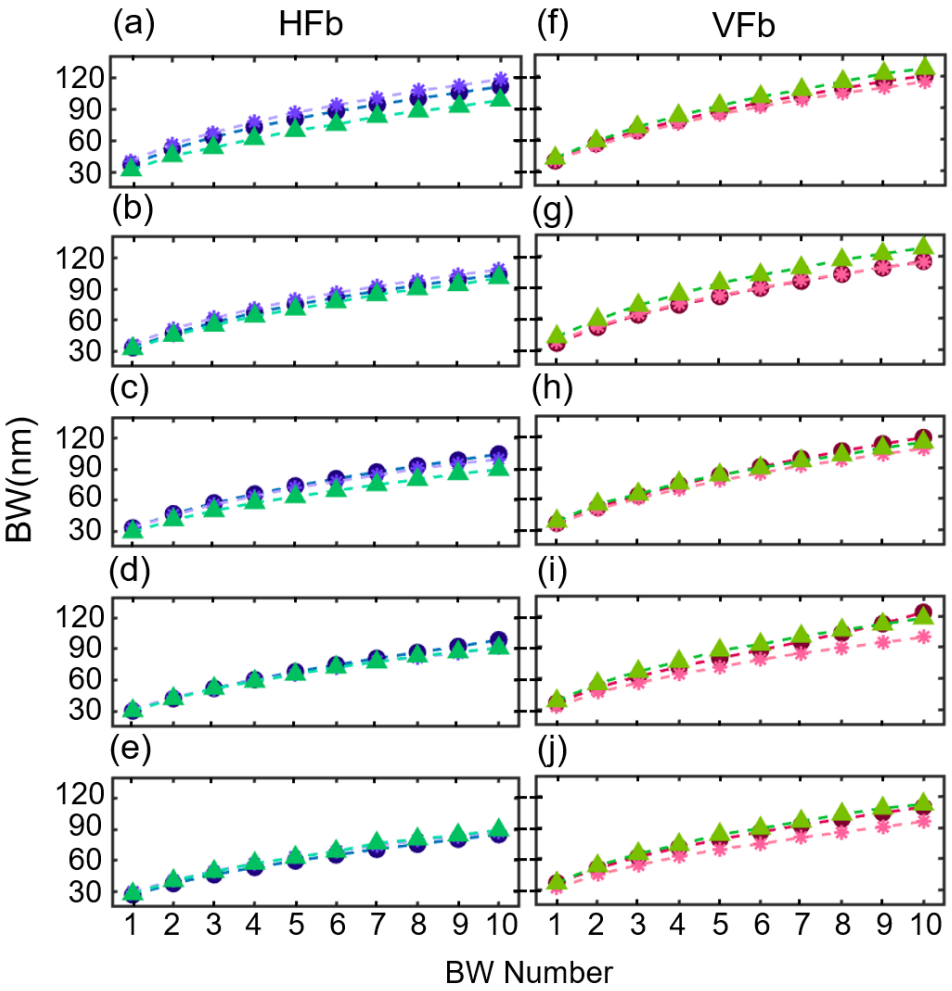

Figure 56: BW values as a function of the BW number. Panel (a)-(e) display the data for the HFb respectively calculated from the measured and computational CE curves (blue dotted and violet asterisk), and the one calculated from the reciprocal space analysis (green triangle) for (a) 220nm-thick SOI, (b) 260nm-thick SOI, (c) 290nm-thick SOI, (d) 320nm-thick SOI, and (e) 340nm-thick SOI. Panel (f)-(j) show the corresponding data for the VFb calculated from the measured and computational CE curve (red dot and pink asterisk), and the corresponding calculated from the reciprocal space analysis (light-green triangle).

agreement of the behaviors of the BWs, calculated exploiting the reciprocal space analysis, and the one evaluated from either the experimental and computational CE curves, is found for all the SOI platforms, independently from the coupling schemes under consideration. Moreover, the monotonically growth of the BW comes with no surprise as it simply derives from the BW definition.

In particular, the data related to the HFb display a progressive decrease of the BW values at each BW number moving from the 220nm-thick SOI to the 340nm-thick SOI, in accordance with the multiwavelength CEs of Figure 47. This behaviour is well supported by the analysis in reciprocal space and it can be compared with the study of the α_{int}, shown in Figure 35, and the n_{eff}^{BS} variation, reported in Figure 36.

Intuitively, this outcome can be understood considering the light propagation across the local pitches of the non-uniform GCs. In fact, a small α_{int} turns into a minor ability of the GC in scattering out the propagating light together with a gentler n_{eff}^{BS} variation that results in either lower values and a weaker wavelength dependence of the associated reflectivity, as reported in Figure 38, resulting in wider BWs.

These are all parameters that depend on the geometrical features of each non-uniform GC. The comparison between these quantities suggests that the wider the BW, the lower the α_{int} value and the gentler the linear n_{eff}^{BS} variation.

On the contrary, for the VFb, the data show a more homogeneous behavior across the different SOI platforms. The cause behind this phenomenon is the wider width of the sFT, proper of the VFb, that result in being less sensitive to the metastrcuture geometry, consequence of greater number of **k**-components carried by this light source.

Overall, the BW values obtained from the VFb are greater than the corresponding one of the HFb for all the SOI platforms. Incidentally, these results are in good agreement with the outcomes reported in [2].

Consequently, the design of the metastructure can be used to select on purpose the **k**-components supported by the apodized GC for each MFD.

In addition, the reciprocal space analysis is not implemented inside the PSO algorithm where the CE(λ_t) represents the only feedback used to maximize the performance of each design, where the effective refractive index is calculated resorting to n_{eff}^{AVG}, as reported in [4, 5], and then simply imported into the PSO without any further elaboration.

Nevertheless, the 2D-FDTD simulations of the optimized GC designs, given by the PSO, and the overlap between the E(**k**) curves and the sFT associated to VFb and HFb, predicted by the reciprocal space analysis, can be potentially used as two independent investigations to capture the entire physics behind the light propagation inside such complex metastructures, due to the good agreement between the two computational frameworks and, more importantly, the experimental results. Moreover, this sustains the hypothesis that the non-uniform GC can be treated as locally made of uniform GCs with their own local pitches and duty cycles.

Eventually, this approach can be added into the PSO optimization routine to either control the effective refractive index variation considering also the effect related to the MFD, helping to control the multiwavelength response of the GC and, hence, its BWs.

4.5 Conclusions

This chapter is focused on the multiwavelength response of these non-uniform GCs expanding and supporting the analysis reported in Chapter 3.

The nature of the BW is investigated performing either a reciprocal space analysis and a bandstructure investigation. The computational results suggest that the multiwavelength response of non-uniform GCs comes from the overlap between the sFT of the impinging light beam and the dispersion curves E(**k**), associated to the non-uniform GC. Hence, it was possible to explain the physical cause of the band pass filter effect, which affect the CE spectra resulting in an asymmetric curve about λ_t.

To prove this idea, the multiwavelength CEs associated to the best performing samples, reported previously were analysed. Moreover, a new campaign of measurements was performed exploiting a VFb coupling scheme on the same samples, offering the chance to compare for the first time the effect of two different MFDs, *i.e.* H-MFD and V-MFD, on the CE curve. Here, thanks to a new parameter $\eta^{\text{i-th BW}}$, it was possible to demonstrate that the VFb displays always better performances compared to the HFb due to the wider BW intervals. Moreover, the 290nm-thick non-uniform GC shows the highest $\eta^{\text{i-th BW}}$ values for both coupling schemes.

Then, the presence of the band pass filter effect was confirmed exploiting the ratio $\frac{\eta_L^{\text{i-th BW}}}{\eta_R^{\text{i-th BW}}}$ demonstrating that the right counterpart is always greater than the left one for all the SOI thickness with the exception of the 220nm-thick SOI.

Finally, the BW associated to a BW number spanning from 1dB to 10dB were calculated either through the experimental and computational CE curves as well as the proposed bandstructure approach showing that the three frameworks are in excellent agreement.

This demonstrates not only the predictability of the bandstructure approach but also that the multiwavelength response of such non-uniform GC depends on either the impinging MFD and the geometry of the non-uniform pattern. In fact, the latter, having

fixed the materials of the SOI, affects the variation of the effective refractive index, and hence the optical impedance matching.

In particular, this chapter shows experimentally to an even higher degree the reliability of the design process and the quality of the fabricated samples presented in this work.

As seen from the measurements, the process captures the entire physics behind grating-coupling going beyond the single wavelength CE, opening to the possibility of gaining full control on the coupling by tailoring the multiwavelength CE.

This is quite interesting for the world of Photonics Packaging since GCs represent one of the most promising solutions for integrated optical connectors and are relatively easy to be packaged.

However, up to now the limited BW is the major drawback of such coupling strategy. In this context considering the results of this chapter, Photonics Packaging can play an important role in improving the GC BW tailoring the issue at different levels.

First, the interfacing of micro optics between SMFs and PICs can be a suitable path to pursue in order to reshape the impinging MFD. The latest advantages in the fabrication of free form micro-lenses can represent an intriguing opportunity as explained in the thesis Introduction.

Second, a careful design of the non-uniform GC pattern, working directly on the E(**k**) curves with the specific aim of increasing the BW, can be used to tackle the issue. Indeed, this two approaches should be brought together in order to achieve the best results possible.

Bibliography

[1] Luca Zagaglia, et al., “Analysis in reciprocal space of the band-pass filter effect in uniform and non-uniform grating couplers,” in *Journal of Physics: Conference Series, 10th Young Reseracher Meeting*, Rome, IT, 2020.

[2] Marco Passoni, et al., “Grating couplers in silicon-on-insulator: The role of photonic guided resonances on lineshape and bandwidth,” *Applied Physics Letters*, vol. 110, no. 041107, pp. 1-5, 2017.

[3] Zhe Xiao, et al., “Bandwidth analysis of waveguide grating,” *Optics Express*, vol. 21, no. 5, pp. 5688-5700, 2013.

[4] Riccardo Marchetti, et al., “High-efficiency grating-couplers: demonstration of a new design strategy,” *Scientific Reports*, vol. 7, no. 16670, pp. 1-8, 2017.

[5] Luca Zagaglia, et al., “Experimental Characterization of Particle Swarm Optimized Focusing Non-Uniform Grating Coupler for Multiple SOI Thicknesses,” *Journal of Lightwave Technology*, vol. 39, no. 15, pp. 5028-5034, 2021.

Chapter 5

Grating Coupling for Laser-to-PIC Integration

Chapter 3 and 4 investigated grating couplers (GCs) for fiber-to-PIC coupling; however, GCs can be also exploited for direct laser-to-PIC coupling. The laser emission cannot be directly coupled into the PIC via typical GC structures, available from the Silicon foundries, as they are optimised for fiber-to-PIC coupling. Thus, the easiest way to overcome this problem is to introduce a new coupling scheme able to reshape the laser emission matching the emission of a single mode fiber. This chapter is focused on the design of such coupling scheme for direct laser-to-PIC grating coupling.

5.1 Direct Laser-to-PIC Coupling

The direct coupling of light into PICs is a quite active research field in Si Photonics for multiple applications; in fact, Silicon is an indirect-band gap material resulting in being not suitable for generating laser-diode emission due to the poor radiative recombination. In particular, the need of an on-PIC light-source is preferred for those applications where there is usually no necessity of integrating the photonic device into the telecom or datacom fibre-network; or where the light source has to be embedded together with the entire PIC in tiny and handy single packaged photonic device.

In this framework, the monolithic integration, *i.e.* a laser diode epitaxially growth directly on the Si-PIC surface, represents the ideal solution to overcome this issue. Indeed, it allows to fully exploit scalability, which is one of the major technological key-aspect of Si Photonics, and to fulfil other important requirements, one above all the high numbers of optical channels on a PIC maintaining low cost [1].

Up to know, there are a few examples of III-V, or Ge light sources developed for monolithic integration [2, 3, 4, 5, 6, 7, 8]. Here, the hetero-epitaxy growth, based either on molecular beam epitaxy or metal-organic vapour phase epitaxy [9], is used to grow

the optically active layer on the Si surface. However, the great mismatch of the lattice constants proper of the III-V materials and Si represents the major challenge to overcome.

The research community still needs time to ensure the development of a CMOS compatible monolithic process making it a credible technological solution addressing the request of the mass production at low cost [10].

Besides monolithic integration, light integration is performed exploiting three different approaches: (i) off-package light source with fiber coupling between the light source and PIC, (ii) direct bonding of the light source on the PIC, *i.e.* Heterogeneous Integration, (iii) in-package light source assembly, *i.e.* Hybrid Integration.

Off-package light source is typically employed in datacom applications where the integration procedure depends on conventional fiber coupling technology. In particular, this approach has the advantage of ensuring the independence of the light source and the PIC from the reliability and thermal management prospective. Despite these advantages, the off-package process is quite slow, expensive, and suffers from large module footprint.

Heterogeneous integration of a III-V material on the SOI is currently used to integrate the optically-active material/device directly onto the PIC surface, overcoming the difficulties behind monolithic integration [11, 12]. This approach allows either to bound a non-processed III-V heterostructure to the PIC surface, where additional etching processes compatible with Si technology are used to create the semiconductor optical amplifiers [13, 14]; or an optically active-device, *i.e.* laser-diode [15]. Here, the transfer printing [16, 17], and wafer-bonding [18, 19] techniques were proven to be efficient, cost effective, and scalable integration processes, potentially advantageous to address mass production. However, Heterogeneous Integration, being a post processing step, suffers from the lack of device testing and pre-selection before the bonding process.

An alternative to Heterogeneous Integration is represented by Hybrid Integration, where a discrete, external laser device is interfaced with the PIC [20, 21, 22, 23].

Hybrid-Integration has the great advantage of transferring only the already-tested devices, whose performances can be verified separately before mounting the laser. This ensures to avoid the possibility of having a final photonic device with poor efficiency, reducing the fabrication cost exploiting off-the-shelf components. In

particular, ensuring low final cost is quite interesting for sensing applications, where a portable medical photonic device represents the key-goal to achieve [24, 25].

The intrinsic mode-mismatch between the MFD and numerical aperture (NA) of the diffraction-limited emission of the laser-diode and the corresponding one of the PIC WGs can be overcome by opto-mechanically attach it to the PIC. Then, the coupling can be performed exploiting edge coupling [26, 27], or grating coupling. The latter can be achieved either through the use of micro-optic coupling [28, 29], or direct chip-to-chip coupling to GC [30].

Up to now, the major challenges in Hybrid Integration remain the development of a fast assembly process, with the final goal of maximising the CEs ensuring a small package footprint. Hence, Photonics Packaging plays an important role in the development and improvement of such approach.

5.2 Micro-Optical Bench (MOB)

Both Luxtera (Cisco) and Tyndall National Institute demonstrated the micro-optic coupling exploiting a coupling scheme based on a micro optical bench (MOB) [28, 31].

Regarding the MOB proposed by Snyder *et al.*, either a ceramic or a Si submount can be used as base to mount an edge emitting laser-diode, used as light source, and the μOptics, such as ball-lenses and μPrisms or a mirror. The ball-lens is used to collect, and reshape the laser emission to obtain a focal spot characterized by a Gaussian profile with a MFD of approximately 10μm, matching the acceptance-footprint of the GC. The μPrisms is exploited to deviate the travelling beam towards

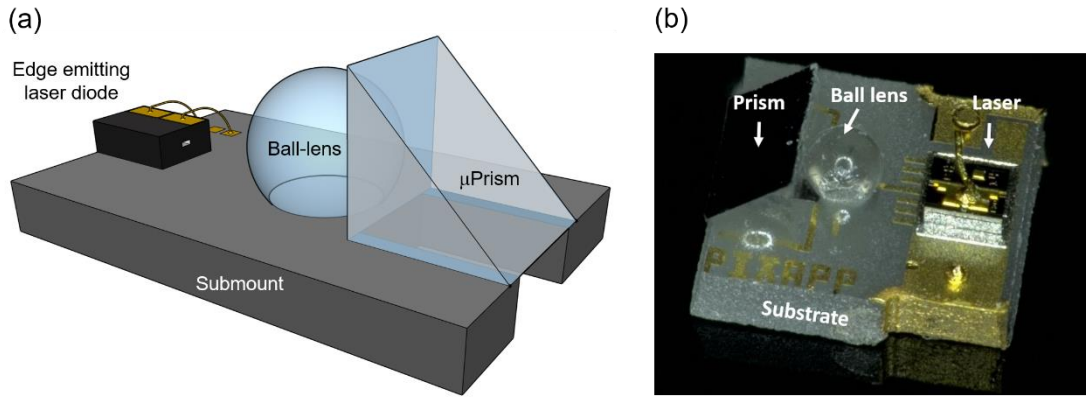

Figure 57: (a) Sketch of the Micro Optical Bench (MOB) where the ceramic/Si submount, the edge emitting laser-diode, the Ball-lens and the μPrism are explicitly pointed out. (b) Picture of a manufactured MOB taken from the PIXAPP project [32].

the PIC surface with the right impinging angle θ_i. Figure 57 shows the MOB design where all the component are pointed out.

The mechanical manufacturing of such coupling scheme is not straightforward. In particular, the laser-diode is placed on the ceramic submount exploiting the die-bonding or flip-chip technique, and the ball-lens is dropped passively on top of the ceramic submount exploiting a laser-drilled hole, previously made. The hole diameter width is used to control the final height of the lens, and the μPrisms is manually aligned bringing it into physical contact with the ball-lens and fixed using UV-curing Epoxy [28].

In addition, Duperron *et al.* proposed in [33] a more complex configuration where a Faraday isolator is used to avoid feedback into the laser cavity and it is placed in the middle of two different ball-lenses used to collimate and focus the light beam reducing spherical aberrations [49].

The key aspect of the MOB is the possibility of achieving an almost vertical coupling scheme exploiting a planar geometry, in analogy with the HFb coupling scheme. Moreover, it allows to have a final photonic device with an overall footprint of approximately $1.5mm^2$ and a total height of 0.5mm, fulfilling the sensing requirement of a small and portable device.

Indeed, the optical design of the MOB represents a critical step for the fabrication process as it fixes all the distances between the laser-diode and μOptics defining the final mechanical layout of the entire system.

Typically, the optical design is performed exploiting ray-tracing and physical optics softwares, such as Zemax [35], since the dimensions of the μOptics are way greater respect to the wavelength involved. Ray optics and physical optics simulations have the great advantage of being neither computational nor time-consuming making them a suitable tool to design such optical system.

However, these ray-tracing models use geometric-optics rules and empirical algorithms, rather than a true physics-engine, to generate solutions, and a fully vectorial description of the electromagnetic field is needed to describe the light-matter interaction in photonics structure such as GCs. Thus, a computational method based on full wave electromagnetism is necessary.

In particular, the FDTD, even though being computationally heavy, makes no assumptions or simplifications about the micro-optic elements in the MOB, and it can

be exploited to overcome this issue due to the recent advances in computer hardware architecture, *i.e.* amount of RAM, and both processor performances and number of cores. This enables to apply FDTD also for designing μOptical systems where the FDTD BOX has millimetre-scale dimensions.

In particular, the accuracy related to the FDTD simulation depends only on the mesh refinement used to discretize the simulation-space, which is practically limited only by the amount of memory and processing speed of the specific computer used to perform the simulations.

Thus, in a single-shot simulation all the information regarding the propagation of the laser-mode through the μOptics of the MOB, its interaction with the GC and consequently, the diffraction process behind the coupling into the WG can be obtained. Moreover, a straightforward access to the information on either the intensity and the wavefronts profiles, fundamental aspects in grating coupling, of the travelling wave are ensured.

Besides the full wave description of the electromagnetic field, the FDTD method resolves Maxwell's equations either in space and time offering, within the same simulation, the multiwavelength response of the system enabling to calculate the CE spectrum of the GC.

The next section is dedicated to show how millimetre-scale 2D-FDTD simulations can be used to capture the full physics behind this coupling scheme offering a powerful designing tool for grating coupling.

Through the simulations, the whole laser-to-WG insertion loss (IL) are calculated and compared to the one related to the VFb coupling scheme. In addition, further 2D-FDTD simulations are exploited to analyse either the alignment and the manufacturing tolerances of the MOB.

All the results presented in the next sections were published in [36].

5.3 MOB design and Simulation

Figure 58 panel (a) shows the VFb coupling scheme, and the MOB-based laser-to-PIC coupling scheme.

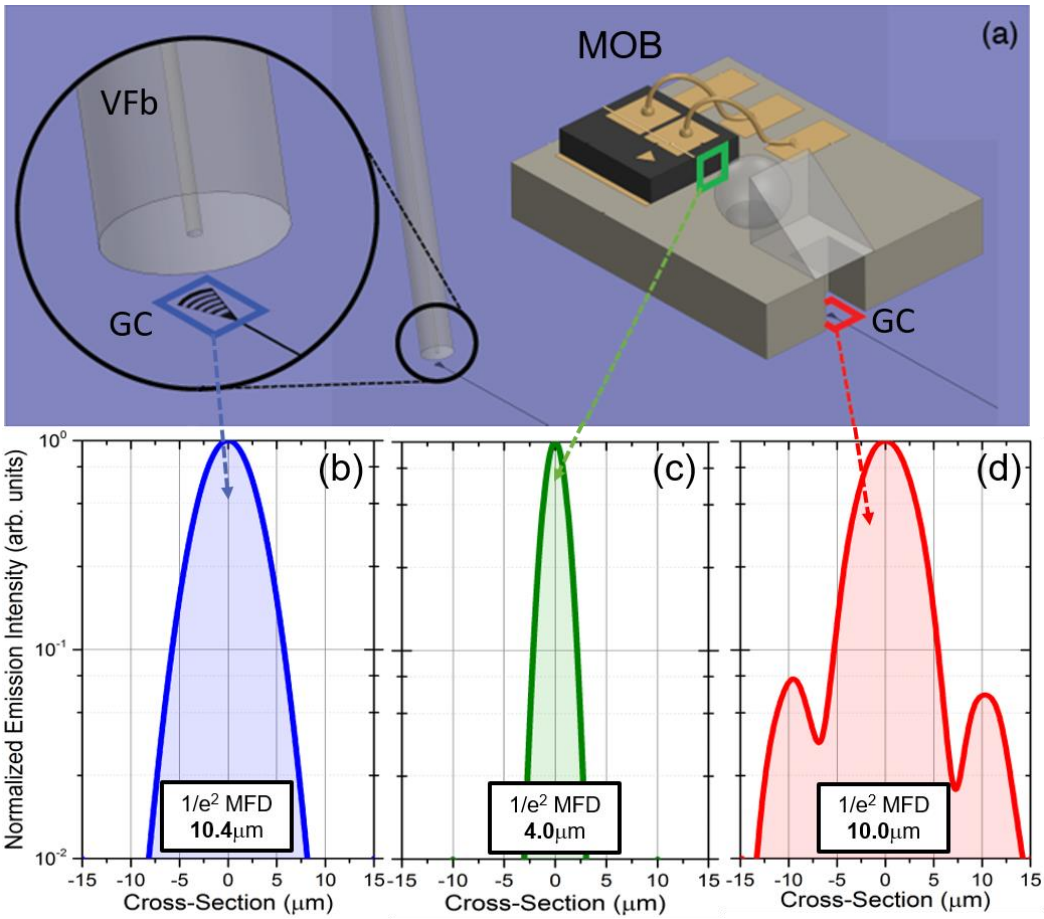

Figure 58: (a) Comparison between a vertical single mode fiber and the MOB systems. (b) Cross section of the Gaussian-intensity emission profile emitted by a single mode fiber, which has typically a mode field diameter of 10.4μm. (c) Cross section of the Gaussian source intensity profile used as laser light source. (d) Cross section along a perpendicular direction respect to the light propagation of the 2D-FDTD MOB focal spot taken at the most intense region. Figure has been taken from [36].

In particular, standard GCs, currently available as PDKs from the photonics foundries, are optimized to couple an emission intensity profile proper of a VFb with a MFD of 10.4μm at 1550nm.

This coupling scheme is considered the current benchmark to model the SMF emission exploiting a Gaussian source in the FDTD simulations. Figure 58 panel (b) represents the normalized intensity profile of the Gaussian beam extracted from a 2D-FDTD simulation used to model the SMF emission.

Therefore, these standard GCs are not designed to accept the beam-profile emitted from a typical laser-diode, which is characterized by a diffraction-limited emission

related to a WG region with a cross-section usually of approximately 2μm × 1μm. A cross-section of the Gaussian beam intensity profile used as laser light source is reported in Figure 58 panel (c).

Thus, the μOptics of the MOB overcome the mode-matching issue between the laser-diode and the GC as: (i) the ball-lens focuses the laser-mode onto the GC with the right 10μm MFD, and (ii) the μPrism through TIR guarantees the correct angle-of-incidence to couple efficiently the incoming beam at 1550nm. Figure 58 panel (d) shows a cross-section along a perpendicular direction, respect to the light propagation, related to the MOB focal spot extracted form a 2D-FDTD simulation collected at the most intense region. The side lobs around the central peak are clearly visible as direct consequence of the distortion of the focal spot image introduced by spherical aberrations.

The design parameters employed in the MOB design are summarized in Figure 59 panel (a).

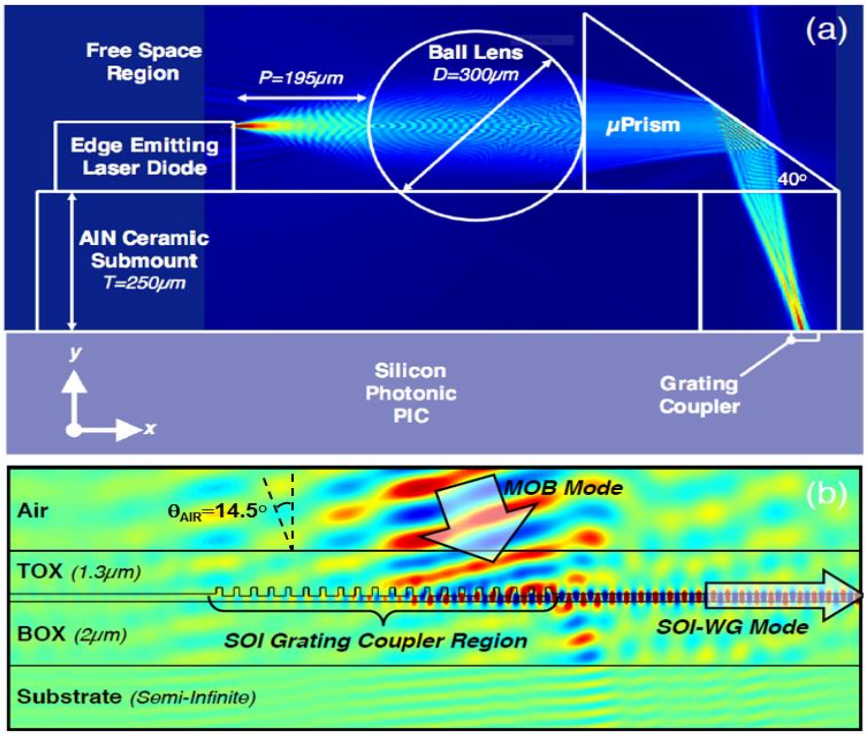

Figure 59: Light propagation inside the 2D FDTD simulation region. (b) Diffraction of the MOB mode inside the 220nm-thick WG through the GC. Figure has been taken from [36].

The light source has been modelled as a 110μm thick laser-diode with full-angle ($1/e^2$) of vertical-divergence of 28° [37]. The ball-lens is made of fused Silica, with a refractive index at 1550nm of n_{FS} = 1.44, with a diameter (D) of 300μm, while a 300μm-height fused-silica μPrism with a 40° polishing angle is used to deflect the

propagating Gaussian beam ensuring an impinging angle in Air θ_i = 14.5°, *i.e.* 10° inside the TOX layer.

Finally, either the laser-diode and the optics sit on an off-the-shelf 250μm-thick AlN-ceramic submount with a cut-out below the μPrism, to guarantee the re-imaging of the laser-mode on the PIC surface. The specific thickness of 250μm is employed to ease final manufacturing costs, but customize thicknesses are also accessible performing a polishing of the bottom-surface of the submount.

These design-parameters were chosen in accordance to the already existing MOB, reported in [28].

Figure 59 panel (b) display the design-parameters of the GC used to couple the MOB focal spot into the WG. The structure is a uniform-GC, made on a 220nm-thick SOI-layer, with a DC = 0.3 and an additional 160nm poly-Si overlay with an overall 230nm etching depth, *i.e.* measured form the top of the poly-Si overlay down to 70nm into the SOI-layer. The GC structure is sandwiched between a 2.0μm-thick BOX, and a 1.3μm-thick TOX. The choice of such uniform-GC with a poly-Si overlay is due to the high CE at 1550nm, as reported in [38], and these parameters are known to be the basis for the standard 1550nm TE-polarized uniform GCs, designed for an angle-of-incidence of 10° in the TOX and, currently available from IMEC MPW Si-Photonic foundry service [39].

An appropriate convergence test was performed to identify the minimum meshing-density required to describe the whole system, eventually finding adequate an auto-generated non-uniform mesh of approximately 30nm × 30nm at the GC region, and 80nm × 80nm at the micro-lens. In particular, the entire 2D-FDTD simulation BOX of the MOB and the GC has a dimension of 850μm × 550μm and it takes 3 hours to run on the PC with a liquid-cooled 16-core processor and 64GB of RAM.

Typically, the emission of a laser-diode is described by two separate divergence angles that define the beam-spreading in the far-field associated to the transverse and longitudinal planes, with respect to the propagation direction. This means that the propagating beam has an elliptical shape, with two separate MFDs.

Indeed, the wide 2D-FDTD simulation describes only the divergence of the laser-diode and the focusing-effect of the micro-lens in the x-y plane, *i.e.* the transverse plane in accordance with the coordinate system reported in Figure 59 panel (a). In fact, the parameters that most affect the final multiwavelength laser-to-PIC IL lie in this

specific plane, as they define the incoming phase-fronts of the focused-mode across the diffractive-elements, *i.e.* the teeth, of the GC [38].

On the contrary, the divergence and the focusing process related to the x-z plane, *i.e.* the longitudinal plane, which is not considered in the 2D-FDTD simulation, affects the lateral size of the focused-mode, along the diffractive-elements, of the GC. Thus, their effect can be simply managed by properly adjusting the width of the GC in order to accommodate the focused mode.

As shown in Figure 59 panel (a), the light is "injected" into the 2D-FDTD simulation exploiting a Gaussian-mode source with a MFD and a numerical aperture (NA) that guarantee a far-field angle of divergence, in the transverse plane, analogous to the one proper of a commercial laser-diode.

Then, the beam is collected by the ball-lens and re-focused when it leaves the exit curved surface, and it undergoes total internal reflection at the polished-facet of the μPrism. The light exits the bottom-facet of the μPrism entering in Air with an angle of refraction $\theta_{AIR} = 14.5°$, and it is focused onto the TOX-layer of the PIC. Here, it undergoes a second refraction effect entering into the TOX of the GC structure with an angle-of-incidence of $\theta_{GC} = 10°$.

Consequently, the single design-parameter exploitable to properly adjust the MFD in the x-y plane of the focused-mode on the GC is the laser-to-Lens distance (P).

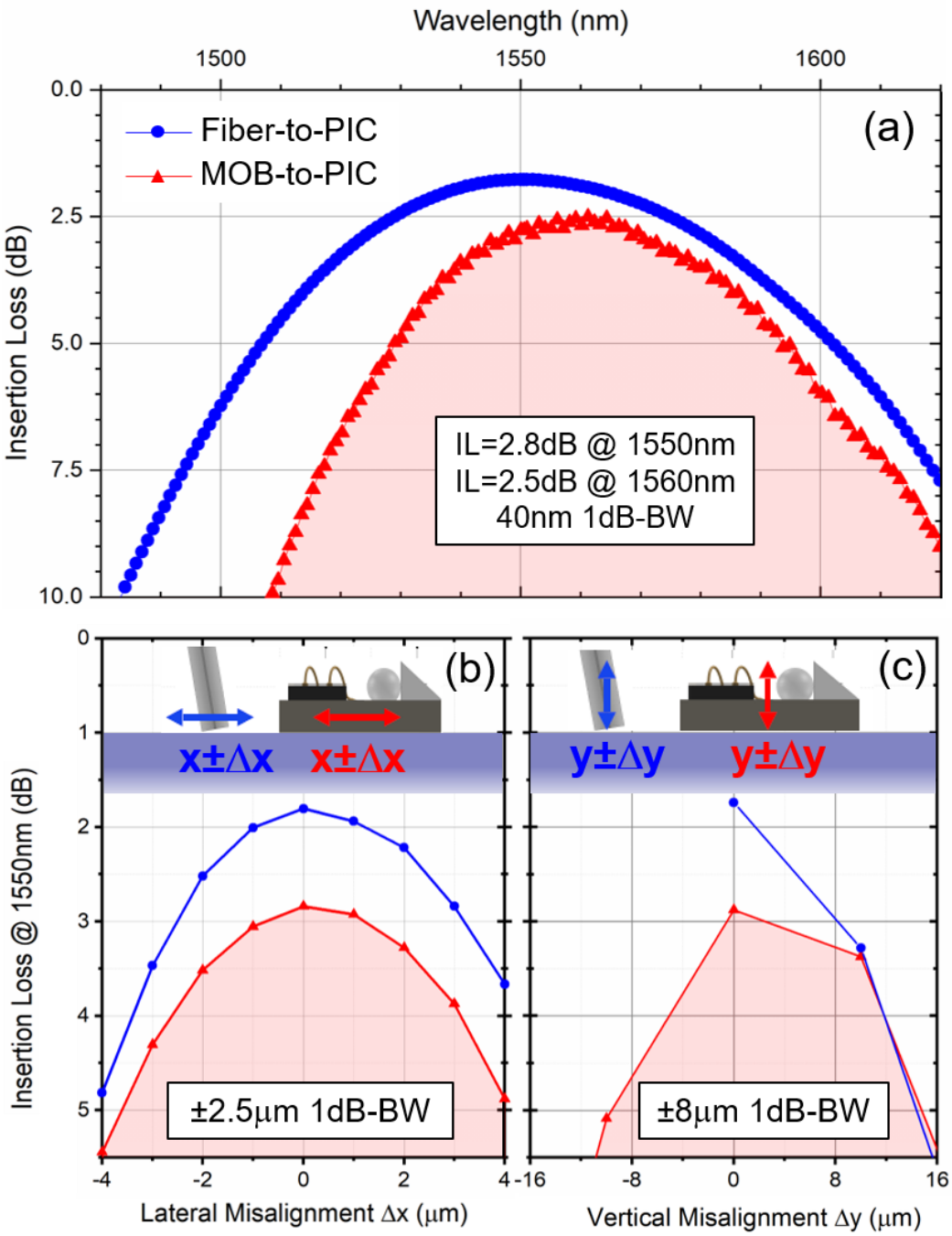

Figure 60: (a) A comparison between the IL of the fibre-to-PIC system and the MOB-to-PIC. The blue line refers to the Fibre IL and the red one refers to the MOB. (b,c) Comparisons in the IL between the lateral and vertical misalignments, Δx and Δy respectively, for the fibre-to-PIC and MOB-to-PIC coupling schemes with respect to their corresponding best positions x and y. Figure has been taken from [36].

A campaign of 2D-FDTD simulations were run to tune the value of P in order to identify the configuration that gives the lowest laser-to-PIC IL of the aforementioned MOB design. Eventually, a computational IL of 2.8dB was achieved through the optimum MOB design with a value of P = 195μm, for this uniform GC with a poly-Si overlay.

5.4 MOB Insertion Losses and Tolerances

Figure 60 panel (a) shows the comparison between the computational multiwavelength ILs of both VFb and laser-to-PIC coupling schemes evaluated for the same uniform-GC.

The 2D-FDTD of the VFb coupling scheme has an IL of 1.8dB at 1550nm, resulting in a performance-penalty of 1.0dB extra-loss for the MOB.

The performed millimetre-scale 2D-FDTD simulation, capturing the whole physics behind the aberration, the reflection and the diffraction in the light propagation across the MOB, enables to weight separately the effect of these contributes on the 1.0dB extra penalty displayed by the optimum MOB design. In particular, the 1dB higher IL, *i.e.* 20% reduction, can be attributed to two effects: (i) the multiple reflections at the different air-to-glass interfaces, calculated thanks to a monitor placed right after the bottom-face of the μPrism, that count for about 0.6dB, *i.e.* 12%, and (ii) the reduced modal-overlap related to the focused-mode on the GC due to spherical-aberration effects that counts for about 0.4dB, *i.e.* 8%. The latter can be estimated considering the cross-section intensity profile reported in Figure 58 panel (d).

The total area under the curve can be divided into three separate regions: one related to the left side lobe, a second related to the central peak, and a third one related to the right side lobe, as reported in Figure 61. Here, the green areas associated to the

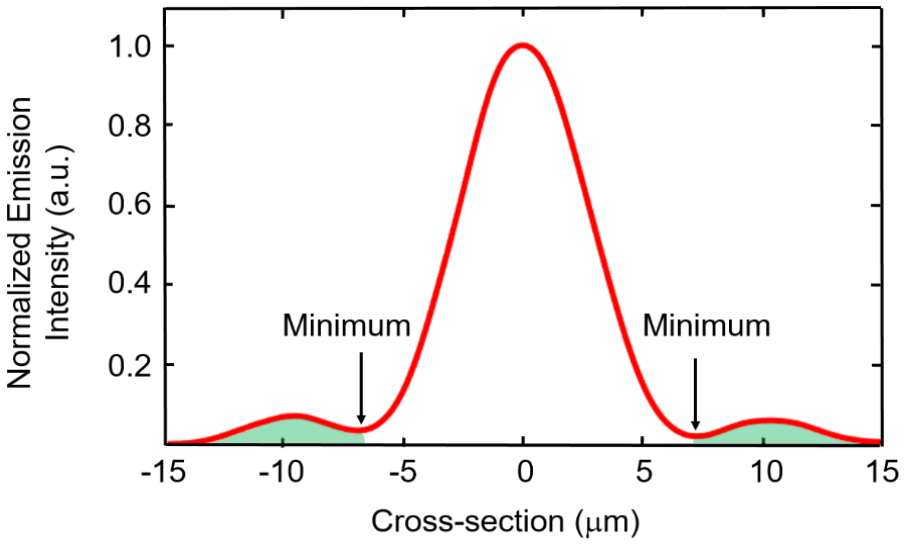

Figure 61: Cross section along a perpendicular direction respect to the light propagation of the 2D-FDTD MOB focal spot taken at the most intense region. The green side lobe regions refer to the areas under the curve

side lobes where calculated performing a numerical integration, excluding the area between the two minima associated to the central peak, and they count for the 8% of

the total area. Thus, the 8% of the power stored inside the side lobes is simply lost during the coupling process.

The losses are broken-down in Figure 62, where the initial power emitted by the laser is supposed to be, as an example, 0dBm (1mW). This reference value is chosen

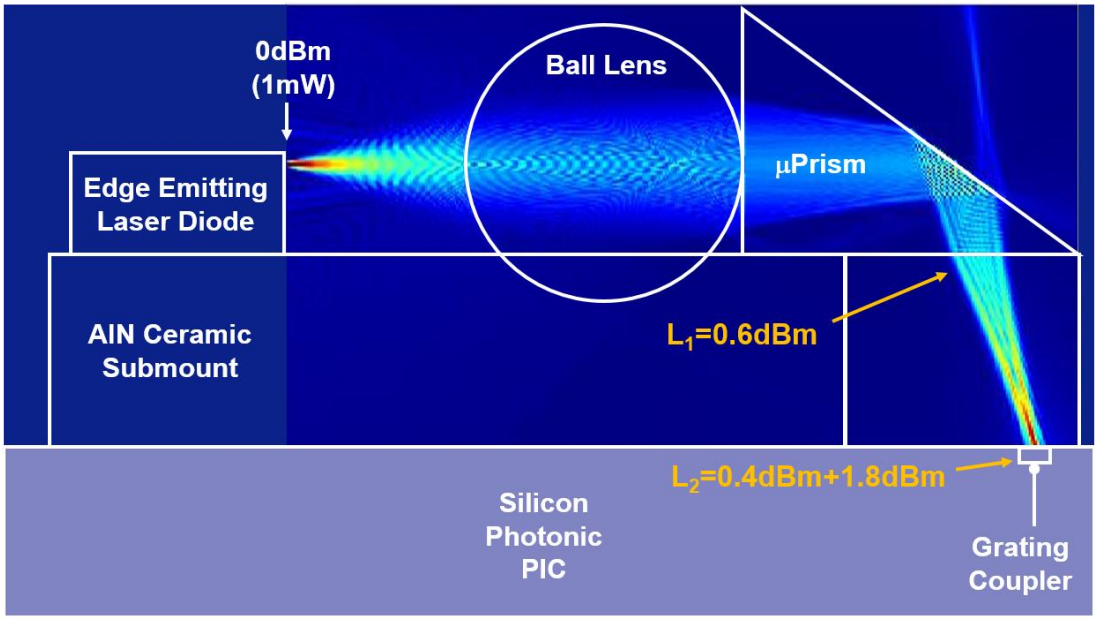

Figure 62: Break-down of the losses related to the MOB coupling scheme. The initial power emitted by the laser is supposed to be equal to 0dBm (1mW), L_1 indicates the loss due to the back-reflections, and the L_2 is the sum of the losses due to spherical aberrations and mode overlap. Figure has been taken from [36] and adapted.

for demonstrative purposes only to simplify the calculus and evaluate the final IL=L1+L2 of 2.8dBm at 1550nm. In particular, the 1.8dBm value, *i.e.* mode overlap loss, refers to the one proper of the coupling of the central peak enabled by the GC.

While the extra losses coming from interface-reflections can be easily minimized exploiting specific anti-reflection coatings on the μOptics; on the other hand, the designing of a GC able to accommodate the wider spot-size as well as the variable phase-fronts of the spherically-aberrated focused mode represents a more challenging task. However, the optimization routine developed in this thesis, or alternatively designing techniques based on genetic-algorithms, can be potentially exploited to tackle this designing problem. In addition, the calculated 1dB BW associated to laser-to-PIC coupling scheme is about 40nm.

The multiwavelength laser-to-PIC IL in Figure 60 refers to an ideally impeccable fabricated MOB that is perfectly aligned over the GC. To investigate the alignment tolerances of the MOB, and compare them to direct fibre-to-PIC coupling, a campaign of 2D-FDTD simulations were exploited, where both the horizontal (Δx) and vertical

(Δy) offsets were introduced misaligning on purpose the ideal MOB (and fibre) positions.

Figure 60 panel (b) shows that both the MOB and the fibre display comparable 1dB horizontal alignment tolerances with a value of ±2.5μm, result compatible with the Epoxy-bonding employed to attach the MOB to the surface of the PIC, after pursing an active-alignment process. In this framework, the 1dB limit in the tolerances was selected as considered the actual benchmark for alignment processes in Photonics Packaging.

On the other hand, Figure 60 panel (c) suggests that the MOB has a 1dB vertical alignment tolerance of ±8μm, which is outside the ±5% manufacturing tolerances that are typical for a 250μm-thick AlN-substrate. The tight tolerance is a consequence of the change in the focal spot position along x due to the vertical misalignment. However, it is always possible to realign along the **x**-direction the GC, consequently compensating the wrong impinging position exploiting the extended MOB-focal region, which is roughly 65μm. In addition, the VFb coupling scheme alignment data are only displayed for positive values of Δy, as the fibre cannot be pushed "through" the PIC surface. The 2D-FDTD simulations suggest that the 1dB alignment tolerances of the MOB are analogous to those of a VFb for grating coupling, and more importantly are compatible with the current alignment processes used in Photonics Packaging.

Figure 63 shows the computational analysis of the fabrication tolerances on the MOB coupling performances.

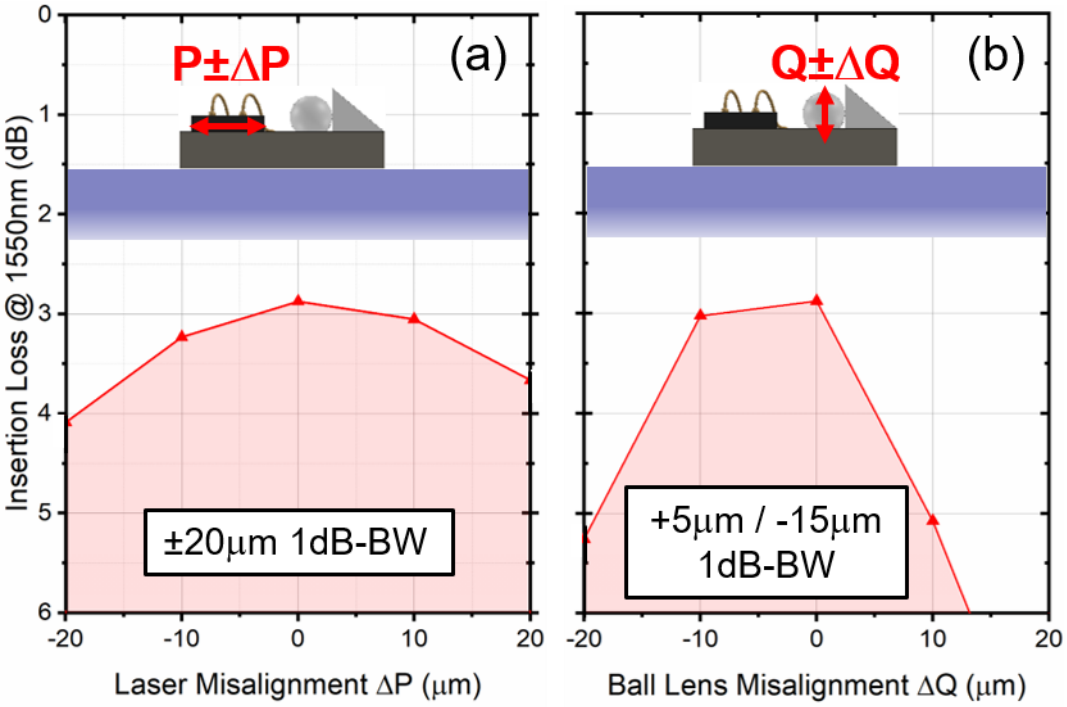

Figure 63: (a) Behavior of the IL value due to a laser misalignment (ΔP) on the ceramic substrate. b) Variation of the IL as a function of a misalignment in the ball-lens height. (a) and (b) represent the consequences in the IL value of the fabrication tolerances. Figure has been taken from [36].

Multiple 2D-FDTD simulations were run to study the effect related to a horizontal offset (ΔP), introducing a misalignment on the best horizontal position (P), and a vertical offset (ΔQ) affecting the micro-lens best vertical position (*i.e.* Q=0µm, thus the lens optical-axis is perfectly aligned with the centre of the laser exit slit, as reported in Figure 59 panel (a)).

Figure 63 panel (a) suggests that the 1dB laser-to-lens horizontal alignment tolerance is ±20µm, showing an excellent compatibility with the capabilities of either the flip-chip or precision pick-and-place processes used to attach the laser-diode to the AlN-substrate.

Instead, Figure 63 panel (b) shows that the 1dB laser-to-lens vertical alignment tolerance is way tighter, displaying values of +5 µm /-15 µm. In particular, the asymmetric ±ΔQ turns into an asymmetric change in either the optical path-length and the propagation-direction through the µPrism resulting in the asymmetry of this tolerance. Moreover, it also changes the angle-of-incidence of the focused-mode impinging at the surface of the PIC, and shifts the focused-mode across the GC. Nevertheless, this previous effect has been re-compensated retuning the horizontal

position of the MOB above the GC (*i.e.* Δx) for each data-point displayed in Figure 63 panel (b), therefore all the corresponding results are shown under an optimum alignment condition.

Actually, two potential origins behind a ΔQ offset can be pointed out. The first one is due to a variation in the thickness of the laser-diode, coming from the polishing-tolerances of the InP-wafer; the second one is related to a variation in the optimum width of the diameter proper of the ball-lens laser-drilled hole on the AlN-substrate, due to fabrication tolerances.

Taking into account the manufacturing tolerances reported in [28], the -15μm 1dB alignment tolerance is technically within the variations introduced by this effect, even though displaying tight margin; on the other hand, the +5μm 1dB alignment tolerance is outside of the manufacturing tolerances, which are currently approximately 12μm.

Thus, it is quite important to ensure that these fabrication processes are performed at a high-level of their nominal specification, and additional improvements in the fabrication processes should be introduced to overcome such tight tolerances.

Eventually, considering the exposed results, the MOB can be potentially a reasonable alternative to the fibre in order to couple light directly into a PIC via a GC. However, it is to be considered that a 2D model is not able to capture the entire complexity of the real MOB features where the 0.4dB can easily increase in a more realistic full 3D model. Nevertheless, to partially overcome such an issue, it is possible make an easy assumption.

Figure 64 shows a straightforward comparison of the different amount of power distributed inside the main peak in the 2D and 3D MOB mode models.

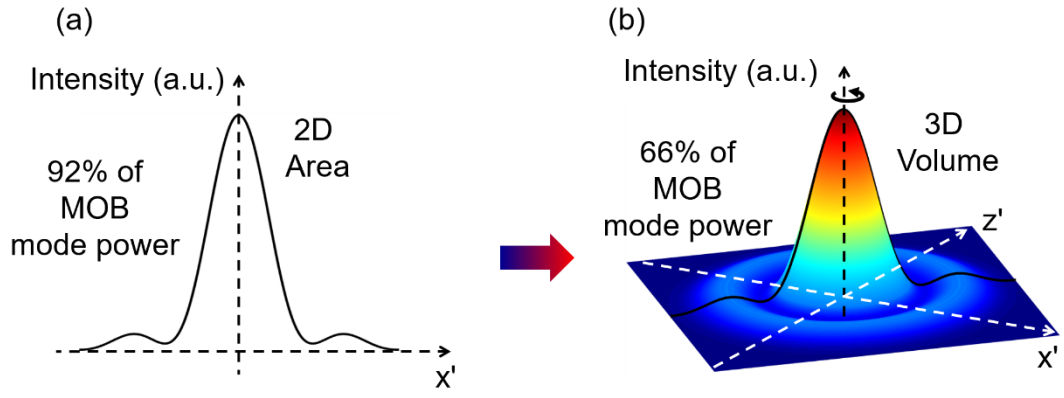

Figure 64: (a) 2D MOB mode model of the power profile where the central peak occupies the 92% of the total area. (b) 3D solid of revolution created rotating the 2D MOB mode profile around its vertical axis. In this case, the central peak represents the 66% of the total volume.

Regarding the 2D model, as stated previously, the power percentage stored into the main peak with respect to the total one can be estimated as the surface fraction enclosed inside the two minima as shown in Figure 61. This quantity represents the 92% of the total area/power.

On the other hand, an easy 3D model can be generated rotating the 2D mode curve around the vertical axis and creating consequently its solid of revolution. Here, the estimated power percentage, equivalent to the 2D area of the central peak, corresponds to the volume ratio bounded, again, between the two minima. Now this value represents the 66% of the total volume/power, implying a substantially redistribution of the fraction of power stored in the central peak. Therefore, a greater importance, with respect to the 2D model, of the side lobes should be expected in determining the laser-to-PIC IL. Here, a rough estimate of the 3D IL at 1550nm can be determined assuming valid the 0.6dBm (88%) and 1.8dBm (66%) losses, see Figure 62, for the 3D model. In this case, the estimated 3D IL is calculated as 3D IL=(0.6+1.8+1.8)dBm= 4.2dBm (38%), which turns into an additional loss of 1.4dBm with respect to the 2D model.

5.5 Conclusions

This last chapter is focused on the optical design of a MOB for hybrid integration of a laser source with a SOI-PIC exploiting the grating coupling technique.

First, an introduction to the monolithic, Heterogeneous and Hybrid Integration is provided as the main approaches currently exploited to achieve the integration of laser source onto a SOI-PIC. Then, the attention is brought to the Hybrid Integration approach and in particular to the MOB structure.

In this context, millimetre-scale 2D-FDTD simulations are shown to be a powerful tool either to design and to optimize the MOB for efficient laser-to-PIC coupling. Compared to direct fiber-to-PIC coupling, the MOB showed only a 1dB extra IL at 1550nm, where 0.6dB of such additional penalty is due to the back reflections at the interfaces of the μOptics. This can be easily overcome by introducing AR-coatings at each interface. While, the remaining 0.4dB of extra penalty derives from spherical aberrations that introduce a distortion in the focal spot creating side lobes. This effect can be in principle resolved through the application of the design routine, described in chapter 2, optimizing a GC to accommodate the MOB focal spot.

Additionally, 2D-FDTD simulations were performed to investigate the 1dB alignment and fabrication tolerances demonstrating that they are compatible with real Photonics Packaging processes. Particular attention to the ball-lens height must be paid as the most critical one in terms of fabrication tolerances.

Overall, the alignment tolerances of the MOB were shown to be comparable to the one related to direct fiber-to-PIC coupling. Eventually, a brief comment on how the 2D-FDTD results could be generalized further to a 3D description is provided by taking into account the solid of revolution related to the 2D MOB focal spot. The redistribution of the energy across the central peak and the side lobes in 3D change with respect to the 2D case. This suggests that the weight of the side lobes on the laser-to-PIC coupling could potentially increase the IL leading to an estimated additional loss of 1.4dBm.

Bibliography

[1] Zhechao Wang, et al., “Novel Light Source Integration Approaches for Silicon Photonics,” *Laser & Photonics Review,* vol. 11, no. 4, pp. 1700063(1-21), 2017.

[2] Rodolfo E. Camacho-Aguilera, et al., “An electrically pumped germanium laser,” *Optics Express,* vol. 20, no. 10, pp. 11316-11320, 2012.

[3] Shinichi Saito, et al., “Towards monolithic integration of germanium light sources on silicon chips,” *Semiconductor Science and Technology*, vol. 31, no. 4, pp. 043002(1-19), 2016.

[4] Zhechao Wang, et al., “Room-temperature InP distributed feedback laser array directly grown on silicon,” *Nature Photonics,* vol. 9, p. 837–842, 2015.

[5] N. Hossain, et al., “Reduced threshold current dilute nitride,” *Electronics Letters,* vol. 47, no. 16, p. 931 – 933, 2011.

[6] Fanglu Lu, et al, “Nanopillar quantum well lasers directly grown on silicon and emitting at silicon-transparent wavelengths,” *Optica,* vol. 4, no. 7, pp. 717-723, 2017.

[7] Zhechao Wang, et al., “Polytypic InP Nanolaser Monolithically Integrated on (001) Silicon,” *Nano Letters,* vol. 13, no. 11, p. 5063–5069, 2013.

[8] Thomas Frost, et al., “Monolithic Electrically Injected Nanowire Array Edge-Emitting Laser on (001) Silicon,” *Nano Letters,* vol. 14, no. 8, pp. 4535-4541, 2014.

[9] Sebastian Lourdudoss, “Heteroepitaxy and selective area heteroepitaxy for silicon photonics,” *Current Opinion in Solid State and Materials Science,* vol. 16, no. 2, pp. 91-99, 2012.

[10] Qiang Li and Kei May Lau, “Epitaxial growth of highly mismatched III-V materials on (001) silicon for electronics and optoelectronics,” *Progress in Crystal Growth and Characterization of Materials,* vol. 63, no. 4, pp. 105-120, 2017.

[11] Sasan Fathpour, “Emerging heterogeneous integrated photonic platforms on silicon,” *Nanophotonics,* vol. 4, no. 2, p. 143–164, 2015.

[12] Xuhan Guo, et al., “Recent advances of heterogeneously integrated III–V laser on Si,” *Journal of Semiconductors,* vol. 40, no. 10, pp. 101304(1-11), 2019.

[13] J. Pu, et al., “Heterogeneous Integrated III–V Laser on Thin SOI With Single-Stage Adiabatic Coupler: Device Realization and Performance Analysis,” *in IEEE Journal of Selected Topics in Quantum Electronics,* vol. 21, no. 6, pp. 369-376, 2015.

[14] Shahram Keyvaninia, et al., “Demonstration of a heterogeneously integrated III-V/SOI single wavelength tunable laser,” *Optics Express,* vol. 21, no. 3, 2013.

[15] Joan Manel Ramirez, et al., “III-V-on-Silicon Integration: From Hybrid Devices to Heterogeneous Photonic Integrated Circuits,” *in IEEE JOURNAL OF SELECTED TOPICS IN QUANTUM ELECTRONICS,* vol. 26, no. 2, pp. 6100213(1-13), 2020.

[16] Ruggero Loi, et al., “Edge-Coupling of O-Band InP Etched-Facet Lasers to Polymer Waveguides on SOI by Micro-Transfer-Printing,” *in IEEE Journal of Quantum Electronics,* vol. 56, no. 1, pp. 1-8, 2020.

[17] Brian Corbett, et al., “Transfer Printing for Silicon Photonics,” in *Silicon Photonics*, Elsevier Inc. , 2018, pp. 43-70.

[18] Brian Corbett, et al., “Strategies for integration of lasers on,” *Semiconductor Science and Technology,* vol. 28, no. 9, pp. 094001(1-6), 2013.

[19] Badhise Ben Bakir, et al., “Heterogeneously Integrated III-V on Silicon Lasers,” *ECS Transactions,* vol. 64, no. 5, pp. 211-223, 2014.

[20] L. Grenouillet, et al., “Hybrid integration for silicon photonics applications,” in *2011 ICO International Conference on Information Photonics*, Ottawa, ON, Canada, 2011.

[21] A. Moscoso-Mártir, et al., “Hybrid silicon photonics flip-chip laser integration with vertical self-alignment,” in *2017 Conference on Lasers and Electro-Optics Pacific Rim (CLEO-PR),* Singapore, 2017.

[22] T. Matsumoto, et al., “Hybrid-Integration of SOA on Silicon Photonics Platform Based on Flip-Chip Bonding,” *Journal of Lightwave Technology*, vol. 37, no. 2, pp. 307-313, 2019.

[23] Muhammad Rodlin Billah, et al., “Hybrid integration of silicon photonics circuits and InP lasers by photonic wire bonding,” *Optica*, vol. 5, no. 7, pp. 876-883, 2018.

[24] Lee Carroll, et al., “Photonic Packaging: Transforming Silicon Photonic Integrated Circuits into Photonic Devices,” *Applied Sciences*, vol. 6, no. 12, pp. 426(1-21), 2016.

[25] Enxiao Luan, et al., “Silicon Photonic Biosensors Using Label-Free Detection,” *Sensors*, vol. 18, no. 10, pp. 3519(1-42), 2018.

[26] Nobuaki Hatori, et al., “A novel spot size convertor for hybrid integrated light sources on photonics-electronics convergence system,” in *The 9th International Conference on Group IV Photonics (GFP)*, San Diego, CA, USA, 2012.

[27] Sebastian Romero-García, et al., “Edge Couplers With Relaxed Alignment Tolerance for Pick-and-Place Hybrid Integration of III–V Lasers With SOI Waveguides,” *in IEEE Journal of Selected Topics in Quantum Electronics*, vol. 20, no. 4, pp. 369-379, 2014.

[28] Bradley Snyder, et al., “Hybrid Integration of the Wavelength-Tunable Laser With a Silicon Photonic Integrated Circuit,” *JOURNAL OF LIGHTWAVE TECHNOLOGY*, vol. 31, no. 24, pp. 3934-3942, 2013.

[29] Thierry Pinguet, et al., “High-Volume Manufacturing Platform for Silicon Photonics,” *in Proceedings of the IEEE*, vol. 106, no. 12, pp. 2281-2290, 2018.

[30] Bowen Song, et al., “3D integrated hybrid silicon laser,” *Optics Express*, vol. 24, no. 10, pp. 10435-10444, 2016.

[31] M. Mack and, et al., “Method And System For A Light Source Assembly Supporting Direct Coupling To An Integrated Circuit”. United States Patent US008168939B2, 1 May 2012.

[32] Pixapp, Pixapp, [Online]. Available: www.pixapp.eu

[33] Matthieu Duperron, et al., “Hybrid integration of laser source on silicon photonic integrated circuit for low-cost interferometry medical device,” in *Optical Interconnects XVII*, San Francisco, California, United States, 2017.

[34] Max Born, et al., “Elements of the theory of diffraction,” in *Pinciples of Optics* , Cambridge , Cambridge Press, 1999, pp. 413-417.

[35] Zemax , Zemax , [Online]. Available: https://www.zemax.com

[36] Luca Zagaglia, et al., “Comparing Laser Hybrid-Integration and Fiber Coupling With Standard Grating Couplers on Si-PICs,” *IEEE Photonics Technology Letters,* vol. 31, no. 1, pp. 66-69, 2019.

[37] Haiyin Sun, "A Practical Guide to Handling Laser Diode Beams," Pittsburgh, PA: Springer, 2015.

[38] Deidrick Vermeulen, et al., “High-efficiency fiber-to-chip grating couplers realized using an advanced CMOS-compatible Silicon-On-Insulator platform,” *Optics Express,* vol. 18, no. 17, pp. 18278-18283, 2010.

[39] Europractice, “IMEC Techologies,” IMEC, [Online]. Available: https://europractice-ic.com/technologies/photonics/imec/

Chapter 6

Conclusions and Future Work

Photonics Packaging represents one of the most significant bottleneck in Integrated Photonics for the development of commercial photonic devices, as it is still very challenging, expensive, and slow. In particular, CEs are low with tight alignment tolerances, which require time-consuming active alignment processes.

In this context, GCs represent a suitable solution to couple the light signal into a PIC, as they are relatively easy to package due to the relaxed alignment tolerances showing potential high CEs.

In my work, I investigated how to optimize a promising class of GCs, called non-uniform GCs, known to deliver high values of CEs, for a specific coupling scheme, called HFb, based on a single mode fiber horizontally interfaced with the PIC.

This scheme is particularly interesting and advantageous for Photonics Packaging due to its mechanical stability, form-factor, and relaxed alignment tolerances. The final aim was a coupling scheme based on grating coupling easy to package, robust, and showing top-class CE value.

To achieve this, it was necessary to start from the design performing either detailed theory, and computational work, and then validate the results through experimental work, using advanced packaging equipment.

To optimise such GCs, a customized design routine was developed resorting to a PSO algorithm, which was implemented inside the commercial FDTD software, Lumerial® FDTD Simulations™. The structure of the design routine is presented with particular attention on the PSO operational behavior, showing how a general GC structure is optimized starting from a generic sets of parameters to the final 3D optimized-structure. The validation of the design routine was done optimizing two "gold" GC structures well-known in literature, a uniform GC with a Si-overlay and a non-uniform GC, showing the ability of the design routine in giving optimized structures that show either CE values and structural parameters in agreement with the corresponding results reported in literature.

The design routine was presented at the 41st *PhotonIcs & Electromagnetics Research Symposium* in Rome and the results published in the corresponding conference paper.

Consequently, high-performance focusing non-uniform GCs for high-efficiency optical connection for Photonics Packaging were designed, resorting to the aforementioned design routine, fabricated, tested and packaged in this thesis. In particular, the GCs were optimised for multiple SOI-thicknesses spanning from the 220nm-thick to the 340nm-thick SOI, considered two standard SOI platforms for Integrated Silicon Photonics.

The experimental results showed CEs at 1550nm up to 83% for the 340nm-thick SOI, one of the highest value reported in literature, and an excellent agreement with the computational predictions across all the SOI thicknesses was demonstrated.

These results were published in the *Journal of Lightwave Technology* and, due to the high CE values, the designs were asked as official PDKs by Cornerstone, the Silicon photonics foundry of the University of Southampton, which fabricated the samples.

Furthermore, the performances of each SOI-thickness were analysed looking at the physics behind each optimized design through the introduction of the integrated scattering leakage factor, new parameter in this field of research. In addition, the variation of the optical impedance matching along the GC pitches was studied exploiting a photonic bandstructure approach showing that a linear apodization of the local pitches turns into a linear variation of the n_{eff}^{BS}.

The reflectivity for each sample was calculated either from the measurements and the simulations in order to compare the quality of the impedance matching consequence of the apodization of the local pitches demonstrating low losses, below 1%, of the best performing samples.

As a further investigation regarding the quality of the fabricated samples, an additional structural analysis was conducted scarifying a 260nm-thick SOI GC, previously characterized, to take SEM images of the apodized local pitches. These were used to rebuild inside the FDTD software the corresponding structure and the CE compared to the measured one showing, again, an excellent agreement.

For all these reasons, the aforementioned outcomes can be considered a valuable contribute for the current state-of-the art of Integrated Silicon Photonics and in

particular of Photonics Packaging, offering new, efficient, and relatively easy to align structures to interface with the promising HFb coupling scheme.

The performance analysis was broadened pursing a detail investigation of the multiwavelength response of such structure exploiting the previously measured CE curves. Here, the attention was focused on the behavior and nature of the asymmetry of the CE curve, with respect to the working-wavelength (λ_t), and the BW of such non-uniform GCs.

In this context, a new campaign of measurements was conducted on the best samples using, this time, a vertical fiber coupling scheme (VFb), which is characterized by a smaller MFD with respect to the HFb coupling scheme. The results were then compared with the FDTD counterparts.

Thanks to the introduction of a new parameter $\eta^{\text{i-th BW}}$, the VFb was demonstrated to have higher performances compared to the HFb due to the wider BW intervals for each SOI thickness, direct consequence of its smaller MFD. In particular, the 290nm-thick non-uniform GC was proven to be the most efficient design above all for both coupling schemes.

Then, the ratio $\frac{\eta_L^{\text{i-th BW}}}{\eta_R^{\text{i-th BW}}}$ was introduced to quantify the asymmetry of the CE curve, hence studying the redistribution of the energy made by each non-uniform GC. Except the 220nm-thick non-uniform GC, all designs have a value of the ration smaller than 1, showing the existence of an asymmetry in the CE curve resulting in higher efficiencies associated to wavelength intervals $[\lambda_t,\lambda]$, with $\lambda>\lambda_t$, with respect to intervals $[\lambda,\lambda_t]$, with $\lambda<\lambda_t$.

This behaviour can be described in terms of a band pass filtering effect, which selects differently the wavelength about λ_t affecting, consequently, the BW values. In particular, the nature of such effect was studied calculating the BW associated to a BW number, spanning from 1dB to 10dB, either through the experimental and computational CE curves as well as through the proposed bandstructure approach showing that the three frameworks are in excellent agreement.

This not only suggests the predictability of the bandstructure approach in calculating the BW, but more importantly how the nature of the BW is directly consequence of the optical impedance matching, which depend on the material, the non-uniform pattern of each GC, and the impinging MFD.

The analysis of the multiwavelength response of such non-uniform GCs led to a talk at the international conference: "*10th Young Research Meeting"* in Rome, to the corresponding conference paper.

The outcomes of Chapter 4 ensure not only a better understanding of the optical response of such complicated non-uniform GCs, but they are interesting for the tailoring of the BW values. In fact, the BW represents the major bottleneck for grating coupling due to their limited values and Photonics Packaging can have a key-role in overcoming such issue.

Finally, the last thesis chapter shows how grating coupling can be further generalized as an efficient coupling scheme for laser-to-PIC coupling exploiting a configuration based on a MOB.

Here, millimetre-scale 2D FDTD simulations are proposed for the first time as a powerful designing tool to optimize the entire MOB structure. In fact, in a single shot simulation all the information regarding the propagation of the electromagnetic field across the optics can be obtained as well as the interaction with the GC and the final CE.

In particular, when the MOB is perfectly aligned, it showed only a 1dB extra IL at 1550nm, respect to the fiber-to-PIC coupling scheme. This extra loss can be split up into 0.6dB additional penalty consequence of the back reflection at the interfaces of the μOptics, which can be easily overcome by introducing AR-coatings at each interface.

While, the remaining 0.4dB of extra penalty derived from spherical aberration, due to the ball-lens, which leads to a distortion of the ideal Gaussian focal spot introducing side lobes. Moreover, the alignment and fabrication 1dB tolerances were demonstrated to be compatible with standard Photonics Packaging processes.

Eventually, even though, 2D FDTD results represents an ideal model, the results can be easily generalized to a 3D description just taking into account the solid of revolution related to the 2D MOB focal spot. This analysis showed that the redistribution of the energy across the central peak and the side lobes changes form the 3D to the 2D model showing that the weight of the side lobes on the laser-to-PIC coupling could potentially increase leading to a 1.4dBm extra loss.

This analysis was published in *Photonics Technology Letters* and it shows a new way of designing coupling scheme based on micro-optics for Photonics Packaging.

This can be considered quite interesting as it offers the possibility of simulating the entire coupling scheme giving the chance to optimise a GC structure for direct laser-to-PIC coupling.

This whole work can be further continued and generalized, and in the next section, some suggestions of possible future works are pointed out.

6.1 Future Work

The results of this research work bring new stimuli for future research and further developments in grating coupling, and additional work is necessary to achieve these goals.

In particular, I would like to summarize in few points the topics where it would be recommended to focus the future effort emphasizing the technological interest:

- Increase the BW of such non-uniform GCs. This can be done working on to different approaches. First, either off-the-shelf or customized micro-lens arrays can be used to reshape the single mode fiber emission changing the MFD dimension. Second, implementing the bandstructure analysis inside the design routine to tailor, through the GC structure, both the CE(λ_t) and the BW. In particular, it could be advisable to work on these two approaches at the same time in order to have a final optimized optical connector, instead of a single structure.

- Micro lens arrays can be tested to increase the alignment tolerances of such non-uniform GCs opening a possible path to achieve passive alignment, which could be potentially interesting for high-volume and low-cost Photonics Packaging processes.

- The design routine can be extended to the development of high efficient two dimensional GCs, obtaining performant polarization insensitive structures. Again, this can be quite interesting for optical packaging reducing material costs, as no polarization maintaining fiber would be necessary, as well as no external polarization controller reducing the time needed for the active alignment processes.

- The FDTD method can be applied to design a new MOB for laser-to-PIC coupling with a MFD able to fulfil all the requirements needed for high CE and wider BW values. Vice-versa, the design routine can be applied to design a non-uniform GC structure for such coupling scheme.

- The design of non-uniform GC can be extended to a different photonic platform, for example Si_3N_4, which importance is becoming relevant nowadays due to the potentialities of such material for applications in nonlinear optics and bio-photonics.

Glossary

1D: One-dimensional

2D: Two-dimensional

3D: Three-dimensional

AlN: Aluminium nitride

AR: Anti-reflection

AWG: Arrayed waveguide grating

BOX: Bottom oxide layer

BW: Bandwidth

CE: Coupling efficiency

CMOS: Complementary metal oxide semiconductor

CPB: Copper pillar-bump

DBR: Distributed Bragg reflector

DC: Duty cycle

e-beam: Electron beam

EIC: Electronic integrated circuit

ED: Etching depth

FDTD: Finite difference time domain

GDS: Graphic design system

GC: Grating coupler

HFb: Horizontal fiber

IL: Insertion loss

IPEK: Integrated photonics educational kit

InP: Indium phosphide

MEMS: Micro-electromechanical systems

MOB: Micro optical bench

MOSFET: Metal-oxide-semiconductor field-effect transistor

MPW: Multi-project-wafer

MFD: Mode field diameter

NA: Numerical aperture

PC: Photonic crystal

PDK: Process design kit

PIC: Photonic integrated circuit

PSO: Particle swarm algorithm

PM: Polarization maintaining

SBB: Solder ball bumps

SEM: Scanning electron microscope

sFT: Spatial Fourier transform

Si: Silicon

Si_3N_4: Silicon nitride

SiO_2: Silicon dioxide

SiON: Silicon oxynitride

SMF: Single mode fiber

SLD: Super luminescence diode

SOI: Silicon on Insulator

SSC: Spot size converter

Sub: Substrate

TE: Transverse electric

TEC: Thermoelectric cooler

TM: Transverse magnetic

TOX: Top oxide layer

UV: Ultraviolet

VCSEL: Vertical cavity surface emitting laser.

VFb: Vertical fiber

WG: Waveguide

WDM: Wavelength division multiplexing

List of Publications

A list of all the scientific production made during my years at the Tyndall National Institute as a PhD student are reported in chronological order for either journal and conference papers.

- Journal papers

  - Luca Zagaglia, Francesco Floris and Peter O'Brien, "Experimental Characterization of Particle Swarm Optimized Focusing Non-Uniform Grating Coupler for Multiple SOI Thicknesses," *Journal of Lightwave Technology*, vol. 39, no. 15, pp. 5028-5034, 2021, doi: 10.1109/JLT.2021.3079575.
  - Luca Zagaglia, Valeria Demontis, Francesco Rossella and Francesco Floris, "Semiconductor nanowire arrays for optical sensing: a numerical insight on the impact of array periodicity and density," *Nanotechnology*, vol. 32, no. 33, pp 335502(1-12), 2021, doi: 10.1088/1361-6528/abff8b.
  - Callum G. Littlejohns, David J. Rowe, Han Du, Ke Li, Weiwei Zhang, Wei Cao, Thalia Dominguez Bucio, Xingzhao Yan, Mehdi Banakar , Dehn Tran, Shenghao Liu, Fanfan Meng, Bigeng Chen, Yanli Qi, Xia Chen, Milos Nedeljkovic, Lorenzo Mastronardi, Rijan Maharjan , Sanket Bohora, Ashim Dhakal, Iain Crowe, Ankur Khurana 4,Krishna C. Balram, Luca Zagaglia, Francesco Floris, Peter O'Brien, Eugenio Di Gaetano, Harold M.H. Chong, Frederic Y. Gardes, David J. Thomson, Goran Z. Mashanovich, Marc Sorel and Graham T. Reed, "CORNERSTONE's Silicon Photonics Rapid Prototyping Platforms: Current Status and Future Outlook," *Applied Sciences*, vol. 10, no. 22, pp. 8201(1-34), 2020.
  - Luca Zagaglia, Francesco Floris, Lee Carroll and Peter O'Brien, "Comparing Laser Hybrid-Integration and Fiber Coupling With Standard Grating Couplers on Si-PICs," *IEEE Photonics Technology*

Letters, vol. 31, no. 1, pp. 66-69, 2019, doi: 10.1109/LPT.2018.2883211.

- Marco Passoni, Francesco Floris, How Yuan Hwang, Luca Zagaglia, Lee Carroll, Lucio Claudio Andreani, and Peter O'Brien, "Co-optimizing grating couplers for hybrid integration of InP and SOI photonic platforms," *AIP Advances*, vol. 8, no. 9, pp. 095109(1-7), 2018, doi: 10.1063/1.5046164.

- Conference papers

  - Luca Zagaglia, Simone Argiolas, Simone Iadanza, Giovanna Mura, Francesco Floris, and Peter O'Brien, "Vertical assisted directional-coupler from Silicon-on-Insulator to Silicon Nitride platforms," *META 2021, the 11th International Conference on Metamaterials, Photonic Crystals and Plasmonics*, 2021.
  - Luca Zagaglia, Francesco Floris and Peter O'Brien, "Analysis in reciprocal space of the band-pass filter effect in uniform and non-uniform grating couplers", *Journal of Physics: Conference Series, 10th Young Researcher Meeting*, 2020, vol. 1548, pp. 012031(1-6), doi:10.1088/1742-6596/1548/1/012031.
  - Luca Zagaglia, Francesco Floris and Peter O'Brien, "Optimized Design Procedure for Low-cost Grating-couplers in Photonics-packaging," *2019 PhotonIcs & Electromagnetics Research Symposium - Spring (PIERS-Spring)*, 2019, pp. 234-241, doi: 10.1109/PIERS-Spring46901.2019.9017442.

Acknowledgments

I thank Peter O'Brien, my supervisor, for giving me the opportunity to undertake such a stimulating "journey" in the Packaging Group at Tyndall, and for his support over the years.

A special thank goes to Francesco Floris, my co-supervisor, that guided and helped me with my PhD project offering his theoretical and experimental supports every time, but more importantly his friendship.

I thank all the people and co-workers in the Packaging Group during these years for the fruitful discussions, and for making the work environment so amazing. Here, a special thank goes to the Marc Rensing, Junsu Lee, Sean Collins, Noreen Nudds, Daniel Carey, Magaly Mora, Kamil Gradkowski, and Ivan-Lazar Bundalo.

I thank Lee Carroll for the helpful chats and for his mentorship provided during the first year of my PhD.

I thank all my friends and colleagues at Tyndall National Institute in particular Andrea Bocchino, Emanuele Galluccio, Ruggero Loi, Marcello Valente, and Simone Iadanza.

I am really grateful to my flatmates and friends at Lancaster Hall Dario Gentile, Michela Del Tin, Alex Cargnel, Andrea Fusco, Nicola Raduazzo, Adria Garcia Gil, and Silvia Cabre for their friendship and all the beautiful and funny moments spent together. They contributed in making my experience here in Ireland special and unforgettable.

I am grateful to Elisa Salvaneschi, my girlfriend, for her constant love and support, which helped and comforted me during the past years.

Finally, I am really grateful to my parents Vasco Zagaglia and Patrizia Zecconi, and my sister Laura Zagaglia for their affection, and support throughout my entire life.

Appendix A

Finite Difference Time Domain

The Finite Difference Time Domain (FDTD) is one of the simplest, easy to implement, and widely used numerical analysis technique employed in computational electrodynamics to resolve Maxwell's equations.

It was proposed for the first time in 1966 by Kane Yee [1] and the method is based on the discretization of the curl Maxwell's equations, *i.e.* Ampere's and Faraday's laws, in both space and time to obtain a complete description of the electromagnetic field propagation knowing the initial condition.

Thus, the FDTD method can be applied to resolve a wide range of electromagnetic problems giving information on both the electric and magnetic fields across the entire domain, enabling at the same time to perform a multiwavelength analysis. Moreover, as the FDTD purely resolve Maxwell's equations, no assumption regarding the electromagnetic problem is needed, with the major downsize of resulting computationally heavy and time-consuming.

The FDTD is an approximate method where the partial derivatives are substituted by their corresponding difference quotients, discretised thorough central-difference approximations.

In this contest, the electric and magnetic field are staggered in both space and time, and their positions are updated through the so-called leap-frog algorithm. Here, the updated value of the E-filed, at any point in space, depends on the previous stored value of the E-field and the numerical curl proper of the local distribution of the H-field. Equal relations hold for the H-field. This description is true for either 1-D, 2-D, and 3-D FDTD simulations.

According to [1], the spatially staggering of the vector components associated to the E- and H-field is preformed exploiting rectangular unit cells of a Cartesian grind, see Figure 65. Such configuration is known as Yee's cell, it has been proved to be very robust, and it is exploited by many FDTD software. In the thesis, the commercial software Lumerial® FDTD Simulations™ was used to perform the FDTD simulations [2]. For further details regarding the FDTD method, see [3].

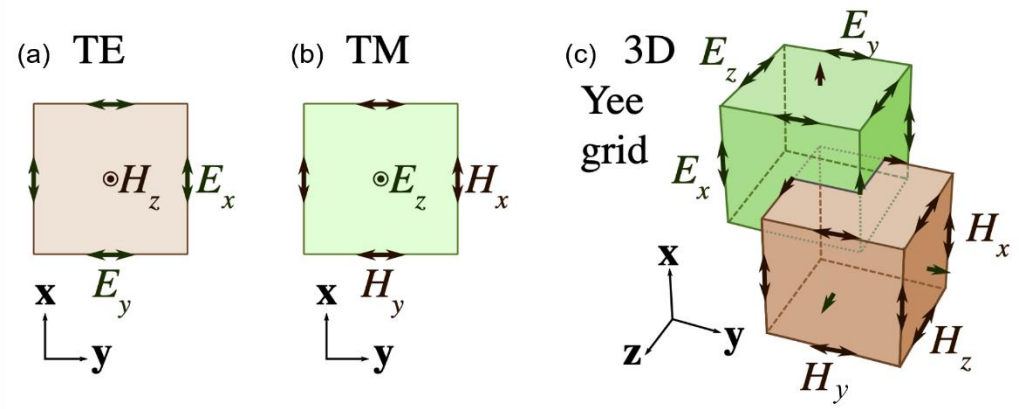

Figure 65: Sketch of the Yee's cell for: (a), (b) a 2D-FDTD cell related to the TE- and TM-polarization, respectively; (c) a 3D-FDTD cell. The figure has been taken from [4].

Appendix B

Particle Swarm Optimization Algorithm

The Particle Swarm Optimization Algorithm (PSO), described in Chapter 2, was written in Lumerical's scripting language [4]. The latter allows to automate: (i) the building of the entire simulation, from the structures, *e.g.* the grating coupler, to the monitors used to collect the desired data; (ii) the process of running the simulations; (iii) the storage and the analysis of the data. In particular, the different command exploited to perform the aforementioned three steps can be grouped and saved inside an external "script" file, which can be called and run directly from Lumerical.

The entire PSO procedure is composed by three separate "script" files: the main script where the iterative process is defined; a secondary script used to set up and run the simulation, tune the structure, and extract the coupling efficiency of each grating coupler; and a third script used to build the final 2D optimized grating coupler characterized by the best parameters found by the algorithm.

The main file is the core of the PSO and governs the entire iterative process. Here, the values of the initial parameters such as the number of agents, iterations, and the quantities to optimize are set, defining each agent's random starting position x_i.

At this point, the secondary script file is called for the first time in the main file in order to perform the actual FDTD simulations related to each agent collecting the coupling efficiencies, which are consequently stored. Thus, the initial g_{best} and $p_{i,best}$ can be defined and passed to the main file to control the temporal evolution of the agents across the parameter space through Eq. 11 and 12.

Now, the real iterative process, backbone of the main file, takes place as a closed loop between the main and the secondary file, which returns the coupling efficiencies of all the agent at each specific iteration. Moreover, the main file manages the "reflecting walls" boundary conditions mentioned in Chapter 2.

Eventually, the third file is called outside the closed loop to build the 2D optimized structure with the global best values, and saves the simulation. The main file then stores these best values of the structural parameters inside an external .txt file.

The development of the PSO algorithm took several months in order to: (i) understand its working principle and the whole structure; (ii) write the actual code exploiting Lumerical's scripting language; (iii) debug it; (iv) test the algorithm by running thousands of simulations for the optimization of grating couplers starting from uniform designs and then, moving to apodized designs. In particular, as explained in Chapter 3, apodized grating couplers required the writing of an external Python code to evaluate the effective refractive index of the fundamental mode of a 2D waveguide, used to build the grating pattern. For this specific case, the secondary script file was modified in order to upload the required values of the effective refractive index from an external .txt file.

Bibliography

[1] Kane Yee, “Numerical solution of initial boundary value problems involving maxwell's equations in isotropic media,” *IEEE Transactions on Antennas and Propagation,* vol. 14, no. 3, pp. 302-307, 1966.

[2] Ansys / Lumerical , “Lumerical FDTD,” [Online]. Available: https://www.lumerical.com/products/fdtd/

[3] Allen Taflove, and Susan Hagness, "Computational Electrodynamics: The Finite-Difference Time-Domain Method," 3rd ed., Norwood: Artech House, 2005.

[4] Wkipedia, “Finite-difference time-domain method,” [Online]. Available: https://en.wikipedia.org/wiki/Finite-difference_time-domain_method

[5] Ansys / Lumerical, “Lumerical scripting language,” [Online]. Available: https://support.lumerical.com/hc/en-us/articles/360037228834-Lumerical-scripting-language-By-category